

**Two-dimensional (2D) Monolayer Materials:
Exfoliation, Characterization, and Application**

Dissertation

zur Erlangung des akademischen Grades

Doktor rerum naturalium

(Dr. rer. nat.)

Vorgelegt

der Fakultät Mathematik und Naturwissenschaften

der Technischen Universität Dresden

durchgeführt am

Leibniz-Institut für Festkörper- und Werkstoffforschung

Dresden (IFW Dresden)

Von

Jiang Qu

geboren am: 15. August 1991 in Chongqing, China

Bibliografische Beschreibung

Jiang Qu

Two-dimensional (2D) Monolayer Materials: Exfoliation, Characterization, and Application

Dissertation (in englischer Sprache) an der Fakultät Mathematik
und Naturwissenschaften, der Technischen Universität Dresden,
2022/2023

132 Seiten, 49 Abbildungen, 4 Tabellen, 278 Referenzen

Gutachter: Prof. Dr. Bernd Büchner

Reviewers: Prof. Dr. Bernd Büchner

Prof. Dr. Axel Lubk

Prof. Dr. Karin Leistner

Committee: Prof. Dr. Jochen Geck (Chairman)

Prof. Dr. Bernd Büchner

Prof. Dr. Karl Leo

Prof. Dr. Axel Lubk

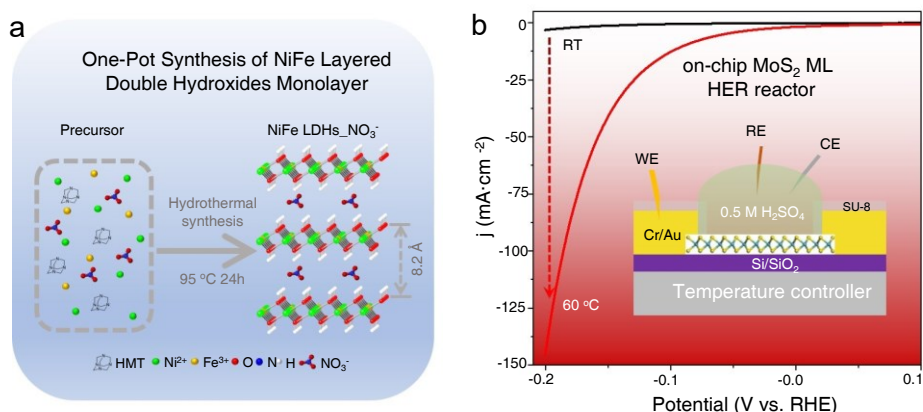
Prof. Dr. Karin Leistner

Submitted, Dresden, July 2022

Defended, Dresden, January 2023

Abstract

Monolayer two-dimensional (2D) materials have been regarded as a hot topic in the fields of condensed matter physics, materials science, and chemistry due to their unique physical, chemical, and electronic properties. However, the research on the preparation method and properties understanding of the 2D monolayer are inadequate. In this dissertation, taking 2D nickel-iron layered double hydroxides (NiFe LDHs) and molybdenum disulfide (MoS_2) as examples, the practicability of the direct synthesis of NiFe LDHs monolayer and the thermal enhancement catalytic performance of 2D MoS_2 monolayer (MoS_2 ML) are discussed. First, a one-pot synthetic strategy (bottom-up method) is presented to synthesize 2D NiFe-based LDHs monolayers, including NiFe, Co-, Ru-, doped and Au modified NiFe LDHs. The prerequisite and universality of this strategy are investigated and confirmed. The features of LDHs are characterized by advanced technologies. The obtained LDH bulks own a large interlayer spacing up to 8.2 Å, which can be facilely exfoliated into monolayers in water by hand-shaking within 10 s. As a result, the as-prepared NiFe-based LDH monolayers display a good electrocatalytic oxygen evolution reaction (OER) performance. This facile strategy paves the way for designing easily exfoliated LDHs for highly active catalysts and energy conversion devices based on other monolayer LDHs.^[1] Second, with gold-modified tape, 2D MoS_2 ML is exfoliated from the bulk crystal through a micromechanical exfoliation method (top-down strategy). The thermal effects of MoS_2 ML are confirmed by Raman and photoluminescence (PL) spectra. Moreover, an on-chip MoS_2 ML hydrogen evolution reaction (HER) reactor is designed and fabricated. The thermal effects generate efficient electron transfer in the MoS_2 ML and at the electrolyte-catalyst (MoS_2 ML) interface, leading to an enhanced HER performance. Compared to the results obtained at room temperature, the MoS_2 ML shows a direct thermal enhanced HER performance at higher temperatures.^[2] In summary, the findings and understandings, the direct synthesis and direct thermal enhancement catalytic performance, of 2D monolayers offer a guideline for synthesizing and catalyst application of other 2D monolayers.



Abstract schematic: (a) One-pot synthesis of nitrate-intercalated NiFe layered double hydroxides; (b) Direct thermal enhancement of HER of on-chip MoS_2 ML microdevice.

Keywords: two-dimensional (2D), monolayer (ML), exfoliation, one-pot synthesis, NiFe layered double hydroxides, MoS_2 , oxygen evolution reaction (OER), hydrogen evolution reaction (HER), and thermal enhancement.

References:

- [1]. J. Qu*, F. Li, M. Wang, S. Subakti, M. Deconinck, G. Chen, Y. Li, L. Liu, X. Wang, M. Yu, D. Wolf, A. Lubk, B. Büchner, Y. Vaynzof, O. Schmidt, and F. Zhu, *Adv. Mater. Interfaces*, 2022, 9, 2200973, DOI: 10.1002/admi.202200973.
- [2]. J. Qu*, Y. Li, F. Li, T. Li, X. Wang, Y. Yin, L. Ma, O. Schmidt, and F. Zhu, *ACS Nano* 2022, 16, 2921–2927, DOI: 10.1021/acsnano.1c10030.

Contents

Abstract.....	1
1. Introduction.....	7
1.1. Research background.....	7
1.2. Motivation and goals	8
1.3. Structure of the dissertation.....	10
2. Fundamentals	12
2.1. 2D materials family	12
2.2. Exfoliation of 2D materials.....	13
2.3. Characterization and applications of 2D monolayer	15
2.4. Sustainable energy and water splitting	16
2.5. 2D electrocatalyst for water splitting	21
2.6. Oxygen evolution reaction.....	23
2.7. Background of 2D NiFe LDHs for OER	26
2.8. Features of 2D monolayer	31
2.9. Hydrogen evolution reaction	32
2.10. Background of 2D MoS ₂ monolayer for HER	34
3. Materials and methods	37
3.1. Materials preparation and device fabrication	38
3.1.1. Materials	38
3.1.2. Synthesis of NiFe LDHs monolayer	38
3.1.3. Mechanical exfoliation of MoS ₂ monolayer	39
3.1.4. Photolithography	40
3.1.5. Electron beam evaporation	41
3.2. Characterization methods	42
3.2.1. Scanning electron microscopy	42
3.2.2. Transmission electron microscopy	42
3.2.3. X-ray photoelectron spectroscopy.....	43
3.2.4. X-ray diffraction	43
3.2.5. Raman and photoluminescence spectra	44
3.2.6. Fourier transform infrared spectroscopy	45

3.2.7.	Atomic force microscopy	45
3.3.	Electrochemical characterization	46
3.3.1.	Total electrode activity	47
3.3.2.	Overpotential	47
3.3.3.	Tafel equation	48
3.3.4.	Cyclic voltammetry and double-layer capacitance.....	48
3.3.5.	Turnover frequency	49
3.3.6.	Electrochemical impedance spectroscopy	50
3.3.7.	Stability measurement.....	50
4.	Experiments and results	51
4.1.	One-pot synthesis of nickel-iron layered double hydroxides monolayer	52
4.1.1.	Introduction	52
4.1.2.	Fabrication of NiFe LDHs.....	54
4.1.3.	Schematic, structure and exfoliation of the NiFe LDHs monolayer	57
4.1.4.	Structure evolution of NiFe LDHs	62
4.1.5.	Universality investigation of the synthesis strategy	67
4.1.6.	OER performance of NiFe LDHs monolayers	70
4.1.7.	OER performance of multi-metal NiFe-based LDHs monolayer	74
4.1.8.	Conclusion.....	76
4.2.	Direct thermal enhancement of hydrogen evolution reaction of on-chip monolayer MoS ₂	77
4.2.1.	Introduction	78
4.2.2.	Fabrication of on-chip MoS ₂ ML devices	79
4.2.3.	Characterization of MoS ₂ ML.....	81
4.2.4.	Laser-induced thermal effects of MoS ₂ ML	82
4.2.5.	Temperature-dependence of HER on MoS ₂ ML	84
4.2.6.	Side effects of HER on MoS ₂ ML	90
4.2.7.	Stability of HER on MoS ₂ ML.....	93
4.2.8.	Conclusion.....	95
5.	Summary and outlook	96
5.1.	Summary	96
5.2.	Outlook	97

List of Figures and Tables	98
List of Abbreviations	103
Bibliography	105
Acknowledgments.....	121
Publications.....	123
Curriculum Vitae	125
Selbständigkeitserklärung.....	127

1. Introduction

In this section, first, the background of energy conversion, such as water splitting, is presented based on two-dimensional (2D) monolayer materials. Next, the motivation and goals of this dissertation that two kinds of 2D monolayer materials were studied: 2D NiFe LDHs monolayer through a bottom-up synthesis and 2D MoS₂ ML through a top-down strategy, respectively. Advanced technologies are also introduced for measuring and evaluating the 2D monolayers. Finally, the outline and structure of the dissertation are presented.

1.1. Research background

With the increasing concern regarding environmental pollution and energy security related to the decreasing availability of fossil fuels, the pursuit of clean and renewable energy sources has become one of the greatest challenges for the sustainable development of society.^[1-3] The research and development of clean energy are of vital importance in the coming decades. Core to this development is the need for advanced energy conversion technologies, such as water splitting ($\text{H}_2\text{O} (\text{l}) \rightarrow \text{H}_2 (\text{g}) + \frac{1}{2} \text{O}_2 (\text{g})$), which has been considered to be a clean, efficient, and sustainable strategy to replace fossil fuels.^[4, 5] However, the sluggish kinetics of the multi-electron transfer in the OER/HER process limit the performance of corresponding energy devices.^[6] Conventionally, the sluggish kinetics of the chemical reactions that take place in these devices can be reduced by the commercial catalysts based on precious metals such as Pt, Ir, and Ru, which suffer from poor stability and high cost, greatly prohibiting their large-scale application.^[3, 7, 8] In addition, the reaction mechanisms of the related reactions are still unclear and in some cases, even the general enhancement methods are not sufficient. Thus, it has become a significant endeavor in clean energy research of developing high-performance, low-cost non-precious metal catalysts alternatives and of exploring the possible enhancement method to understand the mechanisms.

On the other hand, with the discovery of graphene,^[9] 2D materials with atomic thickness have emerged as one of the most promising candidates in the fields of condensed matter physics, materials science, and chemistry due to their unique physical, chemical, and electronic properties.^[10-12] Recently, new 2D materials and their derivatives have been applied as electrocatalysts because of their 2D structure and specific electronic structure.^[13-15] The 2D bulk materials show very low catalytic performance because of the limited active sites.^[3] Various optimization protocols have been developed to prepare efficient electrocatalysts by increasing the active site number through exfoliating the 2D bulk into monolayer or few-layer nanosheets.^[16-18] Therefore, 2D monolayer electrocatalyst is one of the possible options to develop high-performance and low-cost alternatives to clean and sustainable energy.

1.2. Motivation and goals

As a result, these anisotropic 2D materials hold great potential for the design of high-performance electrocatalysts,^[19] and provide an ideal platform to reveal the reaction mechanisms on 2D monolayers, such as field-effect, photoelectrical, and magnetic enhancement methods.^[20-24] To break the van der Waals interaction of 2D materials between the layers, many methods were developed.^[25-29] Taking LDHs, which were recognized as one of the most promising catalysts for OER,^[30-32] as an example, the monolayer can be fabricated by ion-exchange exfoliation,^[19, 33-39] liquid-phase exfoliation,^[40] acid/alkali solution etching,^[41, 42] water-plasma etching,^[43] and argon-plasma etching^[44] methods. However, the exfoliation processes are usually complex, multi-step, labor-intensive, and time-consuming with low yields and throughputs, and they may not be scalable for industrial applications.^[29, 45-47] Therefore, it is urgent to develop a one-pot method for synthesizing 2D LDHs with large interlayer spacing, which can be directly exfoliated into monolayers.

The first goal of this dissertation is to present a one-pot method to synthesize 2D NiFe LDHs monolayers. This method may lay a good foundation for later large-scale production of 2D LDHs monolayers for high-performance and low-cost non-precious

metal catalysts. The key synthetic aspects, such as the prerequisite for the formation of easily exfoliated LDHs and the universality of the synthesis strategy, will be discussed. The structure of NiFe LDHs will be investigated by advanced characterization methods, including scanning electron microscopy (SEM), transmission electron microscopy (TEM), X-ray photoelectron spectroscopy (XPS), X-ray diffraction (XRD), Raman spectroscopy, Fourier-transform infrared spectroscopy (FTIR) and atomic force microscopy (AFM). Moreover, the OER performance of the NiFe LDHs monolayers will be evaluated to investigate the potential application for energy conversion. However, the obtained 2D NiFe LDHs monolayer is not an ideal platform to reveal the reaction mechanisms because of the random distribution and uncontrollable size of the monolayers.

With the rapid development of various catalysts, there seems a bottleneck for the probing mechanism of reactions and enhancing methods of catalysts. The second goal of this dissertation is to reveal the possible reaction mechanisms/enhancement method on 2D monolayer materials. In this section, a 2D MoS₂ ML with a large size has been exfoliated through a mechanical method with gold tape. The 2D MoS₂ ML will be investigated by Raman, photoluminescence (PL) spectroscopy, and XPS. The laser-induced thermal effects of MoS₂ ML will be investigated by Raman and PL spectra. Then, an on-chip MoS₂ ML microelectrode will be fabricated with photolithography and e-beam deposition methods. Lastly, the relationship between HER performance and the temperature of the on-chip MoS₂ ML will be presented.

In short, the goal of this dissertation is to make a thorough inquiry into 2D monolayer materials by bottom-up and top-down exfoliation methods. At first, a strategy to synthesize 2D NiFe LDHs with large interlayer spacing, which can be directly exfoliated into monolayer nanosheets, is provided (bottom-up synthesis). Then, MoS₂ ML with a large size is exfoliated from the bulk (top-down exfoliation). The OER performance of NiFe LDHs and the thermal enhanced HER performance of MoS₂ ML are discussed.

Future opportunities and challenges in terms of both fundamental understanding and applications based on 2D monolayer materials will be presented.

1.3. Structure of the dissertation

The dissertation starts with a brief introduction to exfoliation, characterization, and applications of 2D materials. Subsequently, the background of OER/HER electrocatalysts based on 2D monolayers is summarized. Then, the exfoliation process, characterization, and electrocatalytic application based on the exfoliated 2D monolayer are discussed. Finally, the experimental results, conclusions, and potential applications of two kinds of 2D monolayers are presented. The detailed structure of the dissertation is listed as follows.

Chapter 1 introduces the research background, motivation, and goals of this dissertation based on 2D monolayer materials for energy conversion, and the outline of the dissertation.

Chapter 2 gives an overview of 2D materials, exfoliation of 2D materials, sustainable energy future and electrocatalysts for sustainable energy, the principle of water splitting, and the possible reaction pathway of OER/HER. The features of the 2D monolayer are summarized. The research background of 2D electrocatalysts for sustainable energy is investigated, especially, the 2D NiFe LDHs for OER and on-chip 2D MoS₂ ML for HER.

Chapter 3 introduces the overall experimental methods employed in this dissertation. The raw materials, experimental methods, characterization methods, device fabrication, and electrochemical characterization are listed for both 2D NiFe LDHs and 2D MoS₂.

Chapter 4 presents the results of both physicochemical properties and their potential electrocatalytic application of 2D NiFe LDHs and MoS₂ monolayers. In the first section, a bottom-up synthesis method is reported to prepare easily exfoliated 2D NiFe LDHs

and the efficient OER catalytic performance of the NiFe LDHs monolayer is described. Then, by combining the microfabrication and chemical process, the relation between HER performance and the temperature of MoS₂ ML is disentangled in the second section.

Chapter 5 concludes the whole work in this dissertation and presents new opportunities for future works based on 2D monolayer materials.

The List of Figures and Tables, List of Abbreviations, Bibliography, Acknowledgements, Publications, Curriculum Vitae, and Declaration of Independence are listed at last.

2. Fundamentals

This chapter provides the fundamentals of the dissertation, including the 2D materials family, exfoliation, characterization, and applications of the 2D monolayers. First, the types, the exfoliation methods/strategies, characterization, and applications of 2D materials are summarized. Then, the future of sustainable energy, the key role of electrocatalysts for sustainable energy, and the principle of water splitting are discussed. Afterward, the research background and the possible reaction pathway for OER based on NiFe LDHs are discussed. Finally, the background and prospects of 2D materials for HER based on on-chip 2D MoS₂ are summarized. The details are listed bellows.

2.1. 2D materials family

As previously mentioned, 2D materials have expanded rapidly since the discovery of graphene in 2004^[9] because of their unusual electronic, mechanical, and optical properties, which have led to their extensive study over the past decades for diverse applications. Generally, 2D layered materials, in contrast to thin films, form strong chemical bonds in-plane but weak van der Waals interactions out-of-plane.^[25, 48-53] There are many types of 2D materials, which can be grouped into diverse families, such as the graphene family, 2D chalcogenides, 2D halides, and 2D oxide/hydroxides family.^[29] As displayed in **Figure 2. 1**, a variety of 2D materials have been successively isolated, including graphene,^[9] hexagonal boron nitride (h-BN),^[54] transition metal dichalcogenides (TMDs, e.g. MoS₂),^[55] metal phosphorous trichalcogenides (MX₃ and MPX₃),^[56] metal halides (MX₂, MX₃, MX₄, MX₅, and MX₆),^[57] metal oxides (such as V₂O₅,^[58] MoO₃,^[59] and perovskites^[60]), hexagonal structures of group III-VI monochalcogenides (such as InSe and GaS),^[61] clays,^[62] LDHs,^[63] and metal carbides and nitrides (MXenes).^[64, 65] Although many layered materials exist, all 2D materials share a planar and therefore the 2D materials own the potential characteristic to be

exfoliated into nanosheets, even monolayers, which will yield new and novel properties that radically differ from their bulk counterparts.

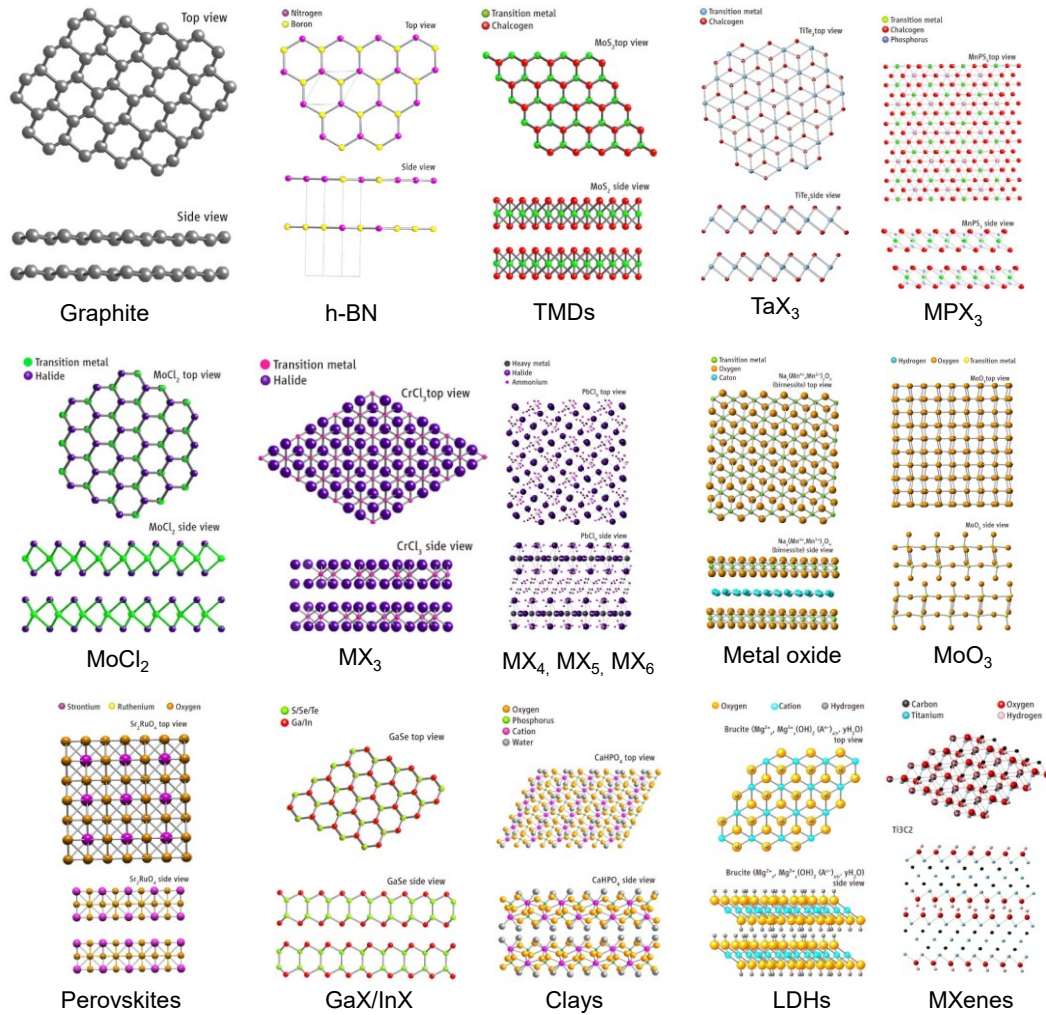


Figure 2. 1 Structure of 2D materials family: atomic structure of top and side view for different types.^[29]

2.2. Exfoliation of 2D materials

Ultrathin 2D nanosheets are attracting great interest and several methods have been developed to exfoliate 2D bulk into monolayers. After exfoliation, the 2D nanosheets, especially, the monolayer, can be micrometers wide but less than a nanometer thick, leading to an extremely high aspect ratio of the nanosheets. The confinement of the exfoliated 2D nanosheets leads to unique optical and electrical properties. There is no doubt that the exfoliation and reconstruction of 2D multifunctional composites play a

large role in the future, which will be used for large-scale applications of flexible electronics,^[66, 67] supercapacitors,^[68] and catalysts.^[69] For instance, more and more new types of 2D multifunctional composites will be developed with enhanced mechanical, electrical, and barrier properties. The 2D layered materials will appear as electrodes or active elements in devices such as displays, dielectrics, optoelectronics, and transistors. Particularly, the 2D materials also can be used as high-performance electrocatalysts and core platforms to understand the catalytic reaction mechanism for energy conversion, which will be discussed in this dissertation.

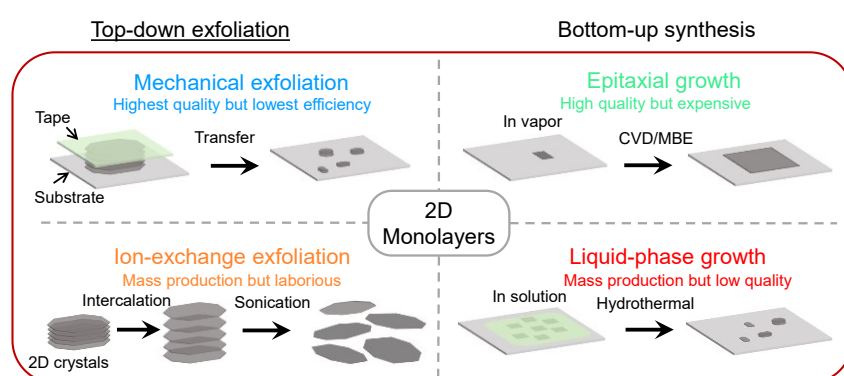


Figure 2. 2 Schematic illustrations of typical 2D monolayer synthesis methods. (a) Top-down strategies for the exfoliation of 2D bulk layered crystals through mechanical cleavage and ion-exchange exfoliation methods. (b) Bottom-up synthesis of 2D monolayers using liquid-phase growth or epitaxial growth methods.

In general, as illustrated in **Figure 2. 2**, the exfoliation methods of 2D materials can be categorized into two groups. First, in a top-down manner, the 2D monolayer can be obtained directly by the delamination of bulk crystals through mechanical cleavage or ion-exchange exfoliation methods (**Figure 2. 2a**). Moreover, the 2D monolayer can be prepared by using liquid-phase growth or epitaxial growth methods in a bottom-up manner (**Figure 2. 2b**). For instance, to date, many strategies have been developed to construct 2D MoS₂ monolayers, including mechanical exfoliation,^[28, 70-79] liquid-phase exfoliation,^[18, 26, 29, 45, 80-83] chemical vapor deposition (CVD),^[84-86] molecular-beam epitaxy (MBE),^[87, 88] and hydrothermal/solvothermal methods.^[89-91] The mechanical exfoliation and epitaxial growth methods can provide 2D monolayers with high quality

and large size, while it is hard to obtain an ordered and isolated monolayer by the liquid-phase exfoliation and hydrothermal/solvothermal methods. In comparison, the mechanical exfoliation method remains the source of the highest-quality 2D monolayers, but it suffers from a low yield and production rate, which is not technologically scalable in its current form. On contrary, the liquid-phase exfoliation method gives large quantities of dispersed nanosheets, but the as-prepared nanosheets are uncontrolled in size and quality. Compare to the hydrothermal or solvothermal methods, the epitaxial growth method is one of the most efficient methods to grow 2D monolayers of large size and high quality. Different methods are appropriate for different objectives, e.g. the liquid-phase exfoliation and hydrothermal/solvothermal methods are suitable for large-scale applications, while the mechanical exfoliation/epitaxial growth of 2D monolayers with the highest quality, providing a platform for relevant basic research.

2.3. Characterization and applications of 2D monolayer

In the following part, in general, the advanced characterization methods and applications will be discussed for the 2D monolayers. With the rapid development of nanoscience and nanotechnology, some powerful and useful characterization technologies have been adopted for characterizing 2D monolayers, including the composition, size, thickness, crystallinity, crystal phase, electronic states, oxidation states, or defects.^[92] Advanced characterization technologies, such as optical microscopy, SEM, TEM, scanning transmission electron microscopy (STEM), scanning probe microscopy (SPM), AFM, Raman, PL, and XPS, have been widely used for distinguishing ultrathin 2D monolayers. Optical microscopy, SEM, and TEM give the morphology or crystal structure information of the ultrathin 2D monolayers. The STEM, SPM, and AFM show the geometric features of 2D monolayers, such as the size, thickness, or defects.^[25, 93, 94] The Raman and PL spectra are powerful tools to investigate the optical properties of 2D monolayers,^[95-97] which give the absorption, scattering, and nonlinear effect information after a light-matter interaction at atomic

scales. XPS is an efficient technology used to determine the chemical composition and electronic states of the 2D nanosheets.^[22, 26] Besides, in light of recent advances, the applications of 2D materials have become a worldwide investigated hot spot, including electronics, flexible electronics, spintronics, optoelectronics, photodetectors, sensors, energy conversion and storage, catalysis, etc.^[98-104]

2.4. Sustainable energy and water splitting

Fossil fuels have formed the cornerstone of the global energy system, bringing unprecedented economic growth and technological progress, powering the industrialization of human society, but also causing serious environmental damages. These damages are happening because large amounts of greenhouse gases are released into the atmosphere from human activities worldwide, especially, the combustion of fossil fuels. Energy is both the reason for the problems and the solution to solve them. In essence, greenhouse gas emissions related to energy can be cut in two ways. First, fossil fuels can be replaced by sustainable energy sources by opting for cleaner energy sources. Second, the overall consumption of energy through energy savings and energy efficiency gains, such as, by using greener transport modes.^[105] Simply, the future of sustainable energy is to improve the energy efficiency of human activities by pursuing low-carbon energy solutions. One goal is to develop an electrochemical conversion system that can convert molecules (e.g., water (H₂O), carbon dioxide (CO₂), and nitrogen (N₂)) into higher-value products (e.g., hydrogen, hydrocarbons, oxygenates, and ammonia) by coupling to renewable energy.^[3] As displayed in **Figure 2. 3**, a sustainable energy cycle contains three parts: source of energy, conversion of energy, and storage or utilization of energy. In addition to using solar, wind, and hydropower, the use of hydrogen produced by renewables in combination with carbon capture and storage, which is also an effective route to reduce greenhouse gas emissions. Moreover, energy conversion technologies, such as electrochemistry and photoelectrochemistry, are critical for alleviating energy-related greenhouse gas emissions. Electrocatalysts play a key role in these energy conversion

technologies because they can increase the rate, efficiency, and selectivity of the involved chemical transformations. However, the available electrocatalysts nowadays are far from satisfactory. The grand challenge is to develop advanced electrocatalysts with enhanced performance, enabling the widespread application of clean energy technologies.

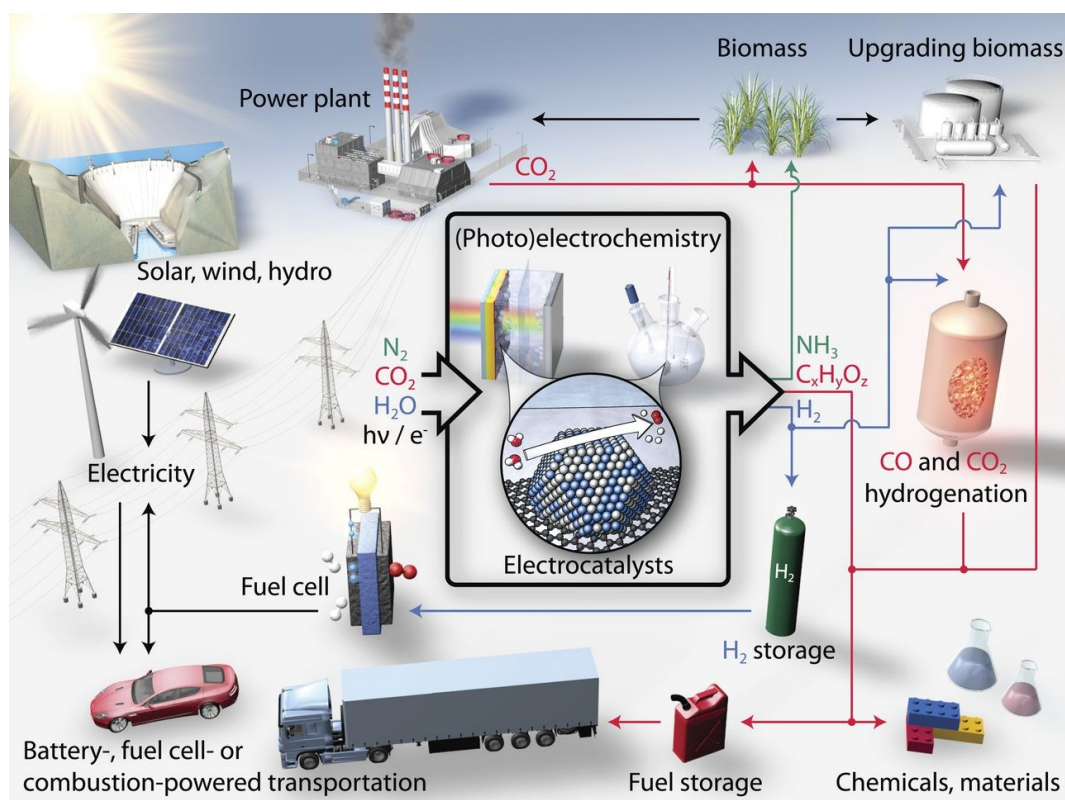


Figure 2. 3 Sustainable energy future. Schematic of a sustainable energy landscape based on electrocatalysis.^[3]

Over the past decades, substantial progress has been made in understanding several key (photo)electrochemical transformations, such as electrochemical reduction of CO_2 gas, electrochemical reduction of N_2 gas, and electrocatalytic splitting of liquid H_2O . That means, CO_2 , N_2 , and H_2O can be transformed into hydrocarbon, ammonia, oxygen, and hydrogen via electrochemical or (photo)electrochemical methods in a cell. One core roles of those technologies is providing the appropriate electrocatalyst for clean energy conversion. Electrocatalysis is one type of catalysis that can speed up the rate of an electrochemical reaction occurring at the electrode-electrolyte interface.

Electrocatalysis plays both the role of the electron donor/acceptor (electrode) and of the catalyst, which will reduce the barrier of the transition state during the reaction process. Generally, the goal of the catalyst design is to increase the number of active sites and/or increase the intrinsic activity of each active site by designing a porous structure, loading the catalyst onto a conductive supports, exposing high-efficient catalyst crystal planes, and so on (**Figure 2. 4**).^[3] For example, as mentioned in Chapter 2.2, the exfoliation of 2D materials bulk into monolayers is one of the efficient ways to increase the number of active sites.

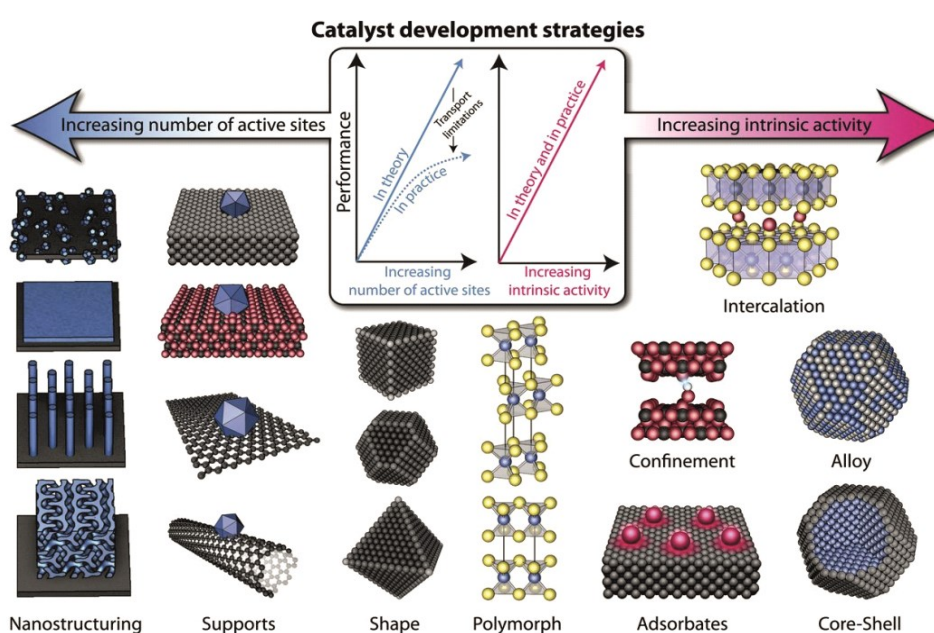
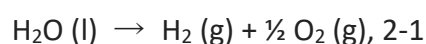


Figure 2. 4 Catalyst development strategies. Schematic of various catalyst development strategies, which aim to increase the number of active sites and/or increase the intrinsic activity of each active site.^[3]

Numerous innovative ideas have been proposed for achieving more efficient energy conversion, such as water splitting, in which the water molecules can be broken down to generate oxygen and hydrogen under an applied potential (**Figure 2. 5a**). The overall water splitting, which occurred at the electrified solid-liquid-gas three-phase interface of the anode and the cathode, is described as follows:



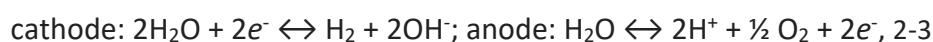
Under standard conditions, an input activation energy of $\Delta G = -237.13$ kJ/mol is required to achieve electrochemical water splitting, which corresponds to a thermodynamic voltage (E^0) of 1.23 V (**Figure 2. 5b**).^[106] The core of water splitting technologies is HER at the cathode and OER at the anode of an electrolytic cell thus producing gaseous molecular hydrogen and oxygen, respectively.^[107, 108] The Pourbaix diagram in **Figure 2. 5c**, also known as a potential/pH diagram, shows a plot of possible thermodynamically stable phases concerning the reversible hydrogen electrode (RHE) as calculated by the Nernst equation. In the Pourbaix diagram, the limits of stability of water are marked by the two dark dashed lines, showing the stability region for water between these lines. Under highly reducing conditions (bottom left in **Figure 2. 5c**), the water will be reduced to form hydrogen gas. Correspondingly, under highly oxidizing conditions (top right in **Figure 2. 5c**), water will be oxidized to form oxygen gas.

Depending on the reaction conditions, the reaction can be expressed in different ways (**Figure 2. 5c**):

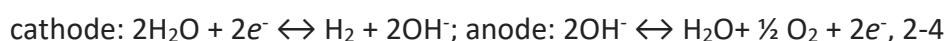
(a) in acidic solutions:



(b) in neutral solutions:



(c) in alkaline solutions:



Usually, those reactions on both electrodes are reversible in fuel cells, where the hydrogen oxidation reactions (HOR) and oxygen reduction reactions (ORR) convert chemical energy into electrical energy. The fuel cell stacks generate the electricity that powers the electric motor by using oxygen and hydrogen. Nevertheless, in practice,

more energy is required due to the kinetic barriers for both HER and OER, while loss of energy will occur for HOR and ORR in fuel cells as seen in **Figure 2. 5d**.

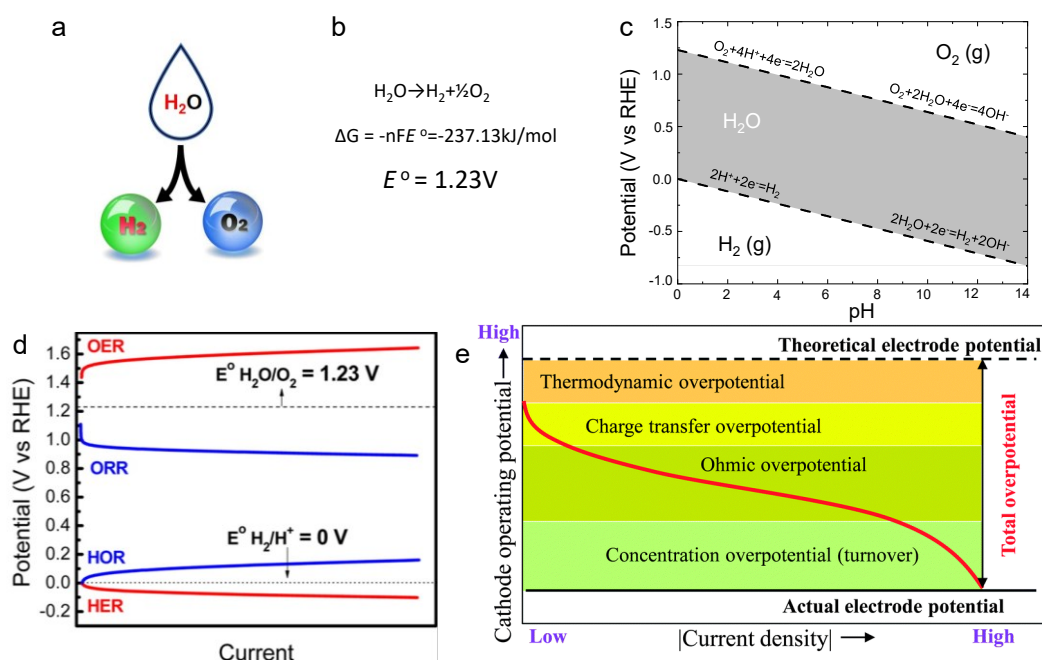


Figure 2. 5 Water splitting. (a) Schematic of water splitting. (b) The standard reaction of water splitting. ΔG represents activation energy, $n = 2$ for 2 electron transfer in the reaction and $F = 96485.3329 \text{ s}\cdot\text{A/mol}$ (Faraday constant). E° denotes the standard reversible electrode potential of water splitting. (c) Pourbaix diagram of water. (d) Representative polarization curves of OER, ORR, HOR, and HER.^[109] (e) Generalized polarization curve for an electrochemical power conversion device with multiple sources of overpotential.^[110]

The difference between the applied potential (E) and thermodynamic voltage (E°) is recognized as overpotential (η). The overpotential (η) is mainly used to overcome the intrinsic activation barriers present on both anode (η_a) and cathode (η_c), as well as some other resistances (η_{other}),^[1] which come from thermodynamics, charge transfer, ohmic contacts and even concentration overpotentials (**Figure 2. 5e**).^[110] It is seen that reduction of the overpotentials by suitable methods is the central issue to make the water splitting reaction efficient. The η_a and η_c have to be minimized by highly active catalysts, such as precious-metal-based catalytic materials, for instance, commercial platinum on carbon (Pt/C)^[111, 112] or IrO₂^[113] for the HER and OER, respectively.

However, the high prices of these materials hinder their larger-scale applications. Indeed, η_{other} can be reduced by optimizing the design of the electrolytic cell.^[114] Therefore, it is of great importance to develop highly active and earth-abundant catalysts to facilitate sustainable energy production.^[1, 2, 5, 115, 116]

2.5. 2D electrocatalyst for water splitting

In recent years, the 2D ultrathin layered materials have shown great application prospects in energy conversion for sustainable energy as electrocatalysts.^[11-13, 15] First, 2D atomic crystals are of considerable merits for heterogeneous electrocatalysts because of their unique structural, physical, chemical, and electronic properties. These advantages can be attributed to the anisotropy property introduced by strong covalent bonds extending through the plane whereas weak van der Waals interactions exist between layers, compared to their bulk counterparts and other nanomaterials.^[12, 15] Second, the motivation to study and develop 2D electrocatalysts is that they are typically inexpensive, which makes them be regarded as the most promising candidates as replacements for precious-metal-based electrocatalysts (such as Pt, Ir, and Ru).^[31, 117, 118] Third, 2D atom-level framework provides an ideal platform for the exploration of catalytic active sites from both theoretical and experimental perspectives.^[119, 120] Representative 2D materials that exhibit extraordinary properties in the area of water splitting, e.g., include graphene,^[121] graphitic carbon nitride (g-C₃N₄),^[122-124] hexagonal boron nitride (h-BN),^[125] and black phosphorus (BP),^[126, 127] transition metal dichalcogenides (TMDs),^[20, 69, 128] LDHs,^[107, 129] layered transition metal carbides and nitrides (MXenes),^[24, 130, 131] and metal-organic frameworks/covalent-organic frameworks (MOFs/COFs).^[132-134] Currently, 2D NiFe LDHs and 2D MoS₂ are the most common 2D materials in research for oxygen and hydrogen evolution, respectively.

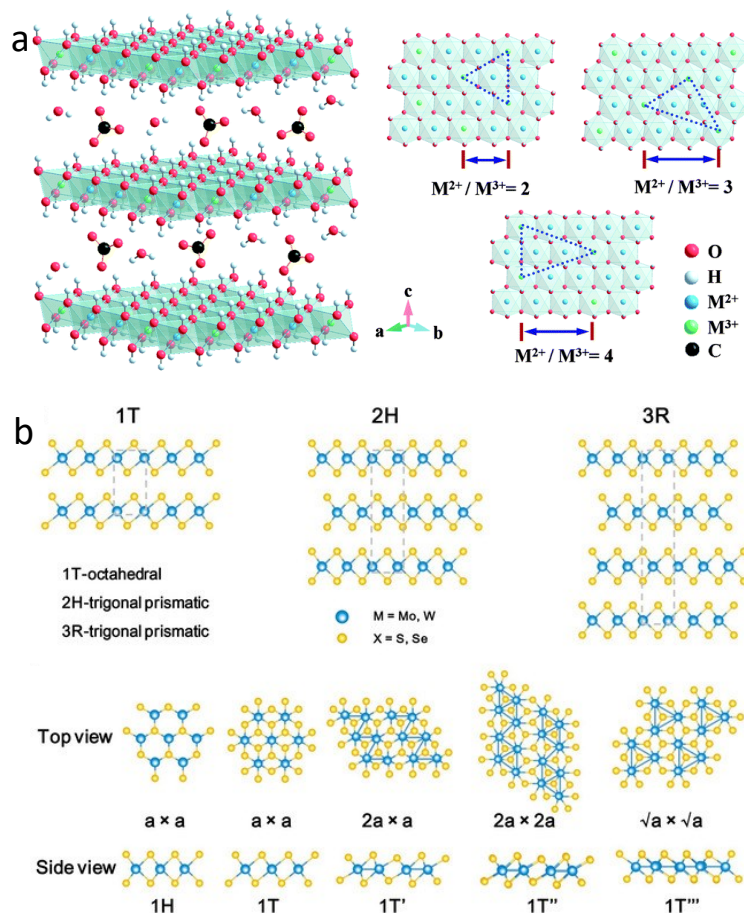


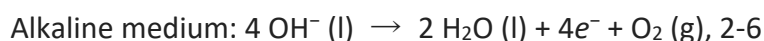
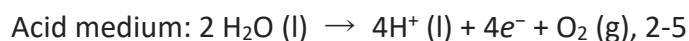
Figure 2. 6. Schematic structural configurations of 2D LDHs and TMDs. (a) The idealized structure of carbonate-intercalated LDHs with different M^{2+}/M^{3+} molar ratios shows the metal hydroxide octahedrons stacked along the crystallographic c -axis, as well as water and anions present in the interlayer region.^[135] (b) Structural polymorphs of bulk TMDs with 1T, 2H, and 3R phases structure.^[136]

The typical structures of LDHs and TMDs are displayed in **Figure 2. 6**. LDHs are composed of positively brucite-like layers, possessing octahedral MO_6 units in a stacked conformation, balanced by negatively charged anions along with structural water within the interlayer (**Figure 2. 6a**). TMDs are represented in MX_2 stoichiometry formula where M represents a transition metal belonging to groups IVB-VIIIB and X is a chalcogen from group VIA (S, Se, Te). TMDs exhibit a variety of structural polymorphs: trigonal (1T), hexagonal (2H), and rhombohedral (3R) forms (**Figure 2. 6b**). The polymorphs are determined by the different chalcogen and transition metal atoms, while the polytypes are determined by the stacking order of two or more individual triatomic layers with the same symmetry. In short, from those two examples,

it can be seen that the features of 2D materials have strong covalent bonds within the plane extended through the atoms whereas weak van der Waals interactions exist between layers. The stacked 2D materials have a limited number of active sites and the plane of 2D materials are usually inert. In order to improve the energy conversion efficiency, the 2D materials can be exfoliated into monolayers by increasing the number of active sites, and also the intrinsic activity of the inert 2D planes can be activated.

2.6. Oxygen evolution reaction

The OER, half-reaction of the water splitting (Equ. 2-1), is a four electron-proton coupled reaction, which involves several surface-adsorbed multiple intermediates, the binding energies of which are strongly correlated and cannot be decoupled easily because of a universal scaling relationship.^[2] As shown in **Figure 2. 7a**, the OER can proceed either by a direct combination of two adsorbed oxygen ($O_{(ad)}$) to produce O_2 (light green route) or by a formation of the $OOH_{(ad)}$ intermediate after multi-steps (black route). It is consisting of a series of consecutive reaction steps for the multi-electron reaction intermediate pathways, which can be either electron transfer steps or chemical steps, such as association/dissociation reactions. The OER can occur with different routes depending on the reaction media (acidic/alkaline conditions in **Figure 2. 7a**) and the specific catalyst used, but most of them involve adsorption/desorption of the oxo, peroxide, and superoxide intermediates ($O_{(ad)}$, $OOH_{(ad)}$, $OO_{(ad)}$). The overall OER reaction in acid and alkaline electrolytes is usually different as shown in **Figure 2. 7a**:



Lots of research groups have proposed the possible OER mechanisms in acid and alkaline mediums.^[2, 5, 123, 137, 138] During the OER process, all the bonding interactions

within the intermediates ($O_{(ad)}$, $OOH_{(ad)}$, $OO_{(ad)}$) are crucial to determining the overall electrocatalytic performance.

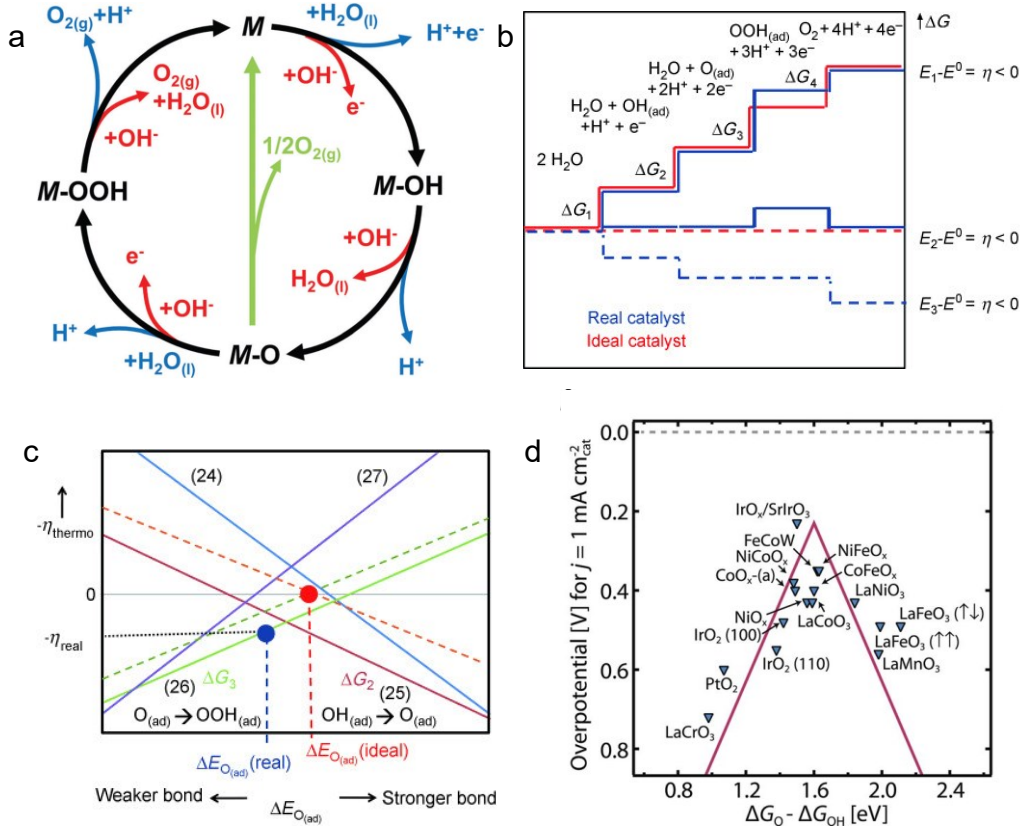


Figure 2. 7 (a) The OER mechanism for acid (blue line) and alkaline (red line) conditions.^[2] The black line indicates that the oxygen evolution involves the formation of a peroxide ($OOH_{(ad)}$) intermediate (black line) while another route for the direct reaction of two adjacent oxo ($O_{(ad)}$) intermediates (light green line) to produce oxygen is possible as well. (b) Gibbs free energy of reactive species and intermediates (horizontal lines) of the OER versus the reaction coordinate at three different electrode potentials.^[139] (c) The thermodynamic overpotential associated with elementary steps of the OER and the total energy of adsorption at the reversible electrode potential on a real and ideal catalyst surface. ΔG_i denotes the free reaction energy of the two elementary reactions steps and the order is $\Delta G_3 > \Delta G_1 = \Delta G_2 > \Delta G_4$.^[139] (d) OER volcano plot for metal oxides.^[3]

The sign of ΔG , free reaction energy, indicates the direction of a chemical reaction and determines if a reaction is spontaneous or not. $\Delta G=0$: the system is at equilibrium and there is no net change either in the forward or reverse direction. If $\Delta G > 0$, the reaction

is nonspontaneous and external energy is crucial for the reaction to begin. On the contrary, if $\Delta G < 0$, the reaction is spontaneous and happens without any external energy. **Figure 2. 7b** shows the free energy diagram for the real and ideal catalyst of reversible oxygen-involving reactions (OER/ORR) at various electrode potentials (E_1 , E_2 , and E_3).^[139] At electrode potential E_1 , all are uphill for either steps and hence OER can not proceed ($\Delta G_i > 0$). At the reversible potential of E_2 , ΔG_3 , which is the thermochemically least favorable step for the real catalyst for the formation of the peroxide intermediate, remains positive, hindering the OER. At the electrode potential E_3 , all ΔG_i shows negative, provided the kinetic limitations are negligible and the OER can occur. Thus, the ΔG_3 is the rate-determining step, which is the formation of the $\text{OOH}_{(\text{ad})}$ state. **Figure 2. 7c** shows the linear relations between the negative thermodynamic overpotential for all four elementary steps on a real and ideal catalyst surface. This phenomenon reflects the Sabatier principle,^[140] which is a general explanatory paradigm in electrocatalysis. According to this principle, the ideal catalyst should bind the reaction intermediates not too weakly or too strongly. Thus, the overall maximum free energy difference can be lowered, and the reaction kinetics can be faster by mediating the strength of adsorption of reaction intermediates. If the binding energy of the active site to oxygen is too weak, the activity is limited by proton-electron transfer to $\text{O}_{(\text{ad})}$ or $\text{OH}_{(\text{ad})}$. On the other hand, if the binding energy is too strong, the activity is limited by proton-electron transfer to $\text{O}_{2(\text{ad})}$ (associative mechanism) or by splitting of the O-O bond in O_2 (dissociative mechanism). **Figure 2. 7d** summarizes the most efficient electrocatalyst for OER from the reported results by Jaramillo's group.^[3] The most efficient electrocatalysts for the OER are generally based on metal oxides and hydroxides. Volcano plots for the OER have been constructed for a wide variety of metal oxide surfaces, especially the non-precious metals, Fe, Ni, Co, W, Mo, and its complex, which is cheap and highly efficient for the reaction.^[141]

2.7. Background of 2D NiFe LDHs for OER

The OER has been extensively studied in the past decades, and various catalysts have been designed to improve the OER kinetics under different electrolyte environments. To the best of our knowledge, as mentioned in Chapter 2.6, the mechanism of water oxidation usually follows the rule of 4-electron transfer steps from the theoretical research.^[4, 7, 139, 142] Researchers need more in-situ techniques to monitor and confirm the reaction pathway of the OER.^[143, 144] As mentioned, transition metal oxides or hydroxides (e.g., NiFe LDHs) have been employed for almost all of the electrocatalytic OER processes.^[63, 107, 145-151] However, most pristine LDHs exhibit unsatisfactory performance compared to benchmark electrocatalysts due to their limited activity and poor conductivity. As summarized in **Figure 2. 8**, there are four strategies to enhance the OER activity of 2D NiFe LDHs, including synthesizing of nanocarbon/LDHs mixtures, synthesizing LDHs with controllable structures, synthesizing multi-metal LDHs, and exfoliate the LDHs bulk into monolayers. First, the combination of LDHs with conducting materials, e.g., carbon nanomaterials, have shown to be a promising way of overcoming their inherently poor electrical conductivity ability. The nanocarbon, such as graphene and carbon nanotubes, were induced in the LDHs system by in-situ^[152] or self-assembly^[33] methods. When used as current carriers, graphene and carbon nanotubes increased the conductivity of the LDHs and led to an OER performance enhancement. More importantly, it was found that the combination of coupling the LDHs with carbon supports and defect engineering can trigger the synergistic effects which can greatly improve OER performance.^[38] Second, for the intrinsic activity of each active site, the higher index surfaces have higher OER activity than the natural (001) facet following density functional theory (DFT) calculations,^[32, 129, 153, 154] which means designing and synthesizing the catalyst with special crystal planes is an effective way to improve the OER activity. It was found that the LDHs with controllable structures, more edges, show better conductivity, and enhanced electrocatalytic activity toward oxygen evolution.^[155, 156] Besides, the strategies for inducing the oxygen vacancy^[157] and forming single-atom catalysts in LDHs^[158, 159] are

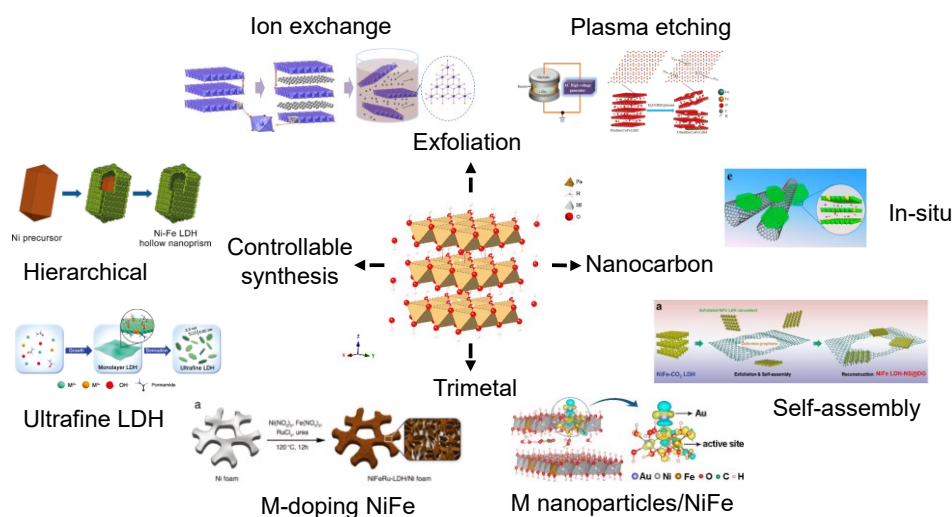


Figure 2. 8 Strategies to enhance the OER activity based on 2D NiFe LDHs by synthesizing controllable structures (hierarchical^[155] or ultrafine^[156] structure); synthesizing nanocarbon/LDHs (in-situ^[152] or self-assembly^[33] methods); synthesizing multi-metal LDHs (doping^[160] and gold modification^[159]) and exfoliation of LDHs (ion exchange^[19] or etching-assisted^[43] methods).

Apart from improving the conductivity and intrinsic activity of each active site of LDHs, exfoliation is another efficient method to enhance the OER by increasing the number of active sites.^[3, 19] A series of ultrathin monolayer or few-layer LDH nanosheets were successfully synthesized from the exfoliation of bulk LDHs. For example, Song et al. reported that monolayer LDHs have superior OER performance in alkaline media compared to bulk LDHs.^[19] The monolayer nanosheets exhibited significantly higher OER catalytic activity compared to their bulk phases, owing to their increased number of active sites and improved electronic conductivity. The exfoliation process can be carried out by ion exchange,^[19, 33-39] liquid phase,^[40] acid/alkali solution etching,^[41, 42]

water-plasma etching,^[43] and argon-plasma etching^[44] methods. Comparisons of the reported exfoliated methods and their trials to exfoliate LDHs are exceptionally laudable, yet typically labor-intensive and time-consuming, toxic, and suffering from strong adsorption of solvent molecules on the surface of the as-exfoliated LDH nanosheets.

In general, the LDHs can be prepared directly by electrodeposition,^[32, 163, 164] coprecipitation,^[165, 166] or hydrothermal method^[19, 152, 160, 167, 168] in a mixed metal salts solution. Compare to electrodeposition and co-precipitation methods, the hydrothermal method has the following advantages for research, e.g., one-step synthetic procedure, environmental friendliness, good repeatability, and controllability. The hydrothermal method was used to synthesize the LDHs in a Teflon-lined stainless-steel autoclave with precursors containing mixed metal salts and hydrolysis reagents. Urea,^[19, 159, 160, 169] dimethylformamide (DMF),^[170, 171] hexamethylenetetramine (HMT),^[39, 104, 172] formamide,^[156, 173] and even 2-mercapto-5-nitrobenzimidazole (MNBI)^[30] were typical hydrolysis reagents used. As summarized in **Table 1**, the reported recipes are almost similar. The NiFe LDHs can be obtained through the hydrothermal method by using the urea at 120 °C or by using HMT at a lower temperature (90-100 °C), respectively. The obtained samples usually have LDHs structure with a CO_3^{2-} as intercalated anions, which own a small interlayer spacing. The LDHs monolayers can be obtained after suffering from the complex processes mentioned before. For example, it was found that several inorganic anions, such as NO_3^- and ClO_4^- , are effective to replace the CO_3^{2-} anions in LDH layered bulk crystals during the ion exchange process, leading to an efficient exfoliation of the bulk into monolayers.^[92, 174] However, there are few researches focused on the possible effect of the hydrolysis agents on the LDHs during the hydrothermal process, such as the interlayer spacing changing of the LDHs. In this dissertation, one of the goals is to present a strategy to prepare 2D NiFe LDHs, with a large interlayer spacing, which can be directly exfoliated into monolayers. The possible effect of hydrolysis agents on the

LDHs will be discussed, including, the interlayer spacing changing of structure, the prerequisite of synthesis, and the universality of the strategy.

Table 1 A summary of NiFe-based LDHs prepared through the hydrothermal method by using urea, HMT, and formamide as hydrolysis agents. M_1/M_2 represents the ratio of divalent to trivalent metal ions. NH_3/M represents molar ratio of ammonium ion to metal ions.

NO.	Catalyst	Recipes	Conditions	M_1/M_2	Hydrolysis	NH_3/M	Ref
1	NiFe LDH/Ni	1 mmol $Ni(NO_3)_2$ and 1 mmol $Fe(NO_3)_3$	120 °C 12 h	1:1	Urea	5	[169]
2	NiFeRu LDH/Ni	0.3 mmol $Ni(NO_3)_2 \cdot 6H_2O$, 0.24 mmol $Fe(NO_3)_3 \cdot 9H_2O$, 0.06 mmol $RuCl_3 \cdot xH_2O$	120 °C 12 h	1:1	Urea	6.667	[160]
3	NiFe LDH/Ni foam	0.66 mmol $NiCl_2 \cdot 6H_2O$ 0.33 mmol $FeCl_3 \cdot 9H_2O$ and 10 mmol $CO(NH_2)_2$	120 °C 12 h	2:1	Urea	20	[175]
4	NiFeV LDH	0.6 mmol $NiCl_2 \cdot 6H_2O$, 0.1 mmol $FeCl_3 \cdot 6H_2O$, and 0.1 mmol VCl_3	120 °C 12 h	3:1	Urea	10	[176]
5	NiFe LDH/Ni foam	0.5 mmol $Ni(NO_3)_2 \cdot 6H_2O$, 0.5 mmol $Fe(NO_3)_3 \cdot 9H_2O$, and 5 mmol $CO(NH_2)_2$	120 °C 12 h	1:1	Urea	10	[177, 178]
6	NiFe LDH	0.25 mmol $Fe(NO_3)_3 \cdot 9H_2O$, 0.75 mmol $Ni(NO_3)_2 \cdot 6H_2O$, and 1.25 mmol $CO(NH_2)_2$	120 °C 10 h	3:1	Urea	2.5	[167]
7	NiFe LDH	0.75 mmol $Ni(NO_3)_2 \cdot 6H_2O$, 0.15 mmol $Fe(NO_3)_3 \cdot 9H_2O$, and 1.8 mmol of $CO(NH_2)_2$	120 °C 10 h	5:1	Urea	2	[179]
8	NiFe LDH	0.29 g $Ni(NO_3)_2 \cdot 6H_2O$, 0.4 g $Fe(NO_3)_3 \cdot 9H_2O$, and 0.6 g $CO(NH_2)_2$	120 °C 10 h	1:1	Urea	5	[168]

9	NiFe LDH	735.0 mg $\text{Ni}(\text{NO}_3)_2 \cdot 6\text{H}_2\text{O}$, 340.0 mg $\text{Fe}(\text{NO}_3)_3 \cdot 9\text{H}_2\text{O}$, and 9.0 g urea	100 °C 10 h	3:1	Urea	100	[180]
10	NiFe LDH	75 μmol $\text{FeCl}_2 \cdot 4\text{H}_2\text{O}$, 225 μmol $\text{Ni}(\text{NO}_3)_2 \cdot 6\text{H}_2\text{O}$	120 °C 6 h	3:1	Urea	13.33	[181]
11	NiFe LDH	15 mmol $\text{Ni}(\text{NO}_3)_2 \cdot 6\text{H}_2\text{O}$, and 5 mmol $\text{Fe}(\text{NO}_3)_3 \cdot 9\text{H}_2\text{O}$, 7 mmol urea and 12.5 mmol triethanolamine	150 °C 2 days	3:1	Urea	1.325	[19]
12	NiFe LDH	0.5 mmol $\text{Ni}(\text{NO}_3)_2 \cdot 6\text{H}_2\text{O}$, 0.5 mmol $\text{Fe}(\text{NO}_3)_3 \cdot 9\text{H}_2\text{O}$, and 2.5 mmol urea	120 °C 12 h	1:1	Urea	5	[182]
13	NiFeCr LDH	0.075 mmol $\text{FeCl}_2 \cdot 4\text{H}_2\text{O}$, 0.225 mmol $\text{Ni}(\text{NO}_3)_2 \cdot 6\text{H}_2\text{O}$, 0.0375 mmol $\text{Cr}(\text{NO}_3)_3 \cdot 9\text{H}_2\text{O}$, 1.688 mmol urea	120 °C 6 h	2:1	Urea	5	[183]
14	NiAl LDH	0.9 mmol $\text{NiCl}_2 \cdot 6\text{H}_2\text{O}$ and 0.3 mmol $\text{AlCl}_3 \cdot 6\text{H}_2\text{O}$	180 °C 24 h	3:1	Urea	5.333	[184]
15	CoAl LDH	10 mmol $\text{NiCl}_2 \cdot 6\text{H}_2\text{O}$, 5 mmol $\text{AlCl}_3 \cdot 6\text{H}_2\text{O}$, and 15 mmol urea	190 °C 48 h	2:1	Urea	2	[34]
16	NiFe	0.77 mmol $\text{Ni}(\text{NO}_3)_2 \cdot 6\text{H}_2\text{O}$, 0.11 mmol $\text{Fe}(\text{NO}_3)_3 \cdot 9\text{H}_2\text{O}$, 4 mmol urea and 1.6 mmol NH_4F	120 °C 6 h	7:1	Urea	9.1	[159]
17	ZnNiFe	0.15 mmol $\text{Ni}(\text{NO}_3)_2 \cdot 6\text{H}_2\text{O}$, 0.05 mmol $\text{Fe}(\text{NO}_3)_3 \cdot 9\text{H}_2\text{O}$ and 0.05 mmol $\text{Zn}(\text{NO}_3)_2 \cdot 6\text{H}_2\text{O}$, 0.66 mmol urea in 80mL H_2O	120 °C 24 h	4:1	Urea	5.28	[185]

18	NiFe LDH	0.75 mmol, $\text{Ni}(\text{NO}_3)_2 \cdot 6\text{H}_2\text{O}$, 0.25 mmol $\text{Fe}(\text{NO}_3)_3 \cdot 9\text{H}_2\text{O}$, and 5 mmol urea	120 °C 12 h	3:1	Urea	10	[172]
19	FeNi LDH	0.4 mmol FeCl_3 and 1.2 mmol NiCl_2	150 °C 24 h	1.2:1	Urea	4.6667	[38]
20	NiFe LDH	0.75 mmol $\text{Ni}(\text{NO}_3)_2 \cdot 6\text{H}_2\text{O}$, 0.25 mmol $\text{Fe}(\text{NO}_3)_3 \cdot 4\text{H}_2\text{O}$, 3 mmol urea, and 3 mmol NH_4F	140 °C 4 h	3:1	Urea	6	[186]
21	NiFe LDH	7.5 mmol $\text{NiCl}_2 \cdot 6\text{H}_2\text{O}$ and $\text{FeCl}_2 \cdot 4\text{H}_2\text{O}$, 60 mmol HMT	Refluxed 6h	2:1 3:1 4:1	HMT	8	[39]
22	NiMn LDH	0.5 mmol $\text{NiCl}_2 \cdot 6\text{H}_2\text{O}$, 0.25mmol $\text{MnCl}_2 \cdot 4\text{H}_2\text{O}$ H_2O_2 (30 wt%, 56.6 μL), 1.5 mmol NaCl , and 4.5 mmol HMT	90 °C 4 h	2:1	HMT	23	[187]
23	NiFe LDH	37.5 mM $\text{Ni}(\text{NO}_3)_2 \cdot 6\text{H}_2\text{O}$, 12.5 mM $\text{Fe}(\text{NO}_3)_3 \cdot 9\text{H}_2\text{O}$, and 20 mL of 23 vol.% formamide	80 °C	3:1	Formamide	2.31	[156, 188]

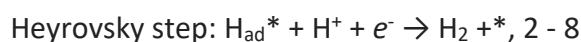
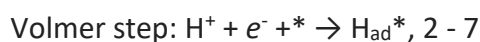
2.8. Features of 2D monolayer

2D LDHs monolayers have attracted tremendous research interest since their widely applications. Most notably, LDHs monolayers are expected to serve as highly efficient OER electrocatalysts due to an increase of active sites number.^[152] Similarly, all 2D monolayers have peculiar features, such as anisotropy, ultra thinness, layer-dependency property, and so on. The surface atoms of 2D monolayers are almost completely exposed, and the atom utilization efficiency is greatly improved compared with bulk materials. The 2D monolayer can be chemically inert, or it can be chemically modified at any time. For instance, the band structure and electrical properties of graphene can be easily regulated by thickness control and element doping.^[189-191]

To sum up, there are three main advantages of the 2D monolayers: (1), the catalytic and electrical properties can be easily tuned by elements doping or chemical modification; (2), the electron transfer is efficient and more sensitive to the external field, which is beneficial to improve the performance of electronic devices and investigate the intrinsic property; (3), highly flexibility and transparency, attractive prospects in wearable smart devices, energy conversion/storage, and other fields.

2.9. Hydrogen evolution reaction

Hydrogen is an ideal energy carrier and an important industrial feedstock for petroleum refining, fertilizer industry, and future transport (such as automotive applications).^[192] It can be effectively produced through HER of water splitting. As shown in **Figure 2. 9a**, the HER is a two-electron three-step transfer reaction with a catalytic intermediate in an acidic, neutral or alkaline medium. For example, in acidic medium, two types of possible pathways have been proposed for transforming protons into hydrogen ($2\text{H}^+ + 2\text{e}^- \rightarrow \text{H}_2$), namely, the Volmer-Heyrovsky or the Volmer-Tafel mechanism (**Figure 2. 9a**):



The asterisk (*) denotes an active site on the catalyst surface and H_{ad}^* indicates a hydrogen atom adsorbed on an active site. These two pathways have the same start, that is the electrochemical hydrogen adsorption step (Volmer step, Equ. 2 - 7), in which an electron transfer to the electrode is coupled to proton adsorption on an empty active site of the electrode to yield an absorbed hydrogen atom (H_{ad}^*). Subsequently, the molecular hydrogen (H_2) formation will be produced via the Heyrovsky reaction (Equ. 2 - 8) or the Tafel reaction (Equ. 2 - 9) depending on H^* surface coverage.^[193] If the coverage of H^* is low, a solvated proton from the solution

reacts with the adsorbed hydrogen (H_{ad}^*) and an electron simultaneously to form H_2 through the Volmer-Heyrovsky mechanism (Equ. 2 - 8). While according Volmer-Tafel mechanism (Equ. 2 - 9), two adsorbed hydrogens (H_{ad}^*) intermediates tend to bond together to form an H_2 molecule if the H^* coverage is high.

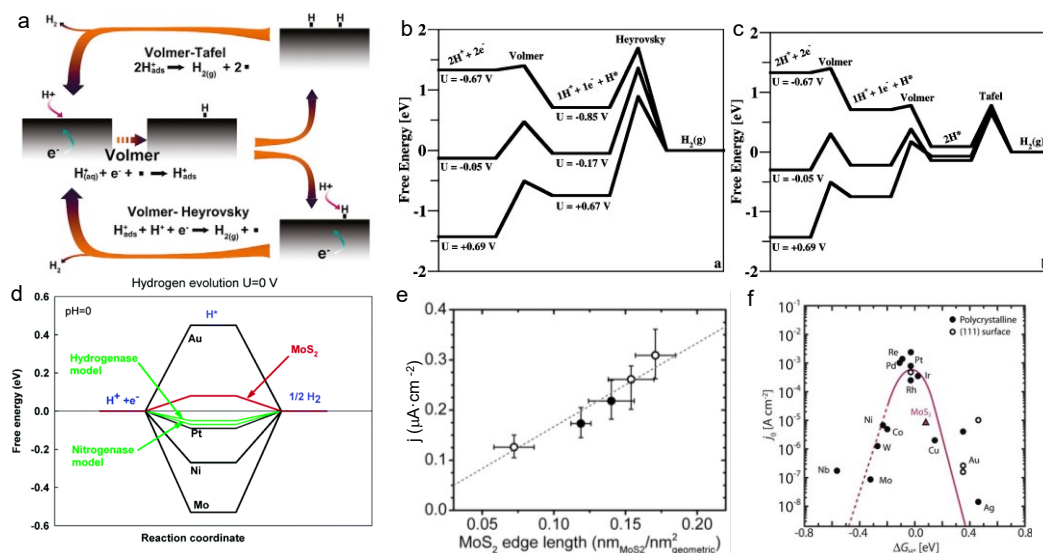


Figure 2. 9. Mechanisms and activity trend of HER catalysis. (a) The mechanism of hydrogen evolution on the surface of an electrode in acidic solutions.^[118] Standard free energy diagram for the (b) Volmer-Heyrovsky and (c) Volmer-Tafel route on Pt (111).^[194] (d) Calculated free energy diagram for hydrogen evolution at a potential $U = 0$ relative to the standard hydrogen electrode at $pH = 0$.^[120] (e) Exchange current density versus MoS_2 edge length.^[119] (f) The Sabatier plot for HER catalysts shows the exchange current densities plotted against the free energy of hydrogen adsorption for metals and MoS_2 .^[3]

To present the possible reaction-rate limiting steps, the reaction free-energy diagrams of HER were proposed from a theoretical perspective. Based on the three elementary HER/HOR steps (Volmer-Heyrovsky/Volmer-Tafel) as well as the reactions barriers, the standard free energy diagrams on Pt (111) were constructed under different applied electrode potentials (**Figure 2. 9b, c**).^[194] The reaction barriers and the free energy level of each reaction step are different in both Heyrovsky and Tafel steps, leading to a different overall reaction rate. With the development of computational methods and technologies, theoretical calculations have the potential to provide more in-depth

information on electrochemical processes.^[6, 195] To explore the effects of various materials on HER activity, the free energy diagrams for hydrogen evolution have been constructed by computational calculations for metals (Au, Pt, Ni, and Mo) and MoS₂ (**Figure 2. 9d**). From the calculated free energy diagram, the value of atomic hydrogen bonding to the MoS₂ edge is close to Pt, raising the possibility of MoS₂ as a promising HER electrocatalyst in theory. Moreover, the results have been supported by experimental results confirming that the MoS₂ edge displays an excellent HER activity (**Figure 2. 9e, f**).^[119, 196] The current density increased with the MoS₂ edge length (**Figure 2. 9e**). As summarized in **Figure 2. 9f**, compared to the precious metal, the MoS₂ has a huge potential application for HER that a series of studies have been conducted to enhance MoS₂'s catalytic performance by creating more edge sites and activating the basal plane.^[69, 118, 197, 198]

2.10. Background of 2D MoS₂ monolayer for HER

2D TMDs electrocatalysts are recognized as greatly promising alternatives for noble-metal-based catalysts (such as Pt) in HER.^[199] As mentioned, the edge site activity of 2D MoS₂ for HER was first predicted by DFT calculation,^[120, 200, 201] and then proven in several experimental studies.^[119, 202] However, such catalytic activity was shown to be anisotropic, with the basal plane of the 2D MoS₂ nanosheet being relatively inert. The activity of the 2D MoS₂ nanosheet can also be affected by phase engineering,^[18, 203] vacancy,^[198, 204] and strain engineering.^[198] In the past decades, significant progress has been achieved and reviewed in TMDs for electrocatalytic hydrogen evolution: MoS₂ and other TMDs,^[205-207] TMDs/compounds,^[118, 208, 209] TMDs nanomaterials,^[106, 108, 210] and computational approaches.^[211] However, most of those studies were focused on TMDs composites to improve the HER performance and its potential application of sustainable energy, such as fuel cells.^[212] Fewer studies are focused on 2D MoS₂ monolayer for HER because not all laboratories can integrate materials, electrochemistry, and microfabrication. Similar but different from the 2D NiFe LDHs, as discussed in Chapter 2.2, MoS₂ bulk not only can be exfoliated into nanosheets in

solvents,^[29, 45, 80-82] (n-BuLi)^[18, 83], and tetraethylammonium bromide (THAB)^[26] by liquid-exfoliated methods, but also can be exfoliated through a micromechanical cleavage with scotch tape,^[28, 70, 71] layer-resolved splitting nickel,^[72] and gold tape.^[73-79]

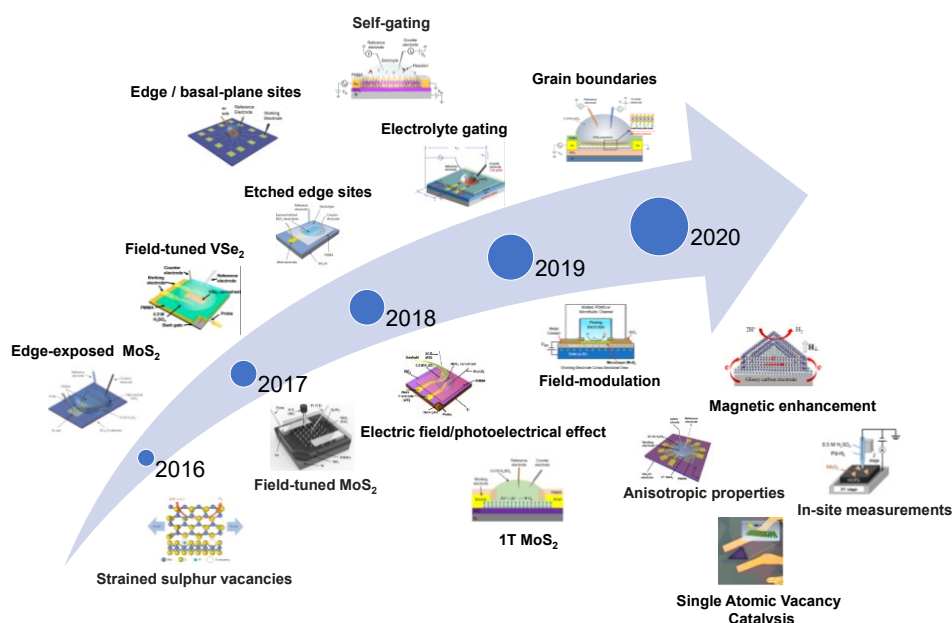


Figure 2. 10 On-chip MoS_2 HER reactors. Development history of on-chip electrocatalytic microdevices. Strained sulphur vacancies,^[198] and edge-exposed MoS_2 ^[20]; field-tuned MoS_2 nanosheets,^[213] field-tuned VSe_2 nanosheets,^[214] and edge and basal-plane sites^[215]; etched MoS_2 edge sites,^[216] edge/basal plane sites,^[21] electric field and photoelectrical effect,^[217] 1T- MoS_2 ^[22]; self-gating,^[23] electrolyte gating,^[218] anisotropic properties,^[219] field-modulation,^[220] and single atomic vacancy catalysis^[204]; grain boundaries,^[221] magnetic enhancement,^[222] and in-site measurement.^[223]

Compared to the exfoliated method of 2D TMDs nanosheets in liquid, the 2D TMDs nanosheets, exfoliated with a micromechanical cleavage tape, usually have a large area, high-quality, which can be used to fabricate on-chip reactors. These on-chip reactors provide an ideal platform to demonstrate unique advantages in the direct probing of many HER processes to obtain previously inaccessible information and to investigate the catalytic property of the TMDs. Therefore, in subsequent research, the structural advantages of this HER reactor model were constantly expanded and

enriched as a powerful tool to discover novel phenomena and clarify HER fundamentals at the nanoscale. A brief overview of the TMDs electrocatalyst as on-chip HER reactors is presented in **Figure 2. 10**. A series of on-chip HER reactors were fabricated for exploring the electrocatalytic hydrogen evolution, involving edges/basal plane activity,^[20, 21, 215, 216] vacancy catalysis activity,^[198, 204] phase engineering,^[22] grain boundaries activity,^[221] the field-effect tunable catalytic activity,^[23, 213, 214, 218, 220], electric field and photoelectrical effect,^[217] anisotropic properties,^[219] magnetic enhancement,^[222] and in-site measurement.^[223] All of the results confirm that the on-chip TMDs HER reactors were ideal platforms for expanding the insight into electrochemical processes.^[224] In this dissertation, the temperature-dependent HER property of on-chip monolayer MoS₂ will be investigated.

3. Materials and methods

Based on the fundamentals mentioned in Chapter 2, the methods for preparation and exfoliation of 2D materials will be presented here. In this Chapter, it will be given in details, such as the preparation (synthesizing and exfoliation), characterization (equipment), and application (electrochemical parameters) of 2D materials.

First, a new kind of NiFe LDHs with large interlayer spacing was synthesized through a one-pot hydrothermal method (bottom-up synthesis in **Figure 3. 1**), and MoS₂ ML were obtained directly through mechanical cleavage from the bulk crystals (top-down exfoliation in **Figure 2. 2**). The electrodes were fabricated by using photolithography (**Figure 3. 2**) and electron beam (e-beam) evaporation technologies (**Figure 3. 3**). Then, in order to characterize the structure of the 2D bulk and exfoliated 2D nanosheets, advanced characterization methods have been applied, including SEM, TEM, XPS, XRD, Raman, PL, FT-IR, and AFM. Lastly, all the electrochemical tests were performed by an electrochemical station (Metrohm Autolab) with a three-electrode system to evaluate the OER/HER activity of the exfoliated 2D monolayer nanosheets. Electrode activity, overpotential (η), Tafel slope (b), cyclic voltammetry (CV), geometric activity (j), turnover frequency (TOF), electrochemical impedance spectroscopy (EIS), and stability have been analyzed.

3.1. Materials preparation and device fabrication

In this section, the original materials, the synthesis methods, and the exfoliation process of 2D monolayers are listed and discussed. The electrodes were fabricated with photolithography and e-beam evaporation technologies.

3.1.1. Materials

All chemicals were used as received without any further purification. All the reagents were of analytical grade. All solutions were prepared with deionized (DI) water (resistance 18.2 M Ω ·cm at 25°C) from a Millipore deionized water system. Ni(NO₃)₂·6H₂O, Co(NO₃)₂·6H₂O, Fe(NO₃)₃·9H₂O, ruthenium(III) chloride hydrate (RuCl₃·xH₂O), gold(III) chloride trihydrate (HAuCl₄·3H₂O), ruthenium oxide (RuO₂), potassium chloride (KCl) potassium iodide/iodide (KI/I₂), hexamethylenetetramine (HMT, C₆H₁₂N₄), urea ((NH₂)₂CO), H₂SO₄ and 5 wt% of Nafion solution were purchased from Sigma-Aldrich. 2D MoS₂ crystals were purchased from SPI Supplies. Potassium hydroxide (KOH), dimethyl sulfoxide (DMSO), acetone, and isopropanol were purchased from VWR chemicals.

3.1.2. Synthesis of NiFe LDHs monolayer

The NiFe LDHs were synthesized through a one-pot hydrothermal method. The oven and hydrothermal reactor are displayed in **Figure 3. 1**. In a typical procedure, Ni(NO₃)₂·6H₂O, Fe(NO₃)₃·9H₂O, and HMT were dissolved in DI water and processed by ultrasound to form a clear solution. Then, the aqueous solution was transferred to a Teflon-lined stainless-steel autoclave (**Figure 3. 1b**), which was sealed and maintained at 95 °C for 24 hours in the oven (**Figure 3. 1a**). After naturally cooling to room temperature, the NiFe LDHs were collected after centrifugation and washed thoroughly with isopropanol 3 times. The NiFe LDHs can be directly exfoliated into monolayers in DI water by shaking or through an ultrasonic process. The bulk NiFe LDHs can be obtained after being dried in the oven at 60 °C (**Figure 3. 1a**).

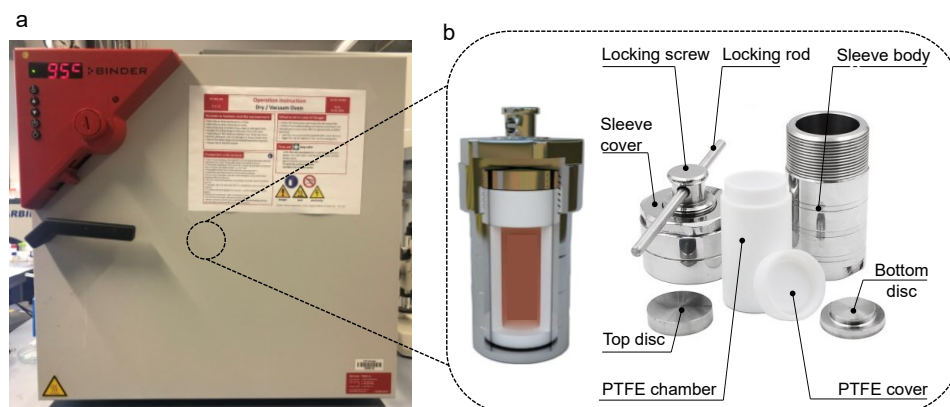


Figure 3. 1 Scheme of the experimental (a) oven and (b) hydrothermal reactor used for carrying out the NiFe LDHs. A hydrothermal reactor is mainly made up of two parts: an outer high-quality stainless-steel jacket and an inner Teflon chamber.

3.1.3. Mechanical exfoliation of MoS₂ monolayer

The MoS₂ ML was mechanically exfoliated with a gold-modified tape.^[73-79] In general, a gold film (Au, 150 nm) was deposited onto an ultra-flat silicon substrate using a template-stripping method.^[225] The prepared gold layer was picked up with a thermal release tape (TRT). Then, the TRT/Au tape was gently pressed onto a freshly cleaved natural single-crystal bulk MoS₂ (SPI Supplies). The gold surface is attached to the crystal surface. As the TRT/Au tape was lifted off the surface, the Au layer with a 2D MoS₂ ML was obtained (TRT/Au/MoS₂ ML), and it was further transferred onto the desired substrate, such as a silicon wafer (Si/SiO₂) and a TRT/Au/MoS₂ ML/substrate was obtained. The TRT was removed by heating at 120 °C for two minutes. The substrate covered by the Au layer (Au/MoS₂ ML/substrate) was cleaned by O₂ plasma to remove any remaining polymer residues. The Au layer was dissolved in a KI/I₂ gold etchant solution. The silicon wafer with MoS₂ ML (MoS₂ ML/substrate) was obtained after being rinsed with DI water, isopropanol, and dried with N₂. The MoS₂ ML/substrate was annealed at 300 °C for 2 h with N₂ gas protection to increase the adhesion force to the substrate.

3.1.4. Photolithography

Substrates (e.g., Si/SiO₂) were cleaned with immersion in DMSO, acetone, and isopropyl alcohol; degassed on a hotplate (120 °C for 2 minutes), and the substrates were cleaned in O₂ plasma. In this work, several commercial photoresists were used. First, an image reversal photoresist AZ5214E was spun onto the individual substrate at 4500 rpm for one minute (thickness: 1.4 μm). Soft baking at 90 °C for 4 minutes. Patterning was performed by a mask less aligner (MLA100, Heidelberg Instruments Mikrotechnik GmbH, Heidelberg, Germany). As illustrated in **Figure 3. 2**, after patterning, the resist was inverted by a two-minute post-baking at 120 °C and flood exposure. After the development procedure, its pattern has an undercut profile, which enables the physically deposited nanomembrane to be easily lifted off from the substrate (**Figure 3. 2**). Moreover, another kind of negative SU-8 photoresist, an epoxy resin, and near-ultraviolet photoresist, is used. The new chemically amplified negative image SU-8 photoresist overcomes the problem of the insufficient aspect ratio of ordinary photoresists when using UV lithography and is very suitable for preparing high aspect ratio microstructures. It has low light absorption in the range of near-ultraviolet light (365 – 400 nm), and the exposure of the entire photoresist layer is uniform. Thick film patterns can be obtained with vertical sidewalls, high aspect ratios, good mechanical properties, chemical resistance, and thermal stability.

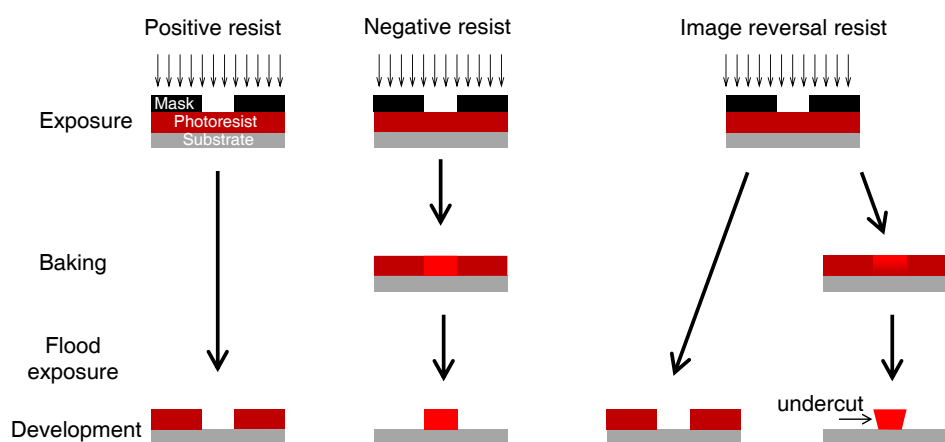


Figure 3. 2 Schematic of technologies of photolithography.

3.1.5. Electron beam evaporation

Electron beam evaporation, also known as e-beam evaporation, is a mature technology for preparing metal and metal oxide thin film. As shown in **Figure 3. 3**, the e-beam evaporator usually consists of an electron source, a crystal detector (quartz crystal microbalance (QCM) monitor), a sample holder with shutter, a crucible with a target, and a water-cooling system (do not display). In the high vacuum (10^{-6} - 10^{-8} mbar) chamber, an electron beam can be generated by applying a high voltage in the electron source which is then focused onto the target material in the crucible by using a magnetic field. Thus, the thermally heated target material is evaporated onto the top substrate in an atomic form. Simultaneously the thickness and deposition rate of the thin film can be monitored by the frequency change in the crystal detector. In this dissertation, e-beam evaporation (Edwards auto 500 FL500, England) was used for the fabrication of the gold film and electrodes (e.g., Au, Cr/Au, Ti/Au, and Cr/Pt).

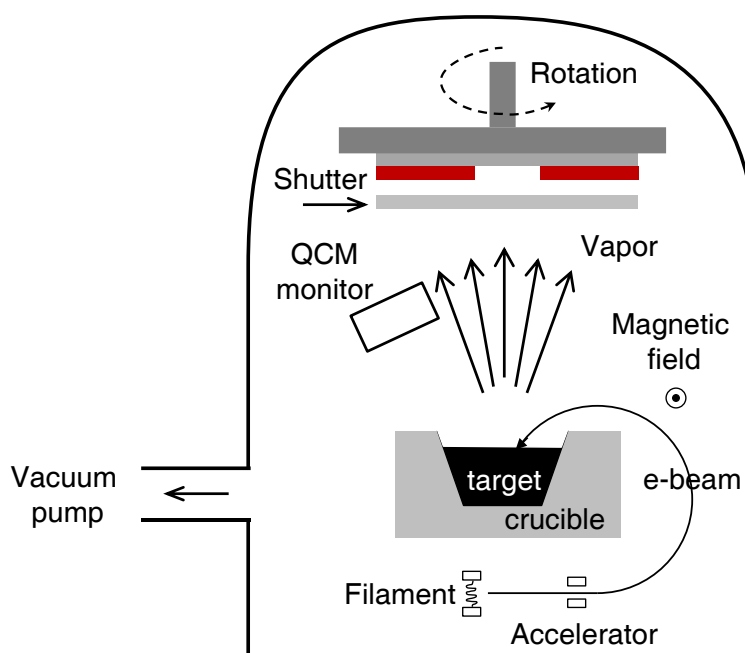


Figure 3. 3 Schematic of the electron beam evaporation system.

3.2. Characterization methods

Different advanced equipments are briefly introduced in this section to check the morphology, structure, structure evolution, chemical composition, element valences, and even the geometry structure (e.g., thickness) of 2D materials.

3.2.1. Scanning electron microscopy

SEM is a precious tool for the analysis of the morphology from nanometer up to micrometer. The morphology of all the products was observed by using a scanning electron microscope (Zeiss DSM982, Gemini) equipped with a field-emission gun at 1 - 5 kV acceleration voltage. Energy-dispersive X-ray spectroscopy (EDS) analysis was performed by an energy dispersive X-ray analysis (EDAX) Genesis instrument. The popularity of SEM can be attributed to many factors: the versatility of its various imaging modes, the excellent spatial resolution, the modest requirement on sample preparation and condition, the relatively straightforward interpretation of the acquired images, and the accessibility of associated spectroscopy and diffraction technologies.

3.2.2. Transmission electron microscopy

TEM is also an electron microscope technology whereby a beam of electrons transmits the thin samples and interacts with them, then an image is formed. Owing to the small wavelength of the electrons, the TEM can provide images with higher resolution than light microscopes for the analysis of the chemical composition, electronic structure, crystal orientation, etc. In this dissertation, the obtained LDHs compounds have been exfoliated easily down to monolayers regime as observed in the HRTEM images. Part of the LDH compounds was grounded by using mortar and pestle and then was dissolved in toluene to obtain the unexfoliated LDHs particles to investigate the crystal structure in the compound. The LDHs nanoflakes for TEM characterizations were then transferred to TEM lacey carbon Cu-grids using a standard pipette. Theoretical

kinematic electron diffraction patterns were applied to index the corresponding electron diffraction patterns. Selected area electron diffraction (SAED) on LDHs nanoflakes was carried out in FEI Tecnai G2 transmission electron microscope (ThermoFisher Comp., US) with LaB6 emitter operated at 200 kV acceleration voltage to investigate the crystal phase of the samples before doing the HRTEM imaging for the samples. The HRTEM imaging and SAED measurements were performed using a double-corrected Titan3 80-300 instrument (FEI Company, USA). The flakes were easily destroyed by the electron beam and therefore the HRTEM images were acquired by using 80 kV acceleration voltage.

3.2.3. X-ray photoelectron spectroscopy

XPS is an efficient technology which always be used to determine the chemical composition and element valences of the samples with a depth between 0 and 10 nm. In this study, XPS spectra were acquired using a PHI-5000C ESCA system, the C1s value was set at 284.8 eV for charge corrections. Thus, high-resolution XPS spectra were obtained with a pass energy of 11.05 eV. The chemical composition and element valences of NiFe LDHs were checked and confirmed. Moreover, the MoS₂ monolayer on a silicon wafer was also characterized by this technology.

3.2.4. X-ray diffraction

XRD (Co K α radiation ($\lambda = 1.7902 \text{ \AA}$), X'Pert PRO MPD, Philips) was used to check the crystal structures, especially, for the interlayer spacing evolution of 2D NiFe LDHs materials. The basal spacing value of the (003) and (006) reflections of NiFe LDHs is calculated and shown further below. According to Bragg's law, which describes the condition on θ for constructive interference:

$$2 d \sin \theta = n \lambda, \quad 3-1$$

where d is the basal spacing, θ is the glancing angle, n is a positive integer and λ is the wavelength of the incident wave. For the same reflections, the relationship between the d and θ should be:

$$2 d_1 \sin \theta_1 = 2 d_2 \sin \theta_2, 3-2$$

where d_1 and θ_1 are 0.78 and 0.39 nm, 13.257 and 26.742° for the (003) and (006) reflections of NiFe LDHs (JCPDS 40-0215), respectively, from the database.^[42, 226] For instance, if the tested glancing angles of θ_2 are 12.5 and 25.5° for the samples. The calculated results for d_2 are 0.82 and 0.41 nm for the (003) and (006) reflections, respectively.

3.2.5. Raman and photoluminescence spectra

Raman spectroscopy is a method used to study the inelastic scattering of light on matter. Monochromatic light, usually choose laser, is used to examine the matter in Raman spectroscopy, giving access to information about modes of rotation, vibrations, spin-flips, or phonons. Photoluminescence (PL) is light emission from any form of matter after the absorption of photons (electromagnetic radiation). Following excitation, various relaxation processes typically occur in which other photons are re-radiated. First, Raman was used to identify the structure and structure evolution of 2D NiFe LDHs. Moreover, the Raman and PL spectra were used to identify the MoS₂ monolayer.^[96, 97] Raman and PL spectra were carried out at room temperature, and the signals were recorded by a LabRAM HR Evolution (Horiba) using a laser with an excitation wavelength of 458 nm. A long working distance (LWD, 10.6 mm) with a 50× objective was used, and the spot size of the laser beam was focused to 0.77 μm. To avoid any thermal effects, the power of the laser incident on the sample was almost 5 kW·cm⁻² for 2 seconds. The thermal effect of monolayer MoS₂ was recorded by adjusting the radiation power from almost 5.4 to 5400 kW·cm⁻² with a filter (from 0.1 to 100 %).

3.2.6. Fourier transform infrared spectroscopy

FT-IR spectroscopy was performed on a Bruker Optics ALPHA-E spectrometer with a universal Zn-Se ATR (attenuated total reflection) accessory in the 400 – 4000 cm^{-1} .

3.2.7. Atomic force microscopy

AFM measurements were collected in a multimode atomic force microscope of Bruker Dimension ICON3 System, using tapping mode in the air at room temperature. Processing and analysis of the images were performed by using the NanoScope Analysis software. In this dissertation, AFM is employed to reveal the topography images of NiFe LDHs monolayer nanosheets, especially the direct evidence of the layer thickness. The height of the NiFe LDHs monolayer nanosheets is around 0.8 nm. The theoretical thickness of a single layer of metal hydroxide is almost 0.4 - 0.5 nm.^[227] The adsorption of the counter-anion layer, such as NO_3^- , on the sheet surface is expected to be about 0.3 nm.

3.3. Electrochemical characterization

The basic parameters of OER and HER will be discussed in this section. All of the electrochemical tests were performed by an electrochemical station (Metrohm Autolab) with a three-electrode system. A silver/silver chloride (Ag/AgCl, in saturated KCl solution) electrode acts as the reference electrode (RE), Pt acts as the counter electrode (CE), and the catalyst/gold electrode acts as the working electrode (WE). During the rotating disk measurement, the catalyst/glassy carbon disk (GCE, 5 mm in diameter) was used as the WE, while platinum foil and mercury/mercury(II) oxide (Hg/HgO) served as the CE and RE, respectively. All data were directly used with iR compensation and all measured potential values were calibrated with RHE by using the following equation: E (versus RHE, V) = E (Hg/HgO) + 0.098 + 0.059 * pH for Hg/HgO,^[228] and E (versus RHE) = E (Ag/AgCl) + 0.197 + 0.059 * pH for Ag/AgCl.^[30] The pH was calibrated to 13.6 for 1M KOH and 0.3 for 0.5 M H₂SO₄.^[30, 159, 229] In the electrochemical half-cell, the concentrations of reactant and product can be linked by the Nernst equation^[230]:

$$E = E^{\circ} + \frac{RT}{nF} \ln\left(\frac{C_o}{C_r}\right), \text{ 3-3}$$

where E° is the thermodynamic voltage of the reaction (also apply to the water splitting in Chapter 2.4), R is the gas constant, T is the temperature, n is the electron transfer number, F is the Faraday constant, and C_o/C_r is the concentration of oxidized/reduced species in the system. To better evaluate and compare the catalytic activity of OER/HER electrocatalysts, some important measurement criteria have been established. The mostly used criteria are linear sweep voltammetry (LSV), exchange current density (j), overpotential (η), Tafel slope (b), cyclic voltammetry (CV), electrochemical double-layer capacitance (C_{dl}), turnover frequency (TOF), and stability. The j can be measured by recording the polarization curves and the Tafel slope can be derived from the polarization curves. These parameters play a key role in obtaining an insight into the mechanism of this electrocatalytic process.

3.3.1. Total electrode activity

The performance of an electrocatalyst is usually evaluated by using two metrics: apparent electrode activity and the intrinsic activity of each catalytic site, which demonstrate the intrinsic activity of the catalyst.^[5] The exchange current of the electrode obtained from LSV reflects the total electrode activity in the process of OER/HER. LSV is a voltammetric method where the current at a WE is measured while the potential between the WE and the RE is swept linearly in time. In this work, the LSV was conducted with a scan rate of 5 mV s⁻¹ in 1 M N₂-saturated KOH for OER or in 0.5 M N₂-saturated H₂SO₄ for HER. The magnitude of intercepts at $\eta = 0$ refers to exchange current (i). For the apparent electrode activity (e.g., current density), it is customary to divide exchange current (i) by the area of the electrode (A) (Equ. 3 - 4). The exchange current (i) becomes the exchange current density (j). Higher exchange current density is usually an indication of a better catalytic performance of electrocatalyst for a target reaction. For the calculations of areal activity, reported methods are followed,^[230] which can be expressed as,

$$j \text{ (mA cm}^{-2}\text{)} = i/A, \text{ 3 - 4}$$

areal current density (mA.cm⁻²) was calculated by normalizing the current at an overpotential value. The amount of catalyst loadings is 6 and 30 μ g for exfoliated LDHs monolayer nanosheets and the LDHs or RuO₂ powder, respectively.

3.3.2. Overpotential

Overpotential (η) is another most important descriptor to evaluate the performance of the electrocatalysts. In an ideal condition, the applied potential for driving a specific reaction should be equal to the thermodynamic voltage. As discussed in Chapter 2.4, in reality, the applied potential is commonly much higher or lower than that at equilibrium to overcome the electrode kinetic barrier of the reaction.

$$E = E^0 + \eta, \text{ 3-5}$$

The η , as illustrated in Equ. 3-5 and **Figure 2. 5d**, is a difference between the applied potential (E) and potential under thermodynamic voltage (E^0). The different current densities will be referred to as different η values. The η is commonly referred to as a value that has been applied to achieve a specified current density, such as the η at a benchmarking current of 10 mA cm^{-2} is measured after normalization and reported as one of the primary screening parameters. A lower overpotential of an electrocatalyst in the system indicates its superior electrocatalytic ability for the target reaction.

3.3.3. Tafel equation

Tafel equation is an equation in electrochemical kinetics relating the rate of an electrochemical reaction to the η ,^[193] which is logarithmically related to the j :

$$\eta = a + b \log j, \text{ 3-6}$$

where b is the Tafel slope. From the Tafel equation, two important parameters, b , and j can be derived. The value of the b can be obtained by fitting with the Tafel equation, which is the most common way to get this value. The b is generally related to the catalytic mechanism of the electrode reaction, whereas j , which is obtained when η is assumed to be zero, describes the intrinsic catalytic activity of the electrode material under equilibrium conditions. A better catalytic material possesses a higher j and a smaller b . A smaller value of the b means that increasing the same current density required smaller overpotential, implying a faster charge transfer kinetic. This is the reason why it is often used as a primary activity parameter in determining the catalytic activity.

3.3.4. Cyclic voltammetry and double-layer capacitance

CV, a widely used potential-dynamic electrochemical technology, can be employed to obtain qualitative and pseudo-quantitative data about electrochemical reactions including electrochemical kinetics, reaction reversibility, reaction mechanisms, electrocatalytic processes, and effects of electrode structures on these parameters.

The principle of this technology is to measure the resulting current under a linear voltage ramp to an electrode between two voltage limits. The electrochemical double-layer capacitance (C_{dl}), which is in proportion to the electrochemical active surface area (ECSA), was calculated by measuring the CV curves in the range 1.15 - 1.25 vs RHE without redox processes for NiFe LDHs.

3.3.5. Turnover frequency

TOF is defined as the number of reactants that a catalyst can convert to the desired product per catalytic site per unit of time, exhibiting the intrinsic catalytic activity of an active catalytic site. The TOF value of NiFe LDHs for OER was calculated from the following equation^[30, 39] (Equ. 3-7):

$$\text{TOF} = \frac{j \cdot A}{4 \cdot F \cdot m}, \quad 3-7$$

A is the area of the WE. F is the Faraday constant ($96,485 \text{ C} \cdot \text{mol}^{-1}$), 4 represents 4 electrons per O_2 , and m is the moles of the active materials deposited on the WE. All of the metal atoms in NiFe LDHs are regarded as the active sites, such as Ni, Fe, Co, and Ru atoms, to give a conservative estimate of TOF. The TOF of the MoS_2 monolayer for HER is calculated according to the following equation:

$$\text{TOF} = \frac{j / (2 \cdot q)}{N}, \quad 3-8$$

where $q = 1.6 \times 10^{-19} \text{ C}$ is the elementary charge, and 2 accounts for 2 H atoms per H_2 molecule. To calculate the turnover frequency per surface Mo atom (TOF_{Mo}), the Mo atom density (N_{Mo}) is estimated to be about $1 \times 10^{15} \text{ cm}^{-2}$ from the MoS_2 lattice constant $\sim 3.2 \text{ \AA}$.^[198]

3.3.6. Electrochemical impedance spectroscopy

EIS analysis was performed to study the interfacial properties between the electrocatalysts (electrodes) and electrolytes. The measured impedances were presented in the form of imaginary (Im) vs. real (Re) parts at various frequencies. The high frequency interception of the Re -axis represents the resistance of the electrodes and the width of the semicircle on the Re -axis corresponds to the charge-transfer resistance (R_{ct}), which indicates the overall kinetic effects. In this dissertation, the EIS is recorded at an overpotential of 270 mV over the frequency range from 100 kHz to 0.01 Hz with a modulation amplitude of 10 mV in NiFe LDHs for OER. The Nyquist plots were obtained at frequencies ranging from 100 kHz to 0.1 Hz at an overpotential of -100 mV in MoS₂ monolayers for HER.

3.3.7. Stability measurement

The stabilities of catalysts are of crucial importance for practical applications, especially considering that the OER/HER catalyst mostly works in a strongly oxidative/reductive environment at the pH extremes. There are two methods for characterizing the electrocatalytic stability of the catalysts. One approach is using a chronopotentiometry (i.e., the j - t curve) method, thus, time-dependent current under a constant potential measurement was employed to evaluate the long-term stability of the system. The other method is to conduct the recycling experiment by performing CV or LSV. After hundreds of CV cycling, the less the overpotential for the same current increases, the better the stability of the electrocatalyst is. A current density of 10 mA cm⁻² is often used in this kind of electrolysis because this value is the most frequently used standard in HER electrocatalysis and solar fuel synthesis. The duration can last from several to dozens of hours, and a longer duration means better stability.

4. Experiments and results

This chapter presents the physical and chemical properties of 2D NiFe LDHs and MoS₂ monolayers, and their potential electrocatalytic applications are also discussed.

In Chapter 4.1, a one-pot synthesis strategy (bottom-up synthesis) was proposed to prepare the monolayer NiFe-based LDHs for water oxidation. The structures of LDHs (include the initial and evolution of structure) are checked by advanced characterization methods. The prerequisite to the formation and the universality of this strategy are investigated and confirmed. The NiFe-based LDHs can be easily exfoliated to monolayers in water. The OER performances of the bulk, commercial RuO₂, and exfoliated monolayers are discussed. As a result, the NiFe LDHs monolayer nanosheets show a lower overpotential than that of the NiFe LDHs bulk counterpart and commercial RuO₂. This facile strategy paves the way to design directly exfoliated NiFe-based LDHs for highly active catalysts, and even for energy conversion based on 2D LDHs composites.

In Chapter 4.2, a MoS₂ ML was exfoliated (top-down exfoliation) with a modified gold tape. Then, an on-chip MoS₂ ML HER reactor is designed and fabricated by using photolithography and e-beam deposition methods. The MoS₂ ML was checked by Raman, PL, and XPS spectra. Finally, the relationship between HER performance and the thermal effects of MoS₂ ML is revealed. The details of the exfoliation process, thermal effects, and HER performance at different temperatures of the MoS₂ ML are discussed. The thermal enhanced HER performance of MoS₂ ML was observed on an on-chip device. This result offers a possible way to increase the catalytic performance by evaluating the catalyst at higher-temperature conditions in the future.

4.1. One-pot synthesis of nickel-iron layered double hydroxides monolayer

This section reports the strategy to synthesize a series of 2D nickel-iron LDHs (NiFe LDHs) through a one-pot hydrothermal method. The interlayer spacing of NiFe LDHs can be adjusted by changing the hydrolysis agent (HMT vs. urea). Finally, a new nitrate-intercalated NiFe LDHs was obtained via the one-pot synthesis way, which possesses a large interlayer spacing, resulting in direct exfoliation of bulk into monolayers. The universality of this strategy also allows the extension of NiFe LDHs to NiFe-based multi-metal LDHs by doping or modification. As a result, the NiFe LDHs monolayer nanosheets show better OER performance than that of the bulk counterpart. This facile strategy paves the way to design NiFe-based LDHs monolayers for highly active catalysts, and even for energy conversion based on 2D superlattices LDH-multifunctional materials. The core part of this section has been published in *Advanced Materials Interfaces*, **2022**, 9, 2200973, DOI: 10.1002/admi.202200973, titled: One-Pot Synthesis of Nitrate-Intercalated NiFe Layered Double Hydroxides with an 8.2 Å Interlayer Spacing.

4.1.1. Introduction

As discussed in Chapter 2.6, OER driven by renewable electricity is considered one of the most promising solutions for the development of renewable energy conversion, such as water splitting, regenerative fuel cells, and rechargeable metal-air batteries.^[141, 231] But the OER efficiency is greatly restricted due to the sluggish kinetics of four sequential proton-coupled electron transfer steps, requires conspicuous overpotential (η).^[2, 137] To overcome this challenge, transition metal oxides or hydroxides catalysts are proposed and regarded as promising candidates to accelerate this reaction rate because of their low cost, abundant resources, good chemical stability, and high OER activity.^[63, 107, 149, 232] And the poor catalytic activity and sluggish kinetics originate from the lack of intimate interfacial interaction,

consequently hindering further development of LDHs-based composites for energy conversion and their practical application. Compared with the LDHs bulk materials,^[135, 147, 151, 168, 233-235] thin-layer or monolayer LDHs can boost the OER performance by providing sufficient accessibility to redox-active sites.^[19] Typically, the exfoliation (such as ion exchange exfoliation,^[19, 33-39] liquid-phase exfoliation,^[40] and etching exfoliation,^[41-44, 236] methods) of bulk LDHs, which are synthesized through electrodeposition,^[32, 163, 164] coprecipitation,^[165, 166] or hydrothermal^[19, 152, 160, 167, 168] methods, represents the typical approach to construct thin-layer LDHs. Taking the ion exchange exfoliation method as an example, the anionic organic guests (such as amino acids or surfactants) will be intercalated into the interlayer of LDHs, leading to formate a loosely stacked and highly swollen phase, which can be dispersed in solvents (formamide, butanol, etc.) with an assistance of mechanical cleavage or ultrasonication.^[35, 36, 237] Despite the great success, these exfoliation methods still suffer from challenges of low sample quality (e.g., low crystallinity), lack of thickness control, low purity caused by strongly adsorbed solvent molecules on the LDHs surface, toxicity, labor-intensive, and so on.^[156, 173, 238] Therefore, it is urgently required to develop novel methods for facile synthesis of high-quality thin-layer LDHs.

As previously mentioned, the LDHs can be prepared via a facile hydrothermal method by mixing metal salts and hydrolysis reagents together. The typical recipes were listed in **Table 1** in Chapter 2.7 and the scheme is shown in **Figure 3. 1**. For example, so-called monolayer NiFe LDH nanosheets with small sizes can be prepared directly by using formamide as the hydrolysis reagents,^[156, 173] while NiFe LDH/nanocarbon hybrid can be synthesized in DMF with MNBI.^[30] Those instructive results indicate that the hydrolysis reagents have a great effect on synthesizing of LDHs with different morphologies. However, until now there are few studies related to the structure changing (such as the interlayer spacing distances) of LDHs, based on hydrolysis reagents, were reported. Herein, the interlayer spacing changing of NiFe LDHs will be discussed by varying the hydrolysis reagents (HMT vs. urea) via a one-pot hydrothermal reaction method.

4.1.2. Fabrication of NiFe LDHs

The NiFe LDHs were synthesized through a one-pot hydrothermal reaction method. In this procedure, metal salt ($\text{Ni}(\text{NO}_3)_2 \cdot 6\text{H}_2\text{O}$, $\text{Co}(\text{NO}_3)_2 \cdot 6\text{H}_2\text{O}$, $\text{Fe}(\text{NO}_3)_3 \cdot 9\text{H}_2\text{O}$, or $\text{RuCl}_3 \cdot x\text{H}_2\text{O}$) and hydrolysis reagents (HMT/urea) were dissolved in DI water and processed by ultrasonic treatment to form a clear solution. Then, the aqueous solution was transferred to a Teflon-lined stainless-steel autoclave, which was sealed and maintained in the oven with a specific temperature and time (**Figure 3. 1**). The details of the fabrication recipe to prepare the NiFe LDHs were listed in **Table 2** and described as below.

Synthesis of NiFe LDHs (NiFe LDHs_ NO_3 **):** in the typical procedure, $\text{Ni}(\text{NO}_3)_2 \cdot 6\text{H}_2\text{O}$ (12 mmol), $\text{Fe}(\text{NO}_3)_3 \cdot 9\text{H}_2\text{O}$ (4 mmol), and HMT (10 mmol) were dissolved in 30 mL of DI water and aided by ultrasound to form a clear solution. Then, the aqueous solution was transferred to a 35 mL Teflon-lined stainless-steel autoclave, which was sealed and maintained at 95 °C for 24 hours. After naturally cooling down to room temperature, the NiFe LDHs were collected by centrifugation, and washed thoroughly with isopropanol 3 times. Then, the monolayer NiFe LDHs nanosheets can be obtained in DI water under a hand-shaking or ultrasonic treatment for a few seconds and the NiFe LDHs bulk was obtained after being dried in the oven at 60 °C for 2 hours.

Synthesis of NiFe LDHs_ X **($X=0.75, 0.50$, and 0.25 , where X represents the percentage of ammonium from HMT):** NiFe LDHs with different interlayer distance were synthesized by delicately varying hydrolysis reagent (the ratio of HMT to urea). In order to keep the amount of added ammonium as a constant value, the hydrolysis reagents are designed as are 7.5 mmol HMT and 5 mmol urea, 5 mmol HMT and 10 mmol urea, and 2.5 mmol HMT and 15 mmol urea for different samples, because of one urea has two $-\text{NH}_2$ groups joined by a carbonyl ($\text{C}=\text{O}$) functional group, while the HMT has four $-\text{NH}_2$ groups. Then, the NiFe LDHs_ X were synthesized with the same process as NiFe LDHs, and the prepared samples were named as NiFe LDHs_0.75, NiFe LDHs_0.50 and NiFe LDHs_0.25.

Synthesis of NiFe LDHs_0 (NiFe LDHs_CO₃²⁻): in this process, the HMT was replaced by the urea completely, and the start materials, Ni(NO₃)₂·6H₂O (12 mmol), Fe(NO₃)₃·9H₂O (4 mmol), and urea (20 mmol) were dissolved in 30 mL of DI water and processed by ultrasound to form a clear solution. Then, the aqueous solution was transferred to a 35 mL Teflon-lined stainless-steel autoclave, which was sealed and maintained at a higher temperature of 120 °C for 24 hours. The products were collected by centrifugation, washing, drying, and then labeled as NiFe LDHs_0.

Synthesis of NiFeCo, NiFeRu, NiFeCoRu, and NiFe/Au: The cobalt doped NiFe LDHs, ruthenium doped NiFe LDHs, and cobalt, ruthenium co-doped NiFe LDHs were synthesized by adding the cobalt (Co²⁺, 0.6 mM), ruthenium (Ru³⁺, 0.2 mM) and mix salt (Co²⁺, 0.6 mM and Ru³⁺, 0.2 mM) into the precursors, respectively. Following the same process as for the NiFe LDHs synthesis, we got the products named as NiFeCo, NiFeRu, and NiFeCoRu. The NiFe/Au was prepared by dropping 10 ml (0.1 mg HAuCl₄·3H₂O) into 50 mL NiFe LDHs (2 mg/mL) solution and stirring for 12 hours. Then, NiFe/Au was collected by centrifugation, washed thoroughly with isopropanol, and the bulk NiFe/Au was obtained after being dried in the oven at 60 °C.

Preparation of catalyst ink of the NiFe-based LDHs nanosheets, NiFe LDHs_0 bulk, and RuO₂: The NiFe-based LDHs monolayers were obtained directly under a hand-shaking or an ultrasonic treatment, the concentration was calibrated to 1 mg/mL. For comparison, 5 mg NiFe LDHs_0 bulk (grounded into powder with a mortar) or a RuO₂ (Sigma-Aldrich) powder was dispersed in 980 µL isopropanol containing 20 µL 5wt% of Nafion solution (Sigma-Aldrich). The mixed solution was subsequently sonicated for no less than 30 min, after which the catalyst ink was obtained (5 mg/mL). Less powder loading (1 mg/mL) for both RuO₂ and the NiFe LDHs_bulk can not cover the electrode well. On the contrary, the monolayer, which can cover the electrode very well at a small amount of loading (1 mg/mL), will fall off from the gold electrode at a larger amount of loading (5 mg/mL) because of the high current density and lots of H₂ bubbles in a short time, leading to the data can not be collected completely.

Table 2 *The recipe of NiFe-based LDHs.*

NO.	Catalyst	Recipes	Conditions	M ²⁺ /M ³⁺	Hydrolysis	NH ₃ /M
1	NiFe LDHs	12 mmol Ni(NO ₃) ₂ ·6H ₂ O), and 4 mmol Fe(NO ₃) ₃ ·9H ₂ O	95 °C 24 h	3:1	10 mmol HMT	2.5
2	NiFe LDHs _{0.75}	12 mmol Ni(NO ₃) ₂ ·6H ₂ O), and 4 mmol Fe(NO ₃) ₃ ·9H ₂ O	95 °C 12 h	3:1	7.5 mmol HMT and 5 mmol urea	2.5
3	NiFe LDHs _{0.50}	12 mmol Ni(NO ₃) ₂ ·6H ₂ O), and 4 mmol Fe(NO ₃) ₃ ·9H ₂ O	95 °C 12 h	3:1	5 mmol HMT and 10 mmol urea	2.5
4	NiFe LDHs _{0.25}	12 mmol Ni(NO ₃) ₂ ·6H ₂ O), and 4 mmol Fe(NO ₃) ₃ ·9H ₂ O	95 °C 12 h	3:1	2.5 mmol HMT and 15 mmol urea	2.5
5	NiFe LDHs ₀	12 mmol Ni(NO ₃) ₂ ·6H ₂ O), and 4 mmol Fe(NO ₃) ₃ ·9H ₂ O	120 °C 24 h	3:1	20 mmol urea	2.5
6	NiFeCo LDHs	11.4 mmol Ni(NO ₃) ₂ ·6H ₂ O), 4 mmol Fe(NO ₃) ₃ ·9H ₂ O, and 0.6 mmol Co(NO ₃) ₂ ·6H ₂ O)	95 °C 24 h	3:1	10 mmol HMT	2.5
7	NiFeRu LDHs	12 mmol Ni(NO ₃) ₂ ·6H ₂ O), 3.8 mmol Fe(NO ₃) ₃ ·9H ₂ O, and 0.2 mmol RuCl ₃ ·xH ₂ O	95 °C 24 h	3:1	10 mmol HMT	2.5
8	NiFeCoRu LDHs	11.4 mmol Ni(NO ₃) ₂ ·6H ₂ O), 3.8 mmol Fe(NO ₃) ₃ ·9H ₂ O, 0.6 mmol Co(NO ₃) ₂ ·6H ₂ O), and 0.2 mmol RuCl ₃ ·xH ₂ O	95 °C 24 h	3:1	10 mmol HMT	2.5
9	NiFe/Au	10 ml (0.1 mg HAuCl ₄ ·3H ₂ O) into 50 mL NiFe LDHs (2 mg/mL) solution and stirring for 12 hours	-	-	-	-

Notes: M²⁺/M³⁺ represents the ratio of divalent (Ni²⁺) to trivalent ((Fe³⁺)) metal ions. M represents the sum of metal ions (Ni²⁺ and Fe³⁺).

4.1.3. Schematic, structure and exfoliation of the NiFe LDHs monolayer

As shown of the schematic diagram in **Figure 4. 1a**, the NiFe LDHs bulk was obtained via a one-pot hydrothermal method, and the monolayers were directly obtained in DI water by shaking or ultrasonic treatment for a few seconds after washing with isopropanol. The structure of NiFe LDHs was first studied via XRD. The XRD pattern of the NiFe LDHs, as shown in **Figure 4. 1b**, is consistent with the reference NiFe LDH (JCPDS 40-0215),^[172] but with slightly larger interlayer spacing. Detailed analysis of (003) and (006) peaks shows that the corresponding d spacings are 0.82 and 0.41 nm, respectively, which are larger than the reference values 0.78 and 0.39 nm.^[172] The expanding of the d spacing indicates the formation of a new 2D NiFe LDHs structure with enlarged interlayer spacing compared to the standard NiFe LDH structure. The enlarged basal spacing facilitates exfoliation of bulk NiFe LDHs into nanosheets in DI water (**Figure 4. 1a, b**). The Tyndall effect observed upon irradiation of the solutions with a laser beam confirms the colloidal nature of the solution (**Figure 4. 1c**).

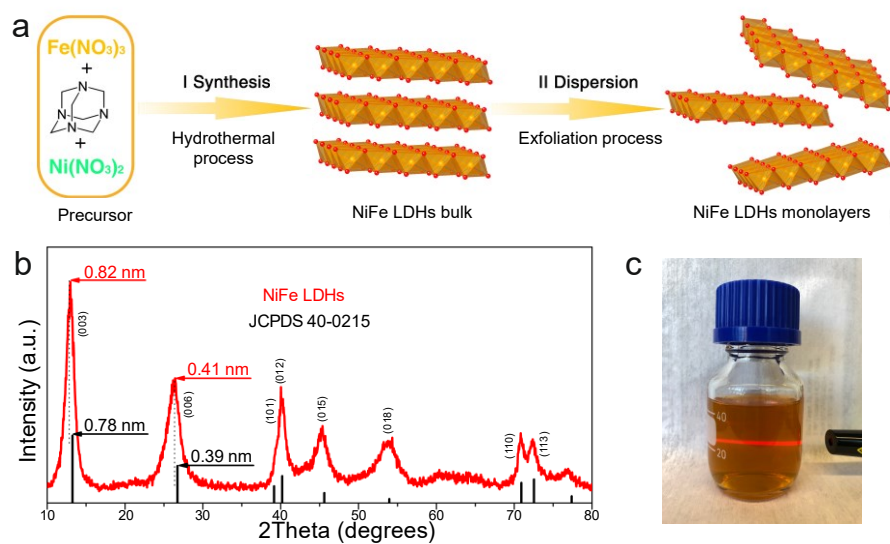


Figure 4. 1 (a) Schematic of the preparation process of NiFe LDHs bulk and monolayers. (b) XRD pattern of NiFe LDHs. The standard pattern of the pristine NiFe LDHs (JCPDS 40-0215). (c) The photographs of NiFe LDHs colloidal solution under laser irradiation.

Table 3. Comparison of this strategy as well as the reported LDHs exfoliated methods: exfoliated methods, equipment, time factors, and prices.

LDHs	Exfoliated methods	Equipment	Time	Prices	Ref.
NiFe LDHs	Directly exfoliation	-	< 10 s	Low	This work
Co(OH) ₂ Nanosheets	Liquid phase exfoliation	High-powder ultrasonication	> 6 h	Median	[40]
LDHs	Ion exchange	-	Few days	Median	[19, 33-39]
CoFe LDHs	Water-plasma	Water-plasma with high voltage generator	5 min	High	[43]
CoNi LDHs	Ar plasma	High voltage generator	10 min	High	[44]
CoFe LDHs	Acid-etched	1 M HNO ₃	30 min	Median	[41]
Bulk LDHs	Strong alkali etching	5 M NaOH	5-120 min	Median	[42]

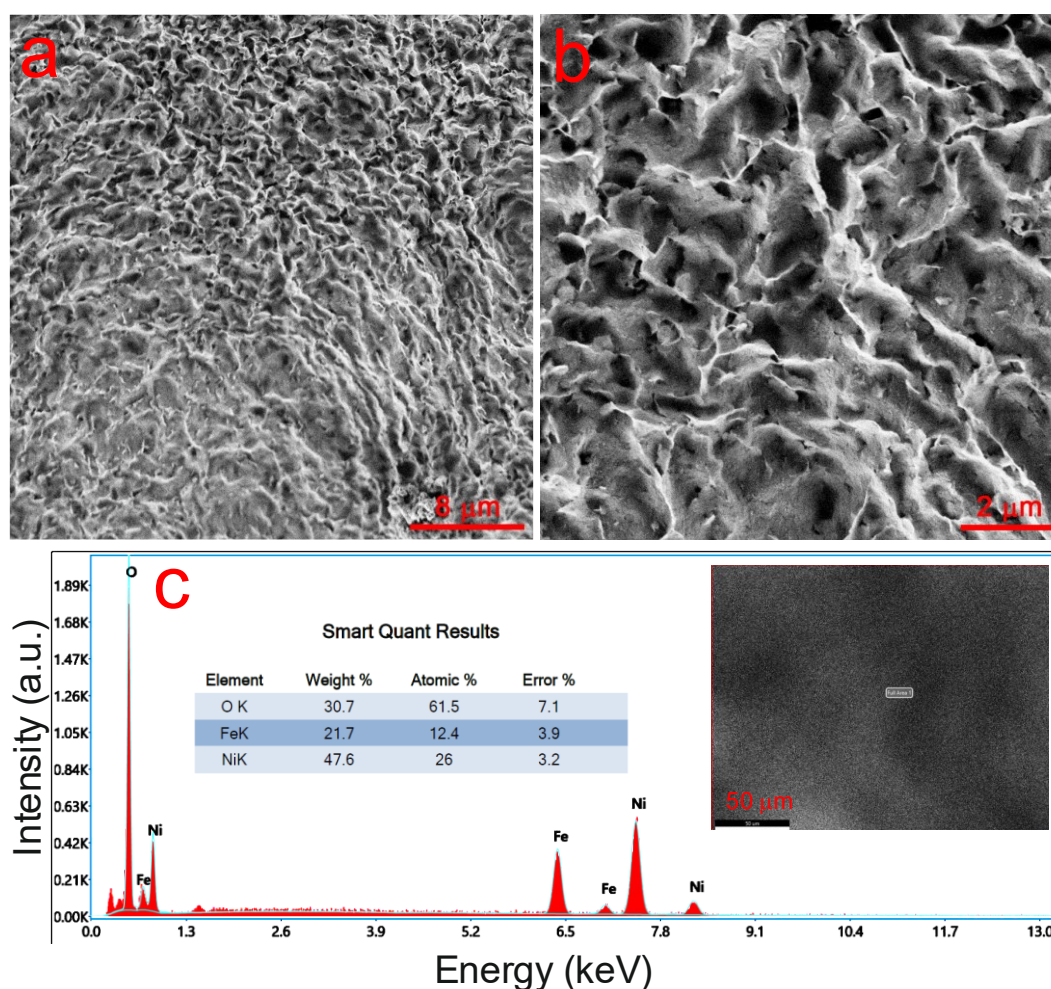


Figure 4. 2 SEM images of NiFe LDHs: (a) low magnification and (b) high magnification. (c) EDS pattern of NiFe LDHs over the full area. The inset in figure (c) shows one selected area of NiFe LDHs and atomic ratios of nickel (Ni), iron (Fe), and oxygen (O) in NiFe LDHs calculated from five different areas.

Compared with the other reported exfoliated methods, as listed in **Table 3**, the NiFe LDHs prepared through this strategy can be exfoliated into nanosheets in a simple, efficient, and low-cost way.

The morphology of the NiFe LDHs was then observed by SEM. As shown in **Figure 4. 2**, the as-prepared NiFe LDHs display a nanosheet morphology with random shape. The element ratios of Ni, Fe, and O which detected by EDS mapping measurements, are 26.5, 12.2, and 61.3 at percentage, respectively (**Figure 4. 2c**).

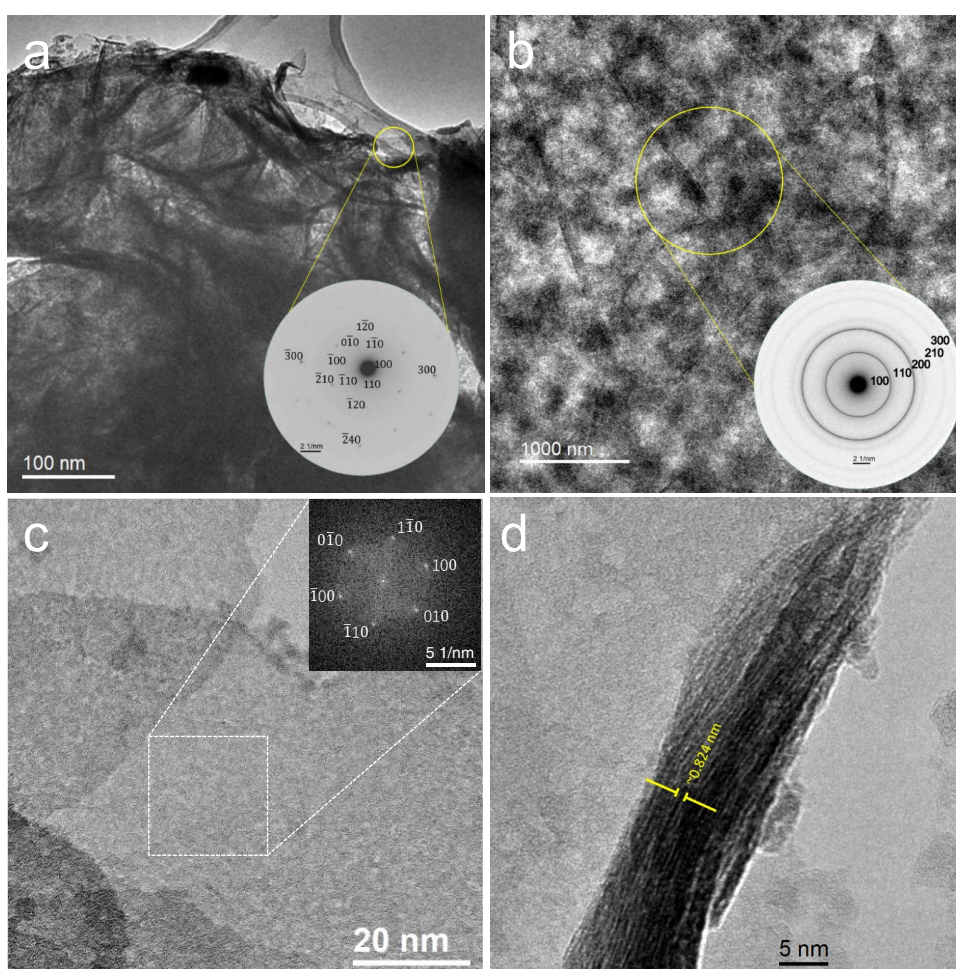


Figure 4. 3 TEM images of NiFe LDHs. (a) TEM image of NiFe LDHs bulk and corresponding SAED pattern (inset). (b) TEM image of exfoliated NiFe LDHs nanosheets and corresponding SAED pattern (inset). (c) HRTEM images of NiFe LDHs monolayers and the corresponding diffractogram pattern are marked in the red square area (inset). (d) HRTEM image of the cross-section of NiFe LDHs.

TEM characterization was employed to investigate the detailed morphology and microstructure features of the NiFe LDHs bulk, the exfoliated NiFe LDHs nanosheets, and the cross-section of NiFe LDHs (**Figure 4. 3**). **Figure 4. 3a** shows the TEM results of NiFe LDHs bulk obtained from dry crushed powder. The corresponding selected area diffraction (SAED) pattern (**Figure 4. 3a**, inset) confirms the high crystallinity of the NiFe LDHs, which is consistent with the XRD pattern results (**Figure 4. 1b**). In contrast to the NiFe LDHs bulk, the SAED and TEM images of exfoliated NiFe LDHs nanosheets indicates they are mostly oriented in the [001]-zone axis (**Figure 4. 3b**) and that these nanoflakes are very thin as can be seen from **Figure 4. 3c**. The SAED pattern of exfoliated NiFe LDHs nanosheets reveals two diffraction rings (**Figure 4. 3b**, inset), corresponding to NiFe LDHs (100) and (110) planes and suggesting the formation of a polycrystalline structure after the block exfoliation.^[39, 172] Furthermore, high-resolution TEM (HRTEM) was also applied to investigate the structure of individual NiFe LDHs monolayers (**Figure 4. 3c**). The exfoliated NiFe LDHs monolayers display a faint contrast, clearly revealing their sheet-like nanostructure and their very thin nature. The corresponding diffractogram pattern (**Figure 4. 3c**, inset) exhibits a typical six-fold symmetry, in accordance with the hexagonal structure of NiFe LDH indicating that the single crystalline nature is retained after the block exfoliation. In addition, the HRTEM image demonstrates a larger interlayer distance, 0.82 nm, matching well with the XRD pattern (**Figure 4. 1b**), than the reference NiFe LDH (JCPDS 40-0215).

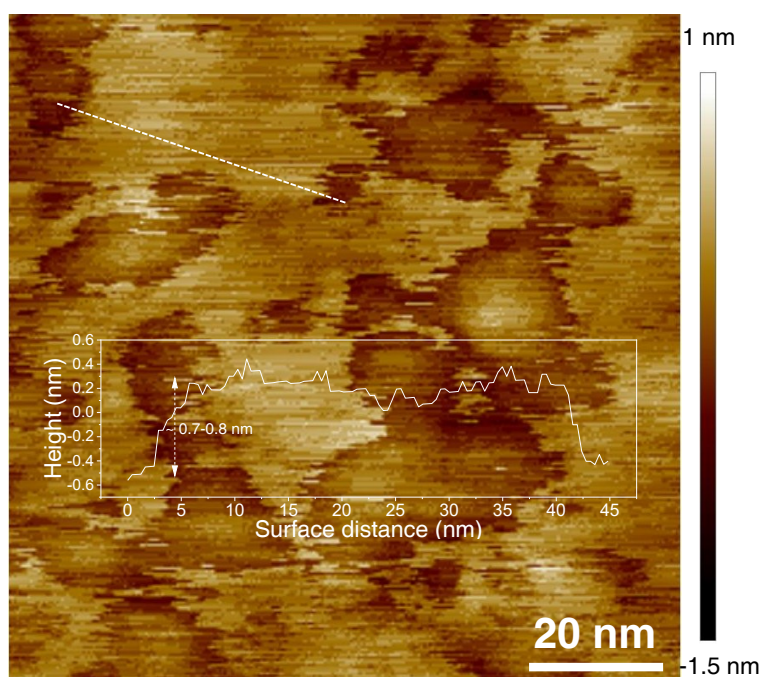


Figure 4. 4 AFM images and the corresponding height profiles of the NiFe LDHs.

The exfoliated monolayer NiFe LDHs nanosheets were directly verified by AFM. **Figure 4. 4** displays ultra-thin characteristics of the exfoliated monolayer NiFe LDHs nanosheets, lower than 1 nm.^[19, 227] The AFM topology revealed that the average thickness of the NiFe LDHs nanosheets is about 0.7-0.8 nm (**Figure 4. 4**), thus suggesting that the initial bulk NiFe LDHs were efficiently exfoliated into NiFe LDH monolayer nanosheets. In short, monolayer NiFe LDHs was obtained in a facile way by synthesing a new NiFe LDHs bulk with enlarged interspacing by using HMT as a hydrolysis reagent.

4.1.4. Structure evolution of NiFe LDHs

In order to further investigate this unique phenomenon, more NiFe LDHs samples are prepared with different hydrolysis reagents, such as HMT and urea. The as-prepared samples are named as NiFe LDHs_X for convenience, where X denotes the percentage of ammonium from HMT (details in Chapter 4.1.2). For example, the NiFe LDHs_1 (NiFe LDHs) represents the NiFe LDHs prepared by using HMT as the hydrolysis reagent, while the NiFe LDHs_0 stand for the products by using urea. As shown in **Figure 4. 5**, XRD was carried out on various samples to investigate the structural evolution. It can be clearly found from the powder XRD patterns (**Figure 4. 5a**), the structure of these NiFe LDHs was confirmed and no impurities phases were detected. The NiFe LDHs_0, prepared by using urea, show the same d spacings as the reference NiFe LDH (JCPDS 40-0215). With the increasing ratio of HMT to urea, the position of (003) and (006) diffraction peaks show a shift towards a smaller angle, indicating an increase in the d spacing along the c -axis for the obtained NiFe LDHs (**Figure 4. 5b**).

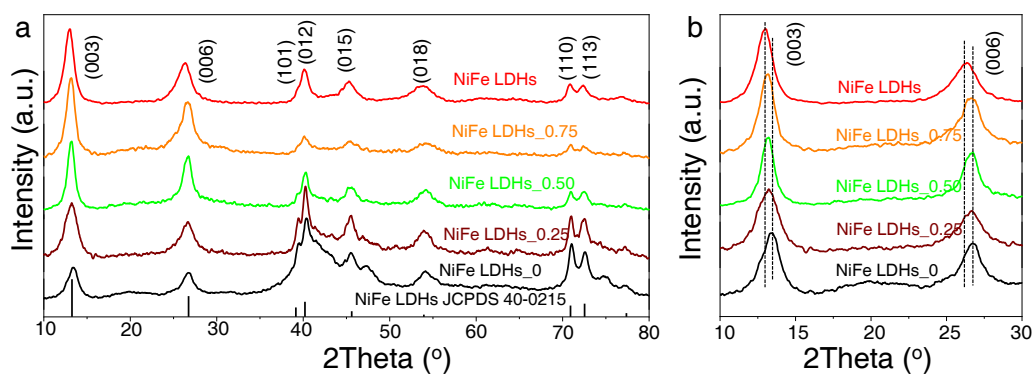


Figure 4. 5 (a) XRD patterns of LDHs obtained at various hydrolysis reagent (the ratio of HMT to urea). (b) (003) and (006) peaks shift of XRD patterns of the obtained as-prepared LDH samples varying hydrolysis reagent between urea and HMT.

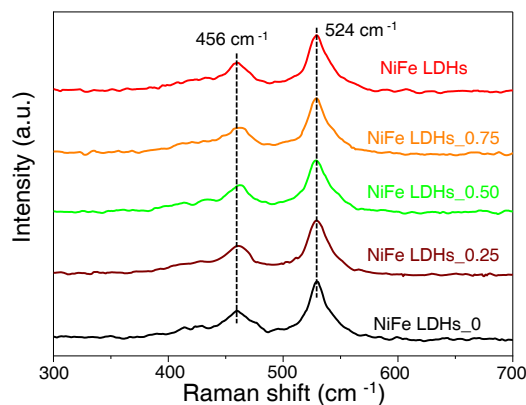


Figure 4. 6 Raman of LDHs obtained at various hydrolysis reagents (the ratio of HMT to urea).

Raman and FT-IR spectroscopy were further performed to acquire information about the chemical identities and structure evolution of the as-prepared NiFe LDHs when varying with the hydrolysis reagents. As shown in **Figure 4. 6**, the pair of bands that emerged at around 456 and 524 cm^{-1} were observed in all NiFe LDHs samples. There is no big difference among all the samples. Compared to A_{1g} modes of Ni-OH (474 cm^{-1}) and of Ni-O (554 cm^{-1}) in pure $\text{Ni}(\text{OH})_2$,^[143, 239] all NiFe LDHs show higher wavenumbers, resulting when the Fe phase was introduced in the $\text{Ni}(\text{OH})_2$ phase.^[234]

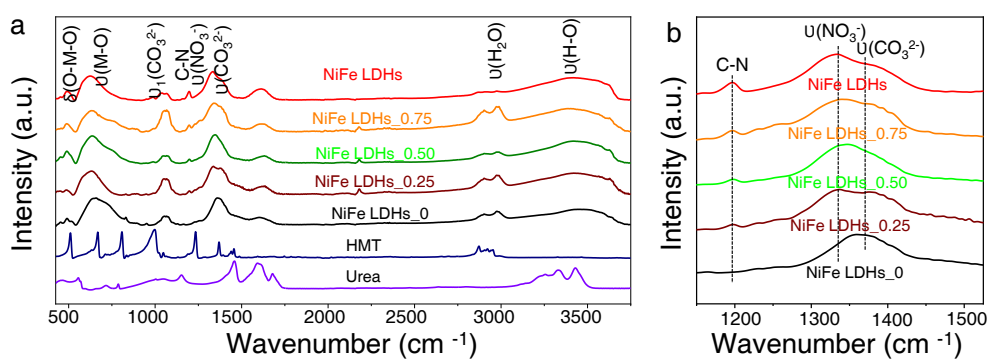


Figure 4. 7 (a) FT-IR spectra of the LDHs. Prepared from pure HMT to pure urea. (b) Region characteristic for NO_3^- and CO_3^{2-} in the NiFe LDHs.

The FT-IR spectra of the NiFe LDHs powder in the region between 400 and 4000 cm^{-1} are illustrated in **Figure 4. 7**. As illustrated in **Figure 4. 7a**, LDHs show the stretching vibrations of intercalated carbonates in the NiFe LDH at 480 cm^{-1} , 610 cm^{-1} , 1055 cm^{-1} , 2950 cm^{-1} , and 3450 cm^{-1} for $\delta(\text{O-M-O})$, $\nu(\text{M-O})$, $\nu_1(\text{CO}_3^{2-})$, $\nu(\text{H}_2\text{O})$ and $\nu(\text{H-O})$, respectively.^[174, 240] Interestingly, as seen via zoom in **Figure 4. 7b**, the intercalated carbonates (CO_3^{2-}) are still in the LDHs, and are observed at 1380 cm^{-1} .^[174] Here are two peaks that appeared at 1200 and 1300 cm^{-1} for CN vibration and (NO_3^-) vibration while varying the various hydrolysis reagent.^[174]

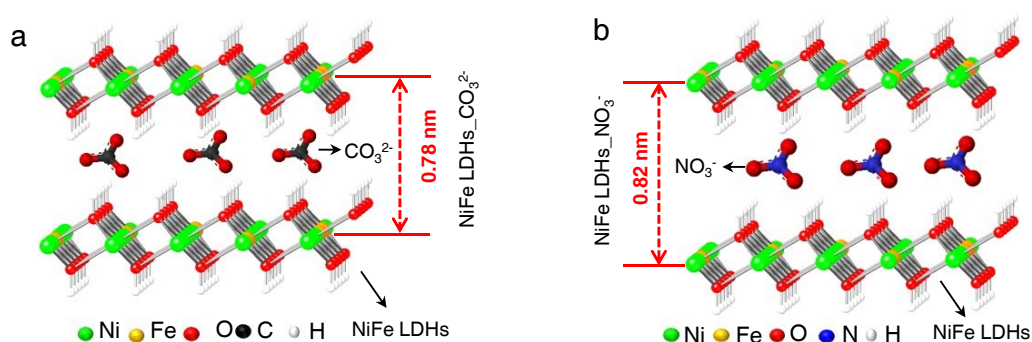


Figure 4. 8 Schematic diagram of NiFe LDHs samples: (a) NiFe LDHs_0 (NiFe LDHs_ CO_3^{2-}) prepared by using urea as hydrolysis reagent) and (b) NiFe LDHs (NiFe LDHs_ NO_3^-) prepared by using HMT as hydrolysis reagent).

Figure 4. 8 displays the schematic diagram of NiFe LDHs_0 (NiFe LDHs_ CO_3^{2-}) and NiFe LDHs (NiFe LDHs_ NO_3^-). The NiFe LDHs_0 (**Figure 4. 8a**) shows a smaller interlayer spacing than the NiFe LDHs (**Figure 4. 8b**). Compared to the urea as a hydrolysis reagent only, there are two functions for the HMT during the hydrothermal process. The HMT can both worked as hydrolysis reagent and inducer during the reaction process, which will intercalate CN compound or NO_3^- into the LDHs interlayer, leading to form a loosely stacked and swollen phase, which can be easily dispersed in water.

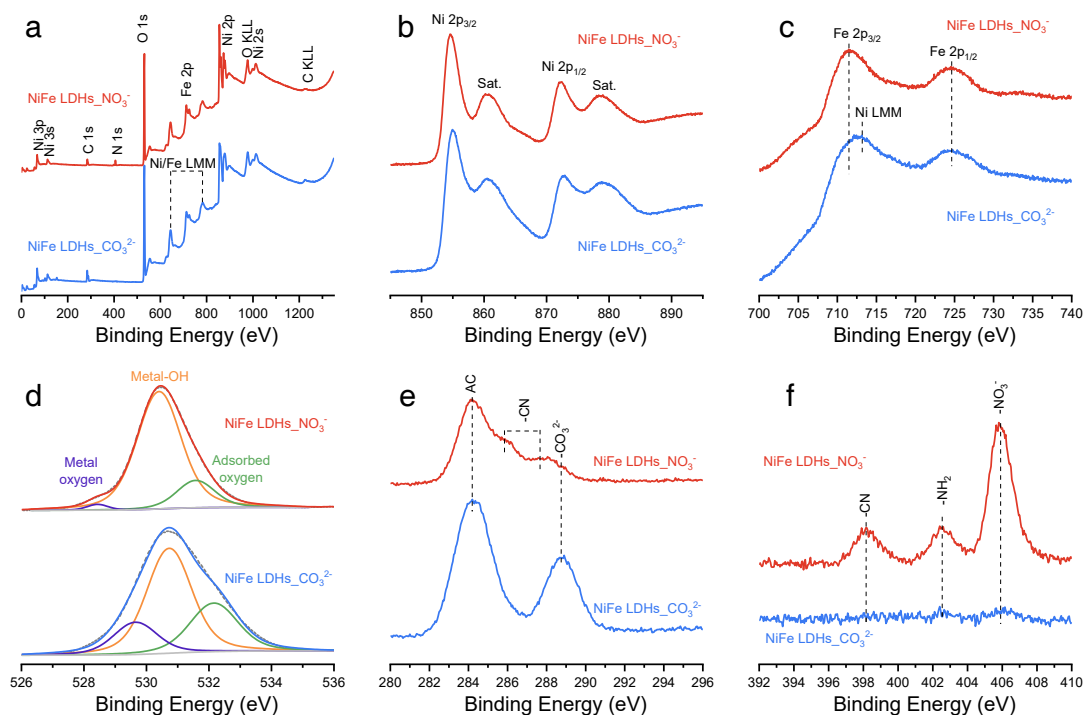


Figure 4. 9 XPS spectra comparison of NiFe LDHs (NiFe LDHs_ NO_3^-) and NiFe LDHs_0 (NiFe LDHs_ CO_3^{2-}). (a) Survey, (b) Ni 2p, (c) Fe 3p, (d) O 1s, (e) C 1s and (f) N 1s. The KLL and LMM structure result from the excitation of Auger electron emission.

XPS was used to further investigate the surface chemical composition and valence states of NiFe LDHs (NiFe LDHs_ NO_3^-) and NiFe LDHs_0 (NiFe LDHs_ CO_3^{2-}) (**Figure 4. 9**). The survey XPS spectra of the two samples revealed the presence of Ni, Fe, O, and C elements. Notably, a N 1s signal appeared only in the NiFe LDHs_ NO_3^- sample (**Figure 4. 9a**). The Ni 2p spectra (**Figure 4. 9b**) consist of two doublets and two shake-up satellites, which are associated with the Ni^{2+} and Ni^{3+} species in Ni-O, $\text{Ni}(\text{OH})_2$, and NiOOH for both the NiFe LDHs_ NO_3^- and the NiFe LDHs_ CO_3^{2-} .^[241-243] Similarly, the Fe 2p spectra (**Figure 4. 9c**) can be fitted by two doublets that correspond to the Fe^{2+} and Fe^{3+} species in FeOOH ^[244, 245] for both samples. And the broad peak detected at around 712.9 eV can be attributed to Ni LMM Auger peaks.^[246] O1s spectra for both samples consist of three different species. The first, at low binding energies, is associated with the oxygen-metal (Ni-O and Fe-O) bonds, while the second at ~531.1 eV originates from oxygen from the hydroxyl groups.^[247, 248] The O species at 532 eV is typical for adsorbed O-O bonds in samples (**Figure 4. 9d**).^[249] The largest differences between the

two samples are observed in the C 1s and N 1s spectra. While both samples exhibit adventitious carbon (AC, centered at 284.8 eV), the signal at higher binding energies varies greatly (**Figure 4. 9e**). The NiFe LDHs_CO₃²⁻ sample shows a strong peak at a binding energy of 288.6 eV which corresponds to carbonate (CO₃²⁻),^[250] while the NiFe LDHs_NO₃⁻ sample exhibits signal at binding energies in the range from 285.7 to 287.8 eV, which are related to CN bonds^[251, 252] in **Figure 4. 9e**. Furthermore, compared with the signal in NiFe LDHs_CO₃²⁻, the N 1s XPS spectrum displays three clear peaks at 398.1, 402.5, and 405.8 eV attributed to CN bonds, -NH₂ group, and NO₃⁻, respectively^[251-253] in **Figure 4. 9f**.

Taken together, the XRD, FT-IR, and XPS results lead to the conclusion that hydrolysis reagents (urea, HMT, etc.) have a significant effect on the interlayer spacing changing of LDHs during synthesizing. Compared with the urea as the hydrolysis reagent only, there are two functions for HMT during the hydrothermal process: the first one is as the hydrolysis reagent, while the second is an inducer, which leads to CN compound and NO₃⁻ intercalated into the LDHs interlayer space. As shown in the schematic diagram, NiFe LDHs_CO₃²⁻ has a smaller interlayer spacing than NiFe LDHs_NO₃⁻ (**Figure 4. 8**). Finally, a loosely stacked and swollen phase of NiFe LDHs_NO₃⁻ with an enlarged basal spacing was obtained.

4.1.5. Universality investigation of the synthesis strategy

The universality of the synthesis strategy was investigated by preparing other NiFe-based multi-metal LDHs including cobalt doped NiFe LDHs (NiFeCo), ruthenium doped NiFe LDHs (NiFeRu), cobalt and ruthenium co-doped NiFe LDHs (NiFeCoRu) and gold modified NiFe LDHs (NiFe/Au). The recipes and experimental details were listed in section 4.1.2. The structure, morphology, and elemental analysis of the doped and modified NiFe LDHs were characterized by XRD, SEM, and EDS. Moreover, the exfoliated multi-metal NiFe LDHs monolayer nanosheets were checked by AFM measurement.

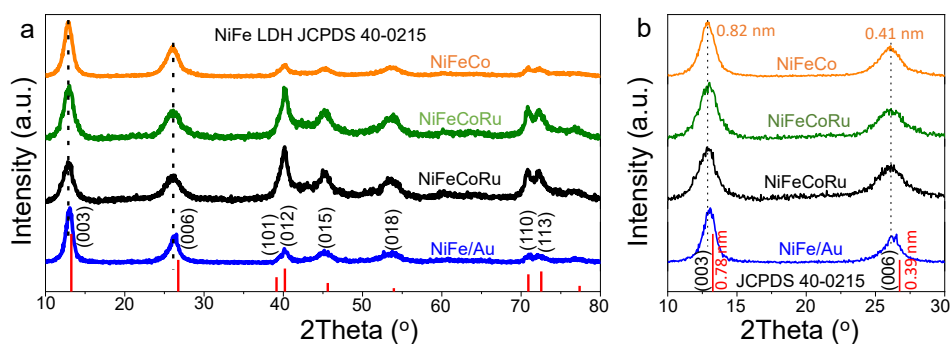


Figure 4. 10. (a) XRD patterns and (b) the zoom-in of the (003) and (006) peaks of NiFe-based multi-metal layered double hydroxides: NiFeCo, NiFeRu, NiFeCoRu, and NiFe/Au.

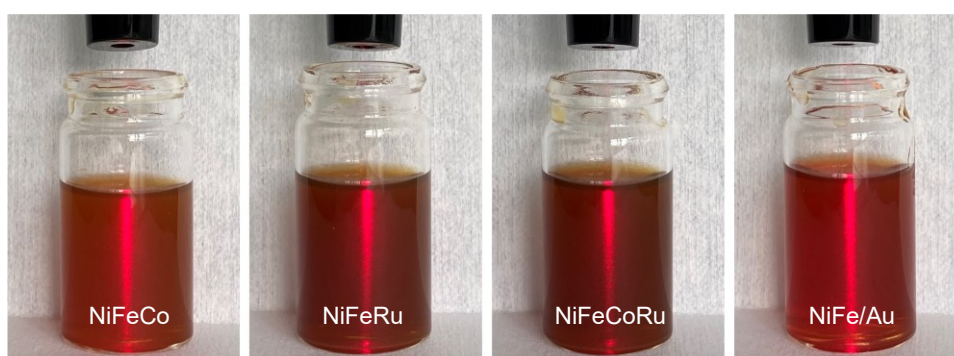


Figure 4. 11. Optical images of NiFe-based multi-metal LDHs nanosheets. Tyndall effect was visible when irradiated with a laser beam.

All of the samples possess a typical NiFe LDHs structure (JCPDS 40-0215) with an enlarged interlayer spacing (**Figure 4. 10**). Compared to the reference NiFe LDHs,

NiFeRu and NiFeCoRu show stronger relative intensity of edges peaks, such as peaks (012) and (110) in **Figure 4. 10a**. As reported, the edges of LDHs own higher OER performance than the natural (001) facet.^[32, 129, 154] **Figure 4. 11** displays optical images of NiFe-based multi-metal LDHs nanosheets exfoliated in water under an ultrasonic treatment or shaking for a few seconds. The phenomenon of the Tyndall effect was observed when irradiated with a laser beam which further confirmed the easy exfoliation property of the NiFe-based multi-metal LDHs nanosheets.

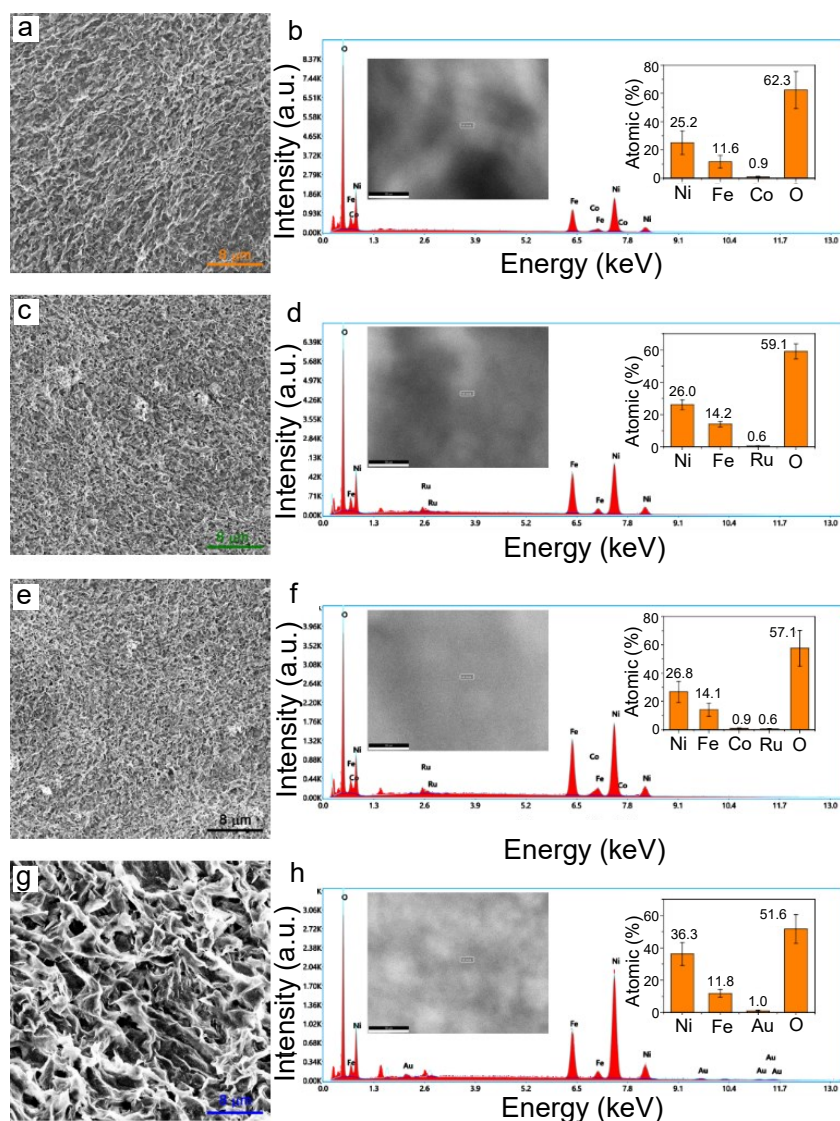


Figure 4. 12 SEM and EDS patterns of NiFe-base LDHs: NiFeCo (a and b), NiFeRu (c and d), NiFeCoRu (e and f), and NiFe/Au (g and h). The inset in figures (b, d, f, and h) shows one selected area of NiFe-based LDHs (Scale bar 50 μm); atomic composition in each sample was calculated from five different areas.

The morphology and corresponding elements analysis of the doped and modified NiFe LDHs samples were carried out by SEM and EDS in **Figure 4. 12**. All of the samples show a sheet-like morphology in SEM images and the corresponding EDS confirmed the success of doping and modification of the NiFe LDHs process.

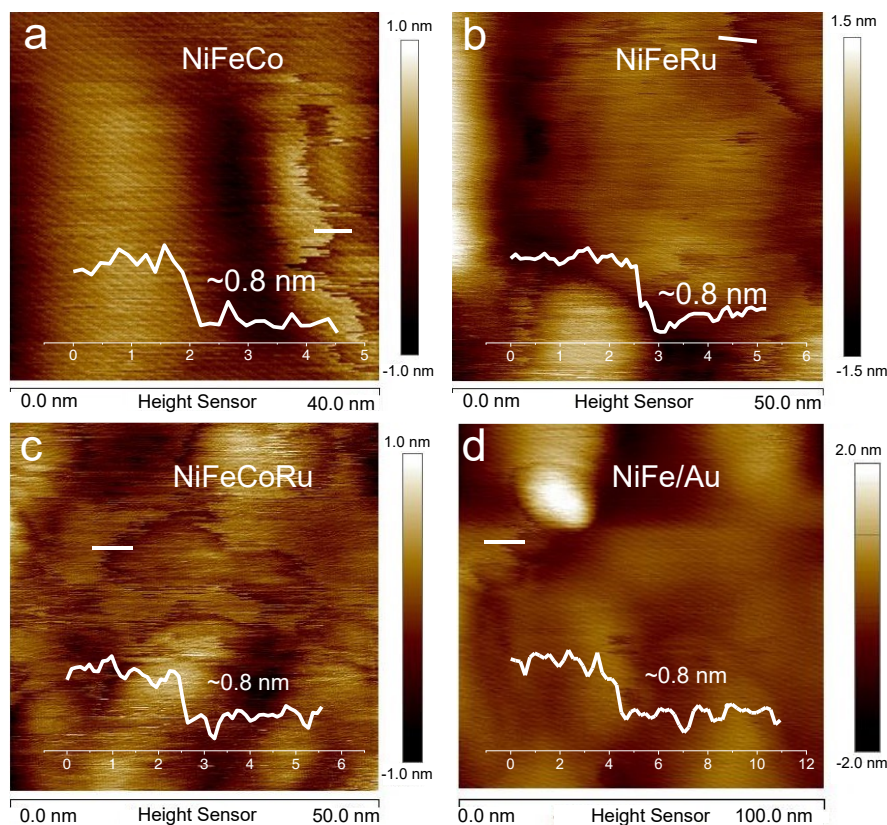


Figure 4. 13 Tapping-mode AFM image and the corresponding height profiles of exfoliated monolayer NiFe-based multi-metal LDHs (a) NiFeCo, (b) NiFeRu, (c) NiFeCoRu and (d) NiFe/Au LDH nanosheets. It is marked with white line.

The AFM topology reveals that all the NiFeCo, NiFeRu, NiFeCoRu, and NiFe/Au LDHs nanosheets are monolayers (**Figure 4. 13**), which is consistent with the NiFe LDHs monolayers (**Figure 4. 4**) and a reported theoretical value,^[227] thus suggesting that the obtained NiFeCo, NiFeRu, NiFeCoRu and NiFe/Au LDH bulk were efficiently exfoliated into LDHs monolayer nanosheets. It is corroborated that the NiFe-based multi-metal LDHs monolayer was successfully obtained after the structure, morphology, and element analysis by XRD, SEM, EDS, and AFM, confirming the universality of the synthesis strategy.

4.1.6. OER performance of NiFe LDHs monolayers

Based on the above investigations, a strategy to prepare NiFe-based LDHs with large interlayer spacing is presented. The NiFe LDHs can be directly exfoliated into monolayer nanosheets in water in a short time via a simple way. The OER performance of NiFe LDHs monolayers is investigated to study the underlying application for energy conversion. OER performance of the NiFe LDHs monolayers was first measured at drop-coated thin films on a Cr/Au electrode in 1 M KOH aqueous electrolyte. The schematic for the Cr/Au electrode based on lithography and e-beam deposition is depicted in **Figure 4. 14** and the fabrication details are listed in Chapters 3.1.4 and 3.1.5.

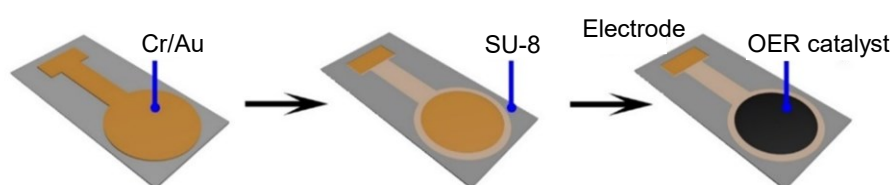


Figure 4. 14 Schematic illustrations of the fabrication process of work electrode based on lithography and e-beam deposition.

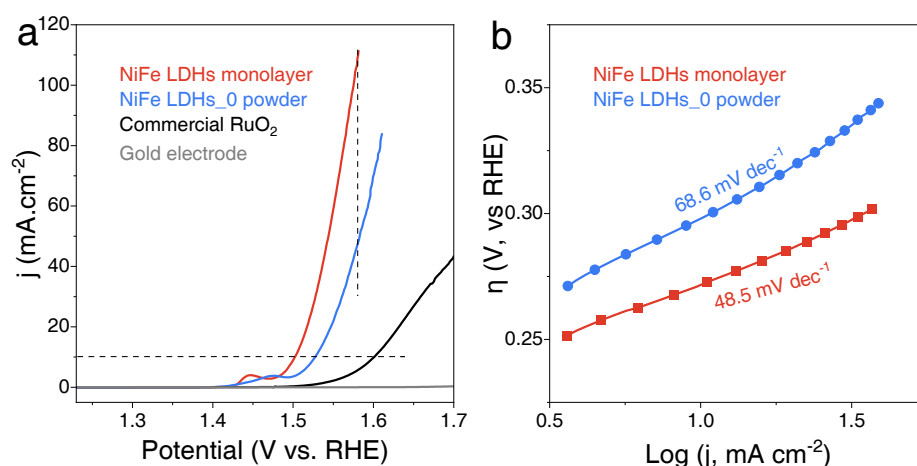


Figure 4. 15 OER performance. (a) Polarization curves of the NiFe LDHs monolayers, NiFe LDHs_0 powder, commercial RuO_2 , and gold electrode, sweep rate: 5 mV s^{-1} . (b) The corresponding Tafel slopes of the NiFe LDHs monolayers and NiFe LDHs_0 powders.

Figure 4. 15a shows the iR-compensated LSV curve of the NiFe LDHs monolayer nanosheets, the NiFe LDHs_0 powder, and the commercial RuO₂ catalyst as well as the gold electrode. It is noted that the bare gold electrode shows poor activity for electrocatalytic oxygen evolution. The NiFe LDHs monolayers and NiFe LDHs_0 powder show an obvious oxidation peak located at 1.42 V versus the RHE, which corresponds to the oxidation reaction of Ni²⁺ to Ni³⁺.^[234, 254] The NiFe LDHs monolayers required an overpotential of only 270 mV at 10 mA cm⁻², which is 40 mV lower than that of the NiFe LDHs_0 powder counterpart tested under the same conditions, respectively. For comparison, RuO₂ reaches 10 mA·cm⁻² at an overpotential of 350 mV, agree well with the reported data.^[255] Correspondingly, the NiFe LDHs monolayers exhibit improved OER catalytic activity with a lower Tafel slope of 48.5 mV dec⁻¹, indicating a facile electron transfer for water oxidation (**Figure 4. 15b**) compared to the NiFe LDHs_0 powder (68.6 mV dec⁻¹). Meanwhile, the NiFe LDHs monolayers exhibit a remarkably higher current density than the NiFe LDHs_0 powder sample when a voltage beyond the oxidation peak was applied, suggesting a more efficient OER activity of the exfoliated NiFe LDHs monolayers.

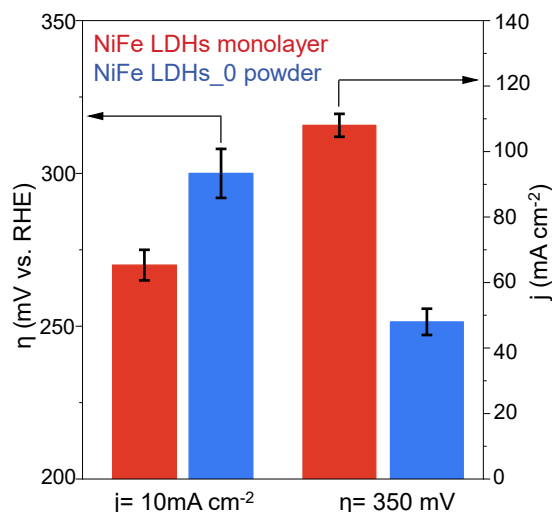


Figure 4. 16 Activity comparison of NiFe LDHs monolayer, NiFe LDHs_0 powder. The overpotential at current density of $j = 10 \text{ mA} \cdot \text{cm}^{-2}$. The current was normalized to the areal activity at an overpotential of $\eta = 350 \text{ mV}$. Error bars represent the standard deviation of six measurements.

Figure 4. 16 further summarizes the relationship of overpotential and areal current densities of the NiFe LDHs monolayers and the NiFe LDHs_0 powder at a current density of $j = 10 \text{ mA}\cdot\text{cm}^{-2}$ and $\eta = 350 \text{ mV}$, respectively. The NiFe LDHs monolayers show a small overpotential than the NiFe LDHs_0 powder. Furthermore, the current densities of NiFe LDHs monolayers (108 mA cm^{-2}) are about 2 times as large as that of NiFe LDHs_0 powder (48 mA cm^{-2}) although the mass loading for the monolayer materials (6 micrograms) was five times less than the bulk powder (the details are listed in Chapter 3.3.1).

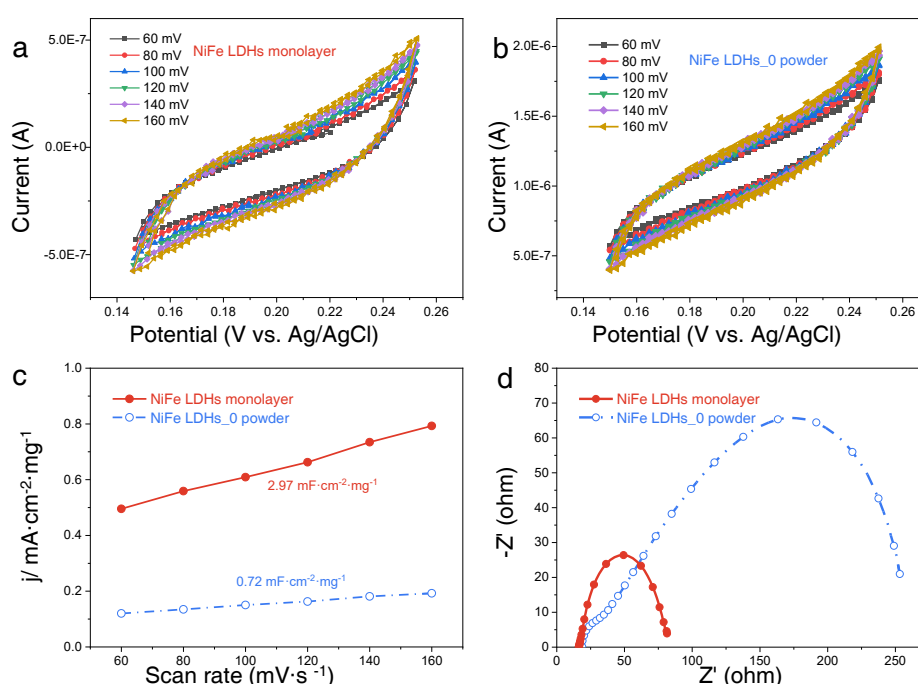


Figure 4. 17 Cyclic voltammetry (CV) curves of (a) NiFe LDHs monolayers and (b) NiFe LDHs_0 powder, scanned in the non-faradaic potential window at variable scan rates from 60 to 160 mV/s. The test potential range is 1.15-1.25 V vs RHE. The corresponding current density at 1.2 V vs RHE is used for calculating the C_{dl} value. (c) The calculated C_{dl} of NiFe LDHs monolayers and NiFe LDHs_0 powder catalysts. (d) Nyquist plots of NiFe LDHs monolayers and NiFe LDHs_0 powder at applied potentials 1.5V vs. RHE (overpotential at 270 mV).

The electrochemical double layer capacitance (C_{dl}), which is in proportion to the electrochemical active surface area (ECSA), was calculated by the cyclic voltammetry (CV) curves in the range 1.15-1.25 vs RHE without redox processes (**Figure 4. 17a** and

b). As shown in **Figure 4. 17c**, the NiFe LDHs monolayers have larger C_{dl} ($2.97 \text{ mF cm}^{-2} \text{ mg}^{-1}$) than the NiFe LDHs_0 powder ($0.72 \text{ mF cm}^{-2} \text{ mg}^{-1}$), demonstrating that the intrinsic active site activity of NiFe LDHs monolayers was much higher than that of the NiFe LDHs_0 powder. Furthermore, EIS analysis was performed to study the interfacial properties of the electrocatalysts electrodes at the overpotential of 270 mV in 1.0 M KOH solution with the frequency range from 100 kHz to 0.1 Hz. The Nyquist plots and equivalent electrical circuit of NiFe LDHs monolayers and NiFe LDHs_0 powder are recorded at an overpotential in **Figure 4. 17d**, which exhibits a smaller charge-transfer resistances (R_{ct} , 26Ω) than the NiFe LDHs_0 powder (66Ω), which indicates a much faster charge-transfer rate and higher charge-transfer kinetics for the NiFe LDHs monolayers.

Furthermore, the catalyst-electrode interactions were studied by loading the NiFe LDHs monolayers or RuO_2 catalyst on a glassy carbon disk electrode (GCE) (**Figure 4. 18a**). As shown in **Figure 4. 18b-c**, the iR-compensated LSV was carried out with a rotating disk electrode (RDE) at a rotation speed of 1600 rpm, which showed a higher overpotential than the value on the gold electrode, and is consistent with the previous reports that the gold/LDHs films show better adhesion, lower resistivity, and higher electrochemically activity, attributing to electronic effects between the LDHs host and gold.^[161, 256]

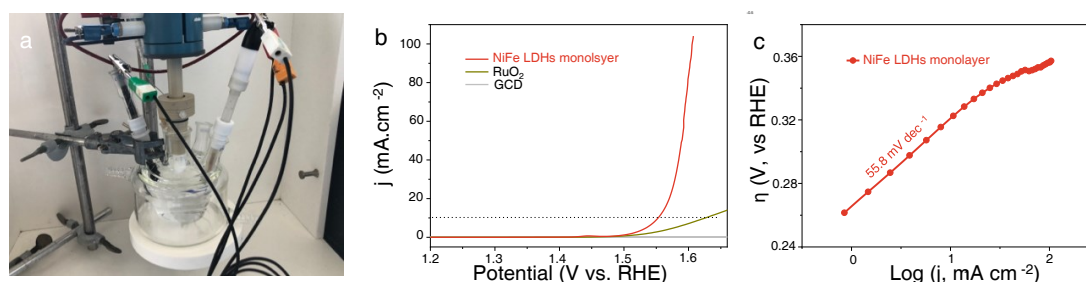


Figure 4. 18 (a) Setup of a rotating disk electrode (RDE). (b) Polarization curves of the NiFe LDHs monolayers and commercial RuO_2 and glassy carbon disk electrode (GCE, 5 mm in diameter), sweep rate: 5 mV s^{-1} at the rotation rate of 1600 rpm. (c) The corresponding Tafel slopes of the NiFe LDHs monolayers on GCE.

4.1.7. OER performance of multi-metal NiFe-based LDHs monolayer

The OER performance of multi-metal NiFe-based LDHs monolayers were also measured on the Cr/Au electrode in 1 M KOH aqueous electrolyte. **Figure 4. 19** exhibits representative iR-corrected OER LSV curves for all multi-metal NiFe-based LDHs monolayers electrocatalysts at a scan rate of 5 mV s^{-1} . The NiFe/Au required an overpotential of only 240 mV which is much lower than in the NiFe LDHs (**Figure 4. 15a**) and other multi-metal LDHs (**Figure 4. 19**). This substantial improvement can be ascribed to the charge redistribution of active Fe as well as its surrounding atoms caused by the gold.^[159, 161, 256] Both NiFeRu and NiFeCoRu exhibit improved OER activities compare to the NiFeCo and NiFe LDHs because of the ruthenium leading to more high index surfaces (edges), which have higher OER activity than natural (001) facet, confirmed by theoretical calculations and experimental results.^[32, 129, 154] In addition, the corresponding Tafel slope of NiFe-based multi-metal LDHs nanosheets shows a similar value as the exfoliated NiFe LDHs, ranging from 43 - 49 mV dec^{-1} , and is smaller than the value of NiFe LDHs_0 powder (**Figure 4. 15b**). The OER activity comparison of NiFe LDHs and multi-metal NiFe-based LDHs is summarized in **Figure 4. 19b** that the NiFeRu, NiFeCoRu, and NiFe/Au show better OER performance than the NiFe LDHs and NiFeCo.

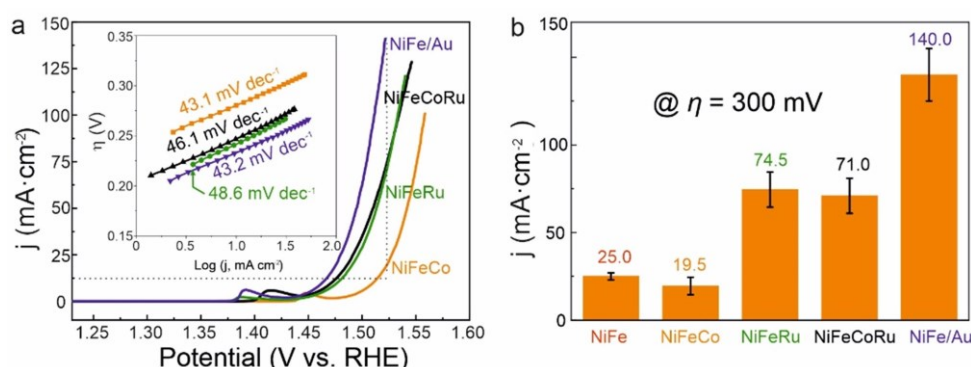


Figure 4. 19 (a) Polarization curves and the corresponding Tafel slopes (inset) of the NiFeCo, NiFe Ru, NiFeCoRu, and NiFe/Au, sweep rate: 5 mV s^{-1} . (b) Activity comparison of NiFe LDHs and multi-metal NiFe-based LDHs monolayers. The current density normalized at $\eta = 300 \text{ mV}$.

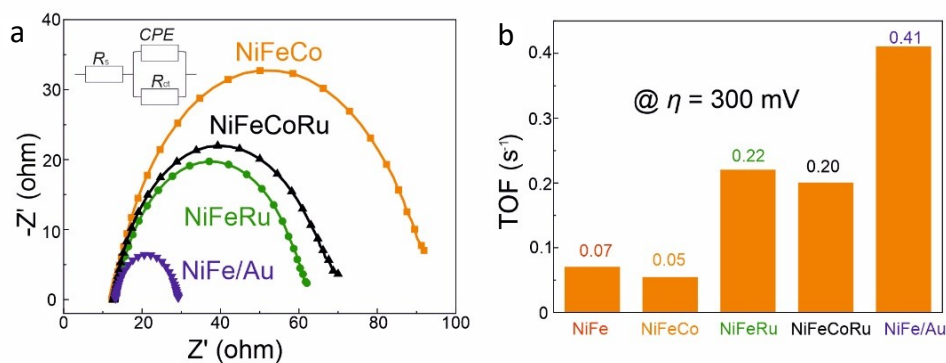


Figure 4. 20 (a) Nyquist plots of NiFe-base LDHs: NiFeCo, NiFeRu, NiFeCoRu, and NiFe/Au at applied potentials 1.5V vs. RHE (overpotential at 270 mV). (b) The calculated TOFs of NiFe LDHs monolayers, NiFeCo, NiFeRu, NiFeCoRu, and NiFe/Au at $\eta = 300$ mV.

To get further insights into the OER kinetics, EIS was measured at 1.5V (overpotential 270 mV) with a frequency range from 100 kHz to 0.1 Hz. The Nyquist plots and the equivalent electrical circuit are shown in **Figure 4. 20a**. Both the NiFeRu and NiFeCoRu electrocatalysts exhibited almost similar intrinsic resistance, while the NiFe/Au shows the smallest R_{ct} value (6.4Ω) among the measured samples. This small resistance is ascribed to NiFe LDHs-gold interfacial interactions, which lead to charge redistribution of the active site and give rise to the free charge carrier concentration, thus facilitating the charge-transfer process during the OER.^[159, 161, 256] The intrinsic activity of NiFe-based LDHs was further confirmed by the turnover frequencies (TOFs) in **Figure 4. 20b**. The NiFe/Au exhibit TOFs of $0.42 s^{-1}$ at an overpotential of 300 mV, which is almost six times that of the pure NiFe LDHs nanosheets. Above all, the universality of the synthesis strategy used to prepare NiFe-based multi-metal LDHs was confirmed and the OER performance was improved by ruthenium doping and gold modification.

4.1.8. Conclusion

In conclusion, a new synthesis method has been developed to prepare easily exfoliated NiFe-based LDHs monolayers. The structure, structure evolution, and the universality of this strategy were confirmed by XRD, TEM, FT-IR, and AFM. Different from the typically NiFe LDHs, the obtained NiFe LDHs can be easily exfoliated into monolayer nanosheets, resulting in excellent OER activity, which is significantly better than the corresponding bulk counterpart and noble metal oxide catalysts RuO_2 . Consequently, considering the universality of the method, it is believed that this strategy offers an easy and efficient way for the design and construction of NiFe LDHs and that this strategy can also be extended to the development of various other LDHs-based multifunctional materials for energy conversation and storage, including in the field of electrocatalysts, supercapacitors, and batteries.

4.2. Direct thermal enhancement of hydrogen evolution reaction of on-chip monolayer MoS₂

This section illustrates an on-chip MoS₂ monolayer (MoS₂ ML) reactor and the relationship between the HER performance and its thermal effect on MoS₂ ML. As is already known (in Chapter 2.9 and 2.10), MoS₂ has drawn great attention as a promising alternative to Pt-based catalyst for the HER. However, it suffers from sluggish kinetics to drive the HER process because of inert basal planes. Here, an on-chip MoS₂ ML HER reactor was designed and fabricated to reveal direct thermal enhancement of MoS₂ ML for the HER. The thermal effects, which were confirmed by Raman and PL spectra, generated efficient electron transfer in the atomic MoS₂ ML and at the interface between the electrolyte and the catalyst, leading to enhanced HER activity. The MoS₂ ML measured at a higher temperature (60 °C) possesses significantly enhanced HER activity with a lower overpotential (90 mV at current densities of 10 mA cm⁻²), lower Tafel slope (94 mV dec⁻¹), and higher turnover frequency (73 s⁻¹ at the overpotential 125 mV) compared to the results obtained at room temperature. More importantly, such an understanding of the thermal effect of 2D MoS₂ ML for HER catalysts offers a guideline for the development of the next generation catalyst technology towards hydrogen evolution or other efficient electrocatalysts. The keywords in this section are MoS₂, monolayer, thermal effects, hydrogen evolution, and on-chip.

The core part of this section has been published in *ACS Nano* **2022**, 16, 2, 2921–2927, DOI: 10.1021/acsnano.1c10030, titled: *Direct Thermal Enhancement of Hydrogen Evolution Reaction of On-Chip Monolayer MoS₂*.

4.2.1. Introduction

Hydrogen (H_2), a key energy carrier for energy conversion (hydrogen fuel cells) and storage, plays a major role in the development of sustainable energy for the environment and can be generated through an electrocatalytic HER.^[3] Because multiple elemental reactions induce an accumulation of energy barriers and result in slow kinetics, the HER ($2H^+ + 2e^- \rightarrow H_2$) needs an efficient, durable, and inexpensive catalyst to reduce the overpotential (η).^[1, 257] MoS_2 , an interesting 2D material, has been recognized as a greatly promising alternatives for noble-metal-based catalysts (such as Pt) in the HER.^[199] For instance, the edge sites of MoS_2 are active for the HER, as predicted by both theoretical,^[119, 120] and experimental^[69, 202] studies. However, the basal plane of MoS_2 (anisotropic property of 2D materials) is relatively inert due to its high hydrogen adsorption energy.^[201]

To activate and optimize the inert catalytic activity of the MoS_2 basal planes, enormous research efforts have been devoted to improving catalytic efficiency with chemical methods (including, phases engineering,^[18, 22, 85, 203] strain engineering,^[198, 258] defects engineering,^[259-261] doping,^[93, 94, 262] and amorphous MoS_2 synthesis^[263, 264]) and physic methods (such as electric field effect,^[213, 220, 265] electric field and photoelectrical effect,^[217] and magnetic field effect^[222] enhancement). The key to activating the inert basal plane is to increase the intrinsic catalytic activity by enhancing the electronic transport in the MoS_2 basal plane or at the interface between the electrolyte and catalyst. As reported, the thermal effect can improve the electron transfer efficiency during catalytic reactions.^[266, 267] However, to date, no results have been reported about the temperature-dependent HER based on MoS_2 ML catalyst. Here, an on-chip MoS_2 ML HER reactor was designed and fabricated to investigate the temperature-dependent HER catalyst activity.

4.2.2. Fabrication of on-chip MoS₂ ML devices

The MoS₂ ML was mechanism exfoliated on the substrate from a crystal MoS₂ bulk (SPI Supplies) with gold tape ^[73] and then transferred onto a silicon wafer covered by a 300 nm thick dielectric SiO₂ layer., and the details were disused in Chapter 3.1.3. The on-chip devices for electrocatalysis were fabricated by standard photolithography (MLA 100) and the Cr/Au (1 nm/50 nm) electrodes were deposited by an e-beam deposition. The fabrication process of the WE for HER device is schematically illustrated in **Figure 4. 21**. First, a HER microelectrode array on a single MoS₂ ML was fabricated with ultraviolet lithography and oxygen plasma etching (**Figure 4. 21b**). Then, microelectrodes with MoS₂ ML were fabricated with ultraviolet lithography and electron-beam deposition (Cr/Au, 1 nm/50 nm), which were regarded to build electrical contacts between the MoS₂ ML and outer electrode (**Figure 4. 21c**). Finally, to avoid the influence of the electrode in the HER test, another layer of SU-8 was spun on the silicon wafer as a protective layer and patterned to expose the MoS₂ ML and outer electrode. After lifting-off the photoresists, on-chip MoS₂ ML microelectrodes were obtained (**Figure 4. 21d**). Similarly, the microelectrodes Pt were fabricated as shown in **Figure 4. 22**.

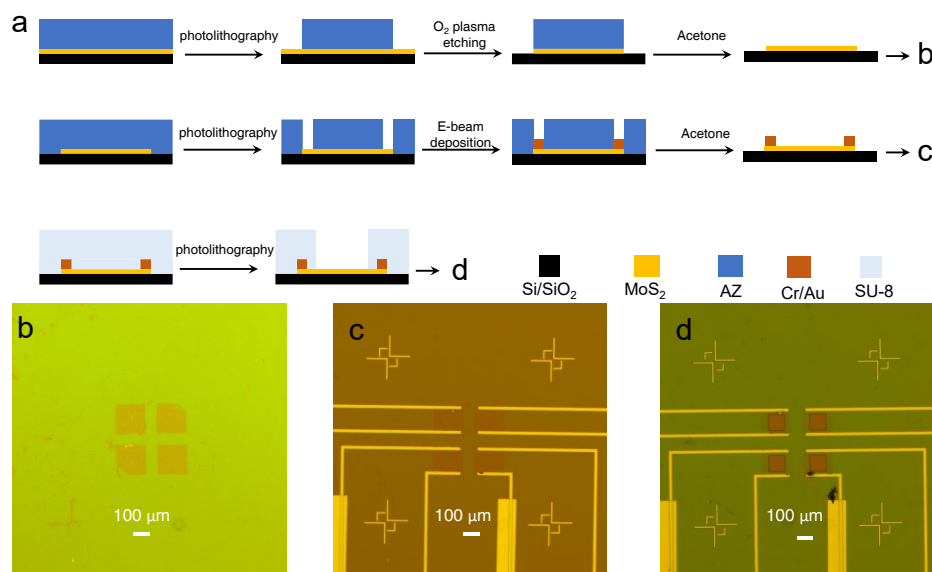


Figure 4. 21 Schematics of the fabrication process and optical microscope images of the MoS₂ ML microelectrode array. (a) Schematic of the fabrication process for MoS₂ ML microelectrode array. Optical microscope image of the patterned (b) MoS₂ ML microelectrode, (c) MoS₂ ML/Cr/Au and (d) MoS₂ ML/Cr/Au/SU-8. AZ is the photoresist AZ5214e.

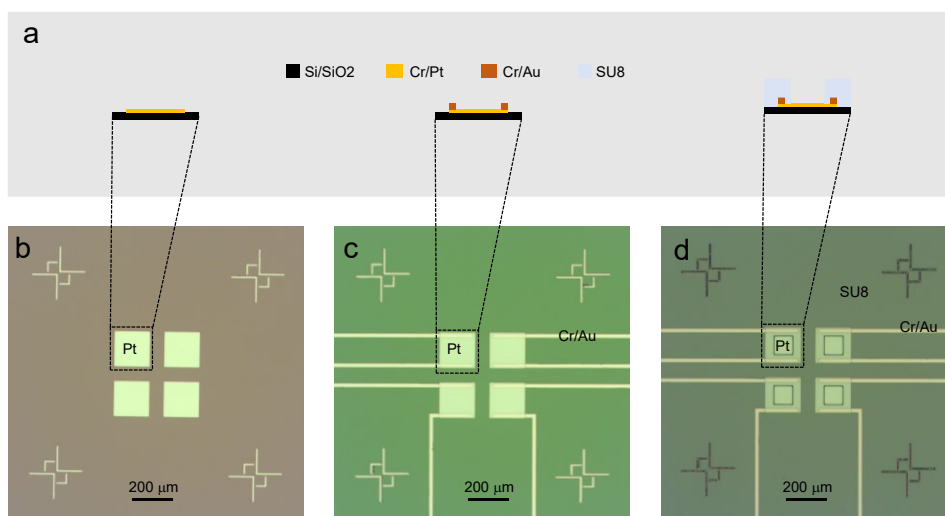


Figure 4. 22 (a) Side-section schematic of Cr/Pt (5 nm/50 nm) microelectrode. Optical microscope image of the patterned (b) Cr/Pt microelectrode, (c) microelectrode Cr/Pt with Cr/Au connection-electrode and (d) Cr/Pt with Cr/Au connection-electrode covered with SU-8 protection layer.

4.2.3. Characterization of MoS₂ ML

In this work, a MoS₂ ML was utilized to investigate the thermal effects on the HER performance. The features of the exfoliated MoS₂ ML were characterized by optic image, Raman, PL, and XPS.

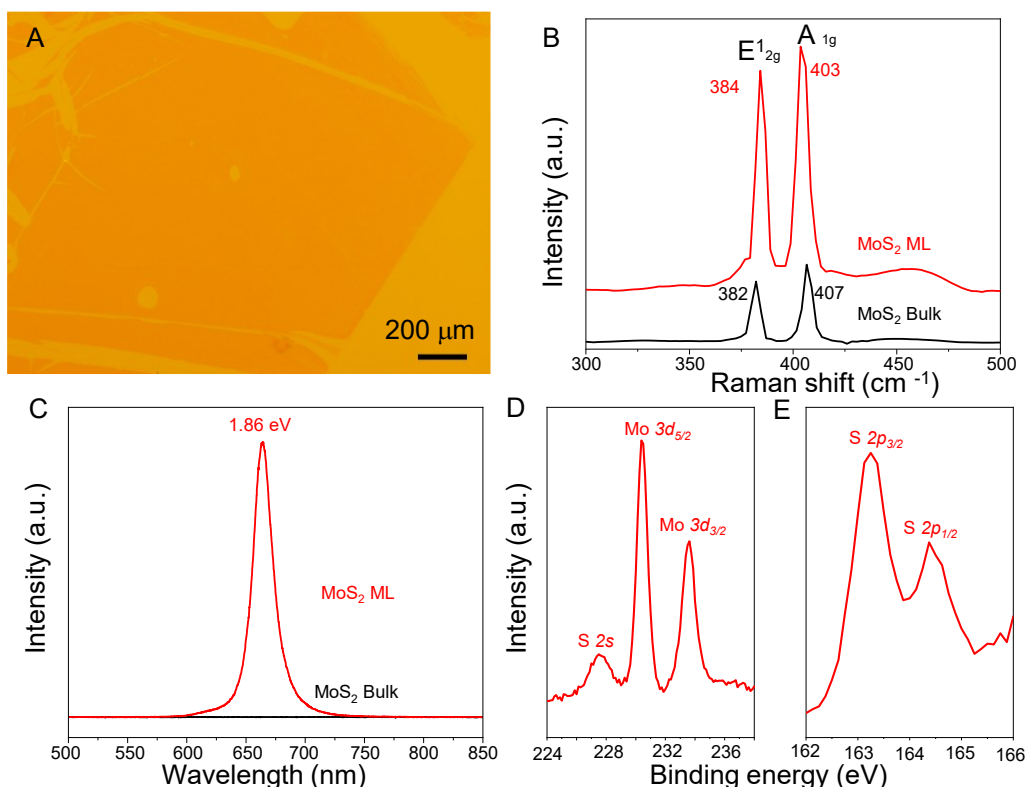


Figure 4. 23 Characterization of exfoliated MoS₂ ML. (A) Optic image of exfoliated MoS₂ ML on a silicon wafer (oxide layer 300nm). (B) Raman and (C) PL comparison of MoS₂ bulk and ML. XPS of MoS₂ ML: (D) Mo3d and (E) S2p. ML: monolayer.

As displayed in **Figure 4. 23A**, the single MoS₂ ML has a large size of up to 1.9 mm. **Figure 4. 23B** compares the Raman spectra of the MoS₂ bulk and MoS₂ ML, revealing two strong peaks assigned to the in-plane (E^{1}_{2g}) and out-of-plane (A^{1}_{g}) vibrations. Clear shifts were observed for the peak positions of the MoS₂ ML. Compared with the MoS₂ bulk, the MoS₂ ML shows a blue shift for E^{1}_{2g} and a red shift for A^{1}_{g} modes. The difference between the two peaks at ~ 384 and ~ 403 cm⁻¹ for the MoS₂ ML adds up to about 19 cm⁻¹, confirming the monolayer configuration.^[268] The PL spectroscopy results also confirm the transition from an indirect (MoS₂ bulk) to a direct (MoS₂ ML)

bandgap material after exfoliation (**Figure 4. 23C**). A single peak at ~ 670 nm (~ 1.86 eV) was observed due to the generation of an A exciton from the direct excitonic transition at the Brillouin zone K point in the MoS₂ ML.^[96] XPS was used to further investigate the surface chemical composition and valence states of the MoS₂ ML. The high-resolution XPS spectra of the Mo 3*d*, S 2*s*, and S 2*p* binding energy regions are shown in **Figure 4. 23D** and **Figure 4. 23E**. The peaks approximately 227.5, 230.5 and 233.6 eV correspond to the S 2*s*, Mo⁴⁺ 3*d*_{5/2} and Mo⁴⁺ 3*d*_{3/2} of the MoS₂ ML, respectively (**Figure 4. 23D**).^[269] The XPS spectra of the S 2*p* region reveal two main features with signals at 163.2 and 164.4 eV, which arise from the S 2*p*_{3/2} and S 2*p*_{1/2} orbitals, respectively (**Figure 4. 23E**).^[22, 69] All of the results indicate that a MoS₂ ML with a large size was exfoliated and successfully transferred onto the silicon wafer.

4.2.4. Laser-induced thermal effects of MoS₂ ML

The laser-induced thermal effects of the MoS₂ ML were investigated by tuning the radiation power from 5.4 to 5400 kW·cm⁻² with a filter (from 0.1 to 100 %) under ambient conditions. The intensities of the Raman and PL spectra show a significant increase as the laser power increases (**Figure 4. 24**). **Figure 4. 25** shows the normalized Raman and PL spectra recorded at various laser powers for the MoS₂ ML. The peak for the E¹_{2g} mode shifts from 384 to 382 cm⁻¹ and the peak for the A_{1g} mode shifts from 403 to 401 cm⁻¹ with increasing laser power (**Figure 4. 25A**). Overall, the A_{1g} and E¹_{2g} modes show redshifts of approximately 2 cm⁻¹ when the laser power increases from 5.4 to 5400 kW·cm⁻², which is consistent with previously published data.^[270] Unlike the MoS₂ ML, the MoS₂ bulk material did not show pronounced changes for either A_{1g} or E¹_{2g} modes, neither for the peak position nor the peak shape as the excitation power was increased (**Figure 4. 24c**).

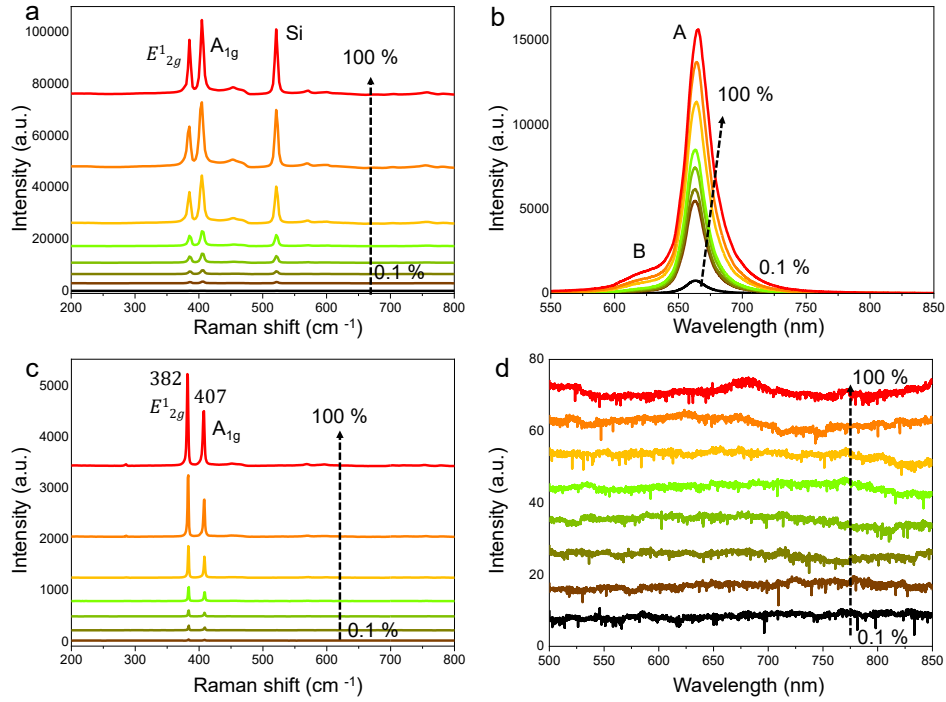


Figure 4. 24 (a) Raman and (b) PL spectra of MoS₂ ML with increasing excitation laser power from 5.4 to 5400 kW·cm⁻² with a filter (from 0.1 to 100 %) at RT under ambient conditions. (c) Raman and (d) PL spectra of MoS₂ bulk with increasing excitation laser power from 5.4 to 5400 kW·cm⁻² with a filter (from 0.1 to 100 %) at RT under ambient conditions.

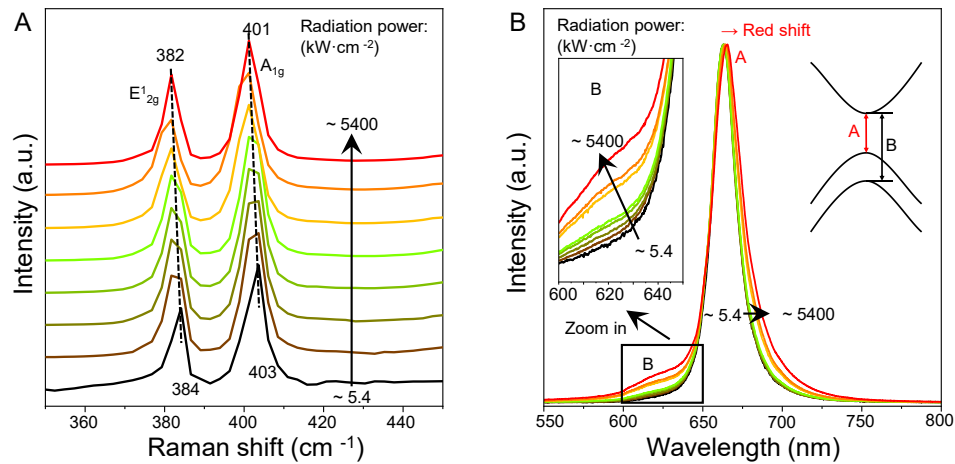


Figure 4. 25 Laser-induced thermal effects in MoS₂ ML. Normalized (A) Raman and (B) PL spectra of MoS₂ ML at increasing excitation laser power from 5.4 to 5400 kW·cm⁻² with a filter (from 0.1 to 100 %) under ambient conditions. Zoomed-in details of B exciton in the MoS₂ ML (insert of B, left) and schematic illustration of the band structure of MoS₂ ML at the K points (insert of B, right).

The normalized PL spectra of the MoS₂ ML show only one peak from the A exciton at low laser power (**Figure 4. 25B**). A new peak, centered at $\lambda = 620$ nm (B exciton), was detected as the laser power increased. This can be attributed to thermal effects resulting from high-density laser irradiation (insert of **Figure 4. 25B**, left).^[97, 271] In contrast, no notable peak was observed for the PL spectra of the MoS₂ bulk even when the laser power was increased to 5400 kW·cm⁻² (**Figure 4. 24d**). The double PL peaks of the MoS₂ ML are attributed to the direct excitonic transition at the Brillouin zone K point for A exciton and B exciton with higher laser irradiation (insert of **Figure 4. 25B**, right)^[272]. Furthermore, the A exciton in the PL peak of MoS₂ ML shows a slight red shift under a higher laser power (**Figure 4. 25B**).^[273, 274] The thermal effects of the MoS₂ ML were revealed and confirmed by Raman and PL results at a higher radiation power.

4.2.5. Temperature-dependence of HER on MoS₂ ML

An integrated on-chip MoS₂ ML HER reactor was fabricated and employed to explore the relationship between the HER catalytic performance and thermal effects in MoS₂ ML. The fabrication process of the MoS₂ ML HER reactor was exhibited in the experimental section (Chapter 4.2.2).

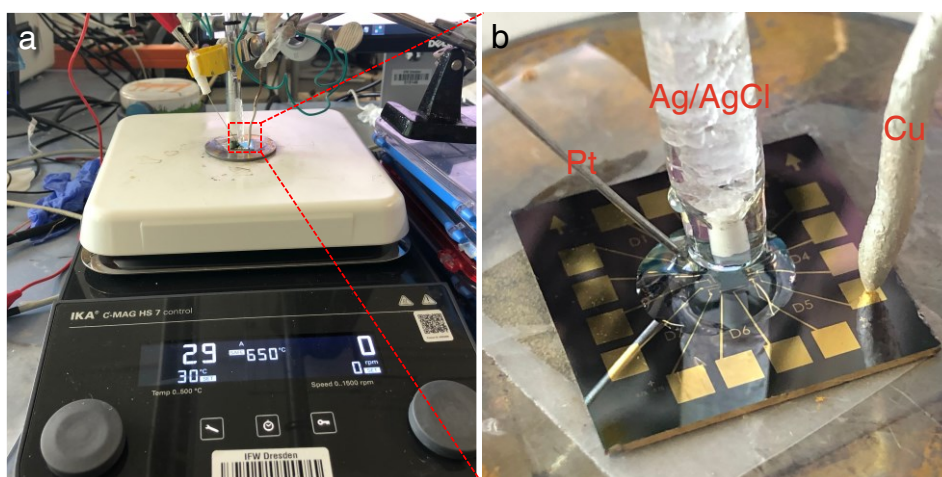


Figure 4. 26 The setup for evaluating the temperature-dependence of HER on an on-chip MoS₂ ML. (a) IKA temperature heater and (b) on-chip MoS₂ ML devices.

Figure 4. 26 displays the setup for evaluating the temperature dependence of HER in MoS₂ ML. **Figure 4. 27A** shows a schematic illustration of the on-chip measurement setup (three-electrode system). The on-chip MoS₂ ML HER reactor is acted as the WE. A platinum wire was used as the CE and a Ag/AgCl acts as the RE. One droplet of nitrogen (N₂)-purged H₂SO₄ (0.5 M) electrolyte was used for the HER performance measurement. Moreover, a temperature controller was placed under the on-chip device to record the HER performance of the MoS₂ ML to thermal effect (**Figure 4. 27B** and **Figure 4. 26**). As already discussed in **Figure 4. 24** and **Figure 4. 25**, thermal effects in the MoS₂ ML are revealed at higher temperatures. In particular, hot carriers (e⁻) will promote the HER process ^[275]. The HER electrocatalytic activities based on thermal activation for a MoS₂ ML were investigated from RT (25 °C) to 60 °C with a step size of 5 °C. The polarization curves in **Figure 4. 27C** clearly show that the catalytic activity of the MoS₂ ML is largely enhanced as the temperature increases. The current density of the MoS₂ ML at 60 °C (145.6 mA cm⁻²) was raised 45.5 times compared to the results at RT (3.2 mA cm⁻²) at an overpotential of 200 mV. For comparison, platinum (Pt) film microelectrodes were fabricated (**Figure 4. 22**), and the temperature-dependence behavior of Pt microelectrodes was investigated. As shown in **Figure 4. 28**, the current density of the Pt microelectrode at 60 °C shows an increase of approximately 2 times compared with RT at an overpotential of 200 mV. The overpotentials of the MoS₂ ML are 201, 170, 126, 120, 110, 102, and 90 mV at a current density of 10 mA cm⁻² at 30, 35, 40, 45, 50, 55, and 60 °C on the same MoS₂ ML, respectively (**Figure 4. 27C**), which documents a considerable HER enhancement compared to the results measured at RT. Interestingly, as displayed in **Figure 4. 27D** and **Figure 4. 27E**, the Tafel slope of 136.7 mV dec⁻¹ drastically reduces to 94.0 mV dec⁻¹ with increasing temperature from RT to 40 °C (region I).

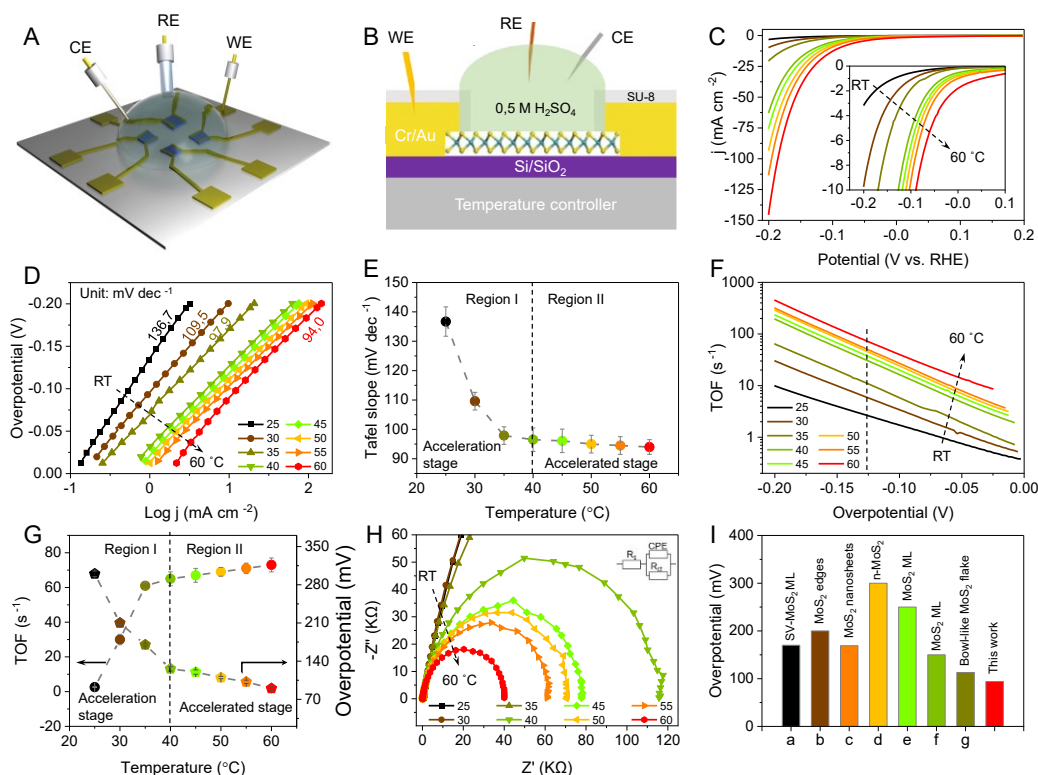


Figure 4. 27 Temperature-dependence of HER properties on MoS₂ ML. (A) Schematic illustration and (B) Cross-section of the on-chip measurement setup. WE: working electrode, CE: counter electrode, and RE: reference electrode. (C) Polarization curves of MoS₂ ML and corresponding (D) Tafel plots were obtained from the polarization curves over a temperature range from RT to 60 °C. (E) Tafel slope as a function of the temperature for lower temperature (Region I) and higher temperature (Region II). (F) TOF as a function of the overpotential. (G) Overpotential and TOF in lower temperature (Region I) and higher temperature (Region II) regions. Error bars represent standard deviations of four independent tests. (H) Nyquist plots for MoS₂ ML at potentials -0.1 V vs. RHE (overpotential at 100 mV) from RT to 60 °C. (I) Overpotential (at 10 mA cm⁻²) comparison with other reported on-chip MoS₂ devices. a-g represent the on-chip MoS₂ catalyst for SV-MoS₂ ML,^[198] MoS₂ edges,^[20] MoS₂ nanosheets,^[217] n-MoS₂,^[23] MoS₂ ML,^[218] MoS₂ ML,^[276] and bowl-like MoS₂ flake,^[222] respectively.

Based on previous research findings, the adsorption of H⁺ onto the catalyst (Volmer step, the Tafel slope would be ≈ 120 mV dec⁻¹) is the rate-limiting step for HER at RT. The acceleration stage in the region I indicates that the number of hot carriers rises as the temperature increases, leading to the reduction of adsorption energy on the inert

basal planes of the MoS₂ ML and the acceleration of the electrocatalytic reaction kinetics, which result in a lower Tafel slope (**Figure 4. 27E**).^[201] Moreover, there is no major difference for the Tafel slopes when the temperatures increase further in region II (40 to 60 °C) because of the saturation of the hot carriers (**Figure 4. 27E**). Thus, the variation in the electrical transport induced by thermal effects (hot carriers) is the origin of the enhanced catalytic performance of MoS₂ ML at higher temperatures. The turnover frequency (TOF) per surface Mo atom on MoS₂ ML at different temperatures was calculated. As displayed in **Figure 4. 27F** and **Figure 4. 27G**, the TOF of MoS₂ ML measured at 60 °C exceeded that at RT by a factor of 10 to 40. In region I, the TOF of the MoS₂ ML is 63.0 s⁻¹ at 40 °C, while the TOF value is only 2.6 s⁻¹ at RT for the same overpotential of 125 mV. Meanwhile, the overpotential of the MoS₂ ML decreased from 300 mV (RT) to 120 mV (40 °C) at a current density of 10 mA cm⁻². There is no major change in the overpotential and TOF values in MoS₂ ML when the temperature increases further in region II (**Figure 4. 27G**). This improvement in the TOF shows that the thermal effect has a great effect on the HER performance of MoS₂ ML. Electrochemical impedance spectroscopy (EIS) was applied to investigate the electrode kinetics in a frequency ranging from 100 kHz to 0.1 Hz at an overpotential of 100 mV. The Nyquist plots and the equivalent electrical circuits are shown in **Figure 4. 27H** and **Figure 4. 29**. Clearly, the charge transfer resistance (R_{ct}) decreases from 440kΩ to 18kΩ as the temperature increases from RT to 60 °C, indicating the high efficiency of electron transfer onto the MoS₂ ML. The EIS results confirm that the external thermal effect not only accelerates the electronic transport in the MoS₂ basal plane, but also increases electronic transport in the MoS₂ ML basal plane, but also increases electronic transport at the interface between the electrolyte and the MoS₂ surface. **Figure 4. 27I** and **Table 4** compare the overpotential of on-chip MoS₂-based microelectrodes.^[20, 23, 198, 217, 218, 222, 276] The MoS₂ ML measured at a higher temperature in this study possesses superior HER performance compared to other on-chip MoS₂-based HER catalysts at RT.

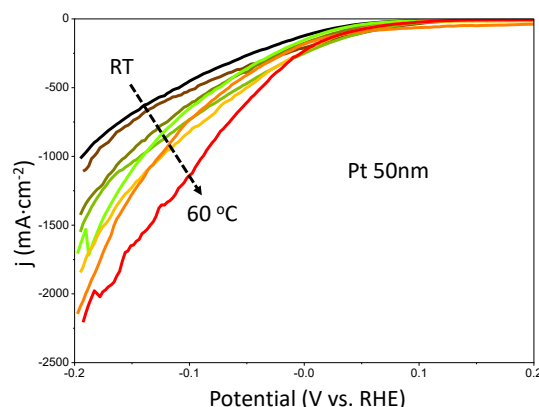


Figure 4. 28 LSV of Cr/Pt microelectrode over a temperature range from RT to 60 °C.

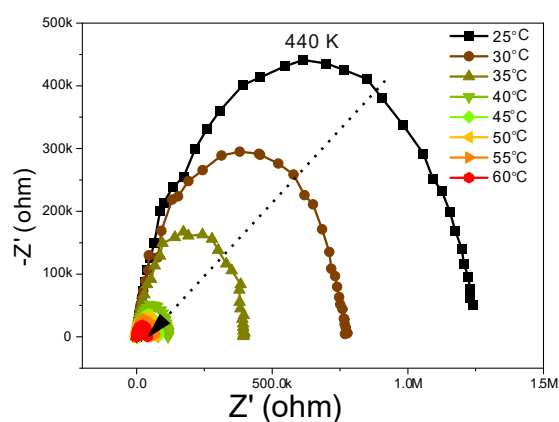


Figure 4. 29. Nyquist plots of MoS₂ ML at applied potentials -100 mV vs. RHE under different temperatures from RT to 60 °C.

Table 4 Comparison of the on-chip HER performance of this report (at 60 °C) as well as other reported on-chip MoS₂ results at RT: (overpotential (η) mV, at 10 mA cm⁻²), Tafel slope (mV·dec⁻¹) and TOF (s⁻¹).

Electrocatalysts	Overpotential (η)	Tafel slope	TOF	Active methods	Reference
MoS ₂ ML	-90	94.0	73 (η =125mV)	Thermal effect (60 °C)	This work
MoS ₂ ML	~ -300	136.7	2.6 (η =125mV)	RT (25 °C)	This work
SV-MoS ₂ ML	-170	60	10(η =125mV)	Strained sulfur vacancies	[198]
Metallic MoS ₂ edges	-200	50	1 (η =100mV)	metallic MoS ₂ edges	[20]
MoS ₂ nanosheets	-169	100	-	Electric field (3 V), photoelectrical (60 mW/cm ²)	[217]
n-type MoS ₂	-300	-	-	FET (50 mV)	[23]
ML MoS ₂	-250	109	-	FET (1 V)	[218]
MoS ₂ ML	-150	75	-	Boundary activated	[276]
Bowl-like MoS ₂ flake	-113	59	-	Magnetic Enhancement	[222]

To better understand the thermal enhancement of the HER performance of MoS₂ ML, the activation energy, that is, the relation between the temperature and current density, from the Arrhenius equation was studied.^[266] The Arrhenius relation is given by

$$\ln(j) = \ln A - \frac{E_a}{R} \frac{1}{T} \text{ or } \log(j) = \log B - \frac{E_a}{2.3R} \frac{1}{T}, \text{ 4-1}$$

where E_a is the apparent activation enthalpy at the reversible potential, j is the current density, R is the gas constant, and T is the absolute temperature. A and B are pre-exponential factors.^[277]

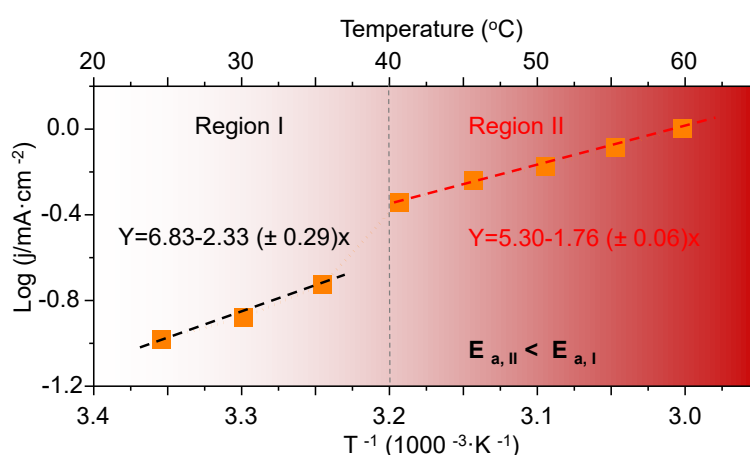


Figure 4. 30 Arrhenius plots of the exchange current densities on the MoS₂ ML vs. temperature from RT (25) to 60 °C.

The current density from the Tafel slope (**Figure 4. 27D**) and the Arrhenius plots were calculated and are drawn in **Figure 4. 30**. Clearly, Arrhenius plots show different linear relationships between the current densities on the logarithmic scale and the reciprocal temperature ($1/T$) for the MoS₂ ML at higher temperatures and lower temperatures. The Arrhenius plots display smaller slopes at higher temperatures (region II) than the values at lower temperatures (region I) for the same MoS₂ ML (**Figure 4. 30**). The activation energies of the MoS₂ ML for HER were calculated through the slopes of Arrhenius plots. The activation energies are 33.65 ± 1.15 kJ/mol for region II ($E_{a,II}$) and 44.55 ± 5.54 kJ/mol for the region I ($E_{a,I}$). It is implied that the higher temperatures conditions are thermodynamically favorable in the case of MoS₂ ML for

the HER. Hence, the increase in temperature leads to a significant improvement in the HER catalytic activity of the MoS₂ ML.

4.2.6. Side effects of HER on MoS₂ ML

In order to confirm the thermal enhancement of HER on MoS₂ ML, side effects were also discussed below, including the effect of substrate, contact resistance, and CE.

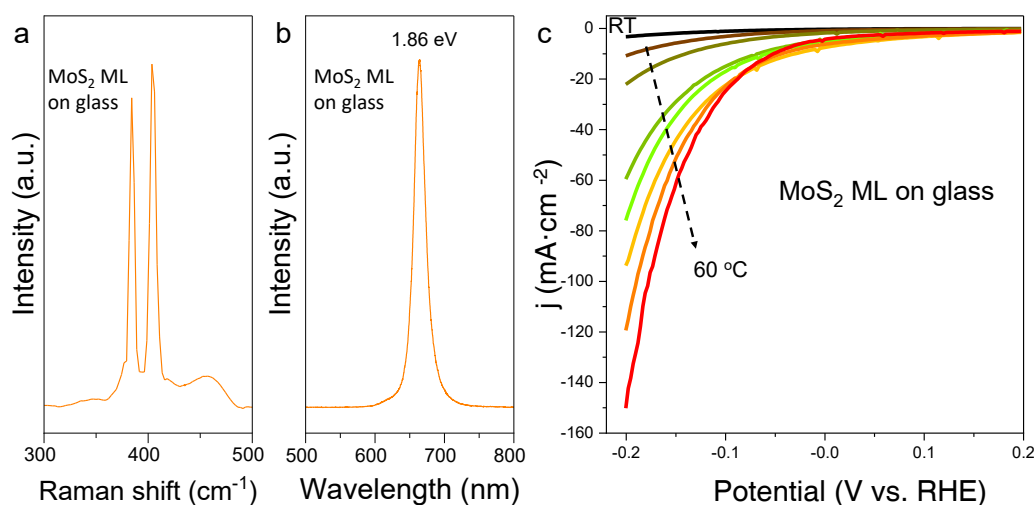


Figure 4. 31 Characterization of exfoliated MoS₂ ML on glass. (a) Raman and (b) PL spectra of the MoS₂ ML on a glass substrate. (c) Polarization curves of the MoS₂ ML on glass over a temperature range from RT to 60 °C.

To investigate the substrate effect, a MoS₂ ML was exfoliated and transferred onto a glass substrate. Then, microelectrodes were fabricated. **Figure 4. 31a** and **b** display the Raman and PL spectra of the MoS₂ ML on glass, confirming that the MoS₂ ML were successfully exfoliated and transferred onto the glass. The HER performance of MoS₂ ML on glass was investigated. The polarization curves in **Figure 4. 31c** clearly show that the catalytic activity of the MoS₂ ML is also largely enhanced as the temperature increases. Comparing the HER results of the MoS₂ ML on a silicon wafer (**Figure 4. 27C**) and glass (**Figure 4. 31c**), the substrate (silicon wafer vs. glass substrate) shows little or no effect on the HER of MoS₂ ML.

The contact resistance of MoS₂ ML, which was obtained from EIS in **Figure 4. 27H**, was also discussed. As displayed in **Figure 4. 32a**, the contact resistance decreases with increasing temperature. To investigate the contact resistance effect on the HER performance, polarization curves of the MoS₂ ML under different temperatures with iR compensation were calculated (**Figure 4. 32b**). There is no difference for the polarization curves (**Figure 4. 27C** and **Figure 4. 32b**) and the areal activity (**Figure 4. 32c**) of the MoS₂ ML under different temperatures with or without iR compensation. That means, although the contact resistance decreases with increasing the temperature of the measurement environment, the HER performance shows nearly no difference whether the contact resistance was considered or not. Therefore, compared to the thermal effect, the contact resistance can be ignored.

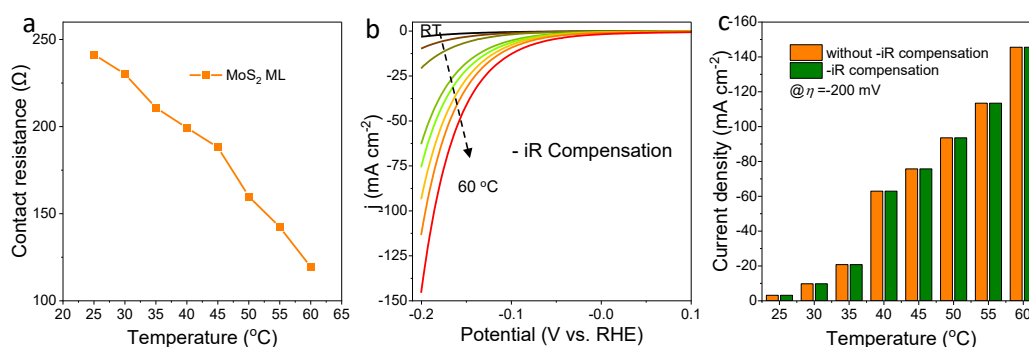


Figure 4. 32 (a) Contact resistance of the MoS₂ ML under different temperatures in H₂SO₄ solution, which was obtained from EIS in **Figure 4. 27H**. (b) Polarization curves of the MoS₂ ML under different temperatures with iR compensation. (c) Activity comparison of the MoS₂ ML with/without iR compensation under different temperature. HER current density normalized to the areal activity, respectively, at the overpotential of 200 mV.

As reported, the platinum (Pt) can transfer from the anode (CE) to the cathode (WE), which will lead to an efficient enhancement of the WE when the Pt wire was used as the CE.^[278] In order to avoid side effects of the Pt as the CE, the HER catalytic performance of the MoS₂ ML and Pt film microelectrode were re-checked by using glassy carbon (d= 3 mm) as a CE. As displayed in **Figure 4. 33**, both MoS₂ ML and Pt film microelectrode show thermal enhancement to HER, which is similar to the results of using Pt as the CE.

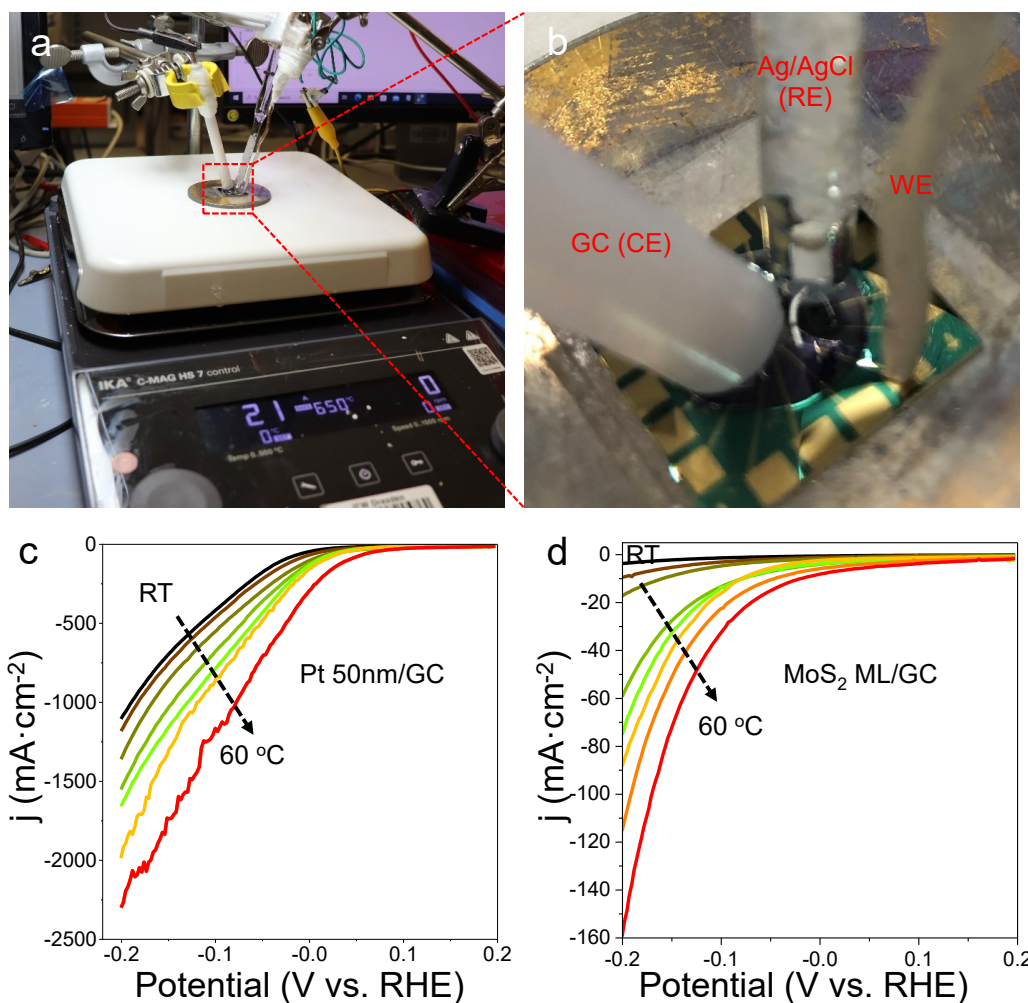


Figure 4. 33 Setup for evaluating the temperature-dependent HER of the MoS₂ ML by using GC as a CE. (a) The temperature was controlled by IKA hot plates under the working electrode. (b) Optical image of the MoS₂ ML microelectrode. Polarization curves of (c) the Pt film and (d) the MoS₂ ML over a temperature range from RT to 60 °C by using glassy carbon ($d = 3$ mm) as a CE.

After carefully comparing the previous results ^[278] with our measurement results (Figure 4. 27C, Figure 4. 28, and Figure 4. 33), we can conclude that the enhancement of HER on the MoS₂ ML and Pt microelectrodes is because of the thermal effect rather than the Pt transfer from the anode to the cathode. The reasons are as follows. First, the HER enhancement, and Pt transfer was observed after 10000 CV cycles in the previous paper, ^[278] while our measurement was carried out in a short time. There is not sufficient time for the complex reaction processes to happen, including absorption of OH⁻ or H₂O on the Pt surface, the evolution of oxygen species and their reaction with the Pt atoms, position exchange between oxygen and Pt atoms, and the

dissolution of Pt and transfer of Pt. Second, for the Pt microelectrode, our tested results are consistent with the published paper,^[266] which also shows a temperature-dependent Tafel slope for the HER. The thermal enhancement of HER on MoS₂ ML was further confirmed after analyzing the side effects of the reaction.

4.2.7. Stability of HER on MoS₂ ML

The stability of MoS₂ ML was also evaluated under various temperature conditions. The chronoamperometry (j - t) test was performed with the MoS₂ ML material at a constant potential of -200 mV versus RHE, as shown in **Figure 4. 34**. The stability curve directly displays the trend of current density changing as the temperature changes. The test temperature was set at RT with a current density of about 3 mA cm⁻². Then, the current density was increased to 12 mA cm⁻² as the temperature increased to 30 °C. After the temperature was lowered to RT, the current density was decreased again to approximately 3 mA cm⁻². By increasing the temperature to 40 °C, the current density increased to 40 mA cm⁻², which is roughly 3 times greater than at 30 °C and 10 times more than at RT. Moreover, the long-term stability of the MoS₂ ML was evaluated in an IKA constant-temperature water bath (**Figure 4. 35**). To protect the RE (Ag/AgCl), the j - t curves were only recorded at 25 °C and 30 °C.

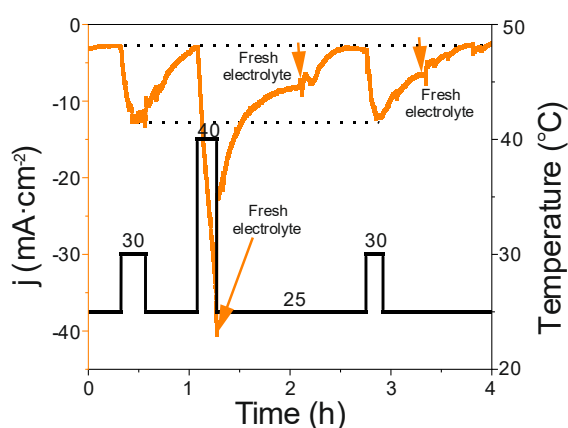


Figure 4. 34 HER Stability on MoS₂ ML. Temperature-dependent current density curve for MoS₂ ML catalyst at a constant overpotential of -200 mV versus RHE under different temperatures (orange curve). The schematic illustration of the set temperature with the IKA temperature controller (black line).

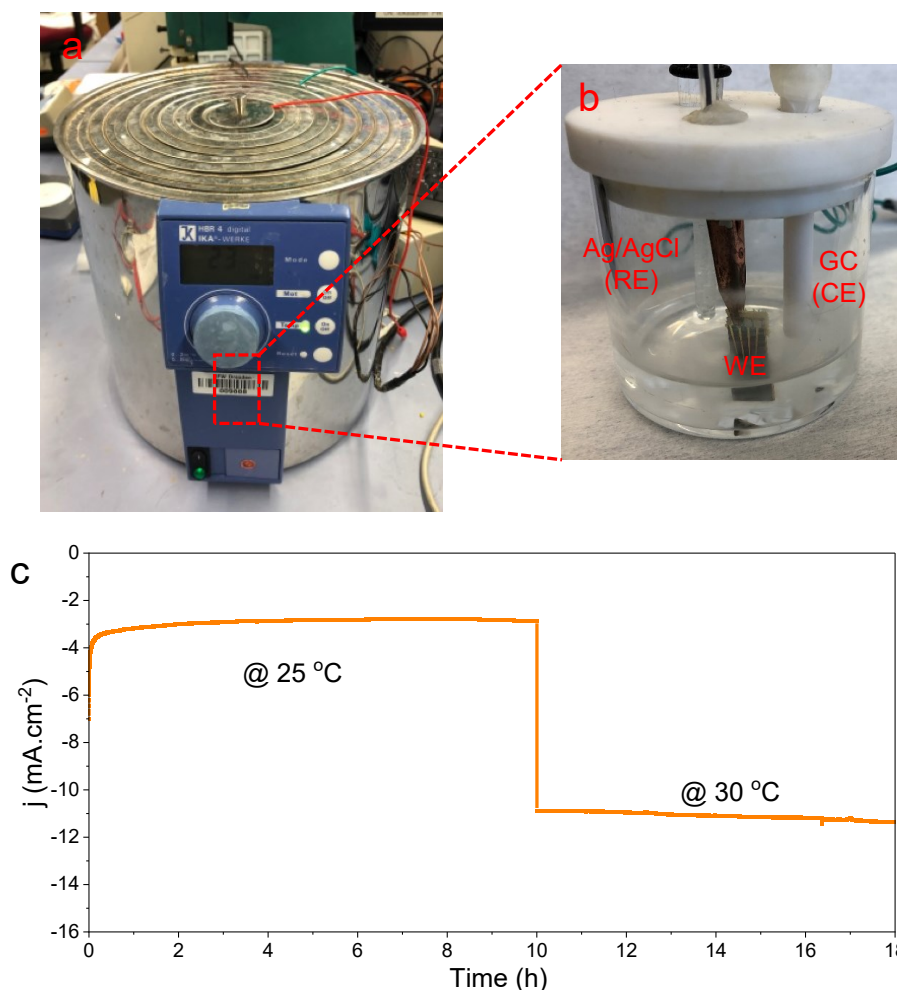


Figure 4. 35 HER Stability of the MoS₂ ML. Temperature-dependent current density curve for the MoS₂ ML catalyst at a constant overpotential of -200 mV versus RHE in an IKA constant temperature water bath at 25 °C and 30 °C.

As displayed in **Figure 4. 35**, the MoS₂ ML shows good temperature-dependent behavior and stability. The results demonstrate that the thermally enhanced MoS₂ ML owns good stability of HER performance at various temperatures. Afterward, Raman and PL spectra were recorded to study the structure of the MoS₂ ML (**Figure 4. 36**). In comparison to the exfoliated MoS₂ ML in **Figure 4. 23B-C**, there is no obvious difference in the Raman and PL spectra of the MoS₂ ML, which indicates that the thermal effect achieves efficient electron transfer in the inert MoS₂ basal plane without structural changes of MoS₂ ML.

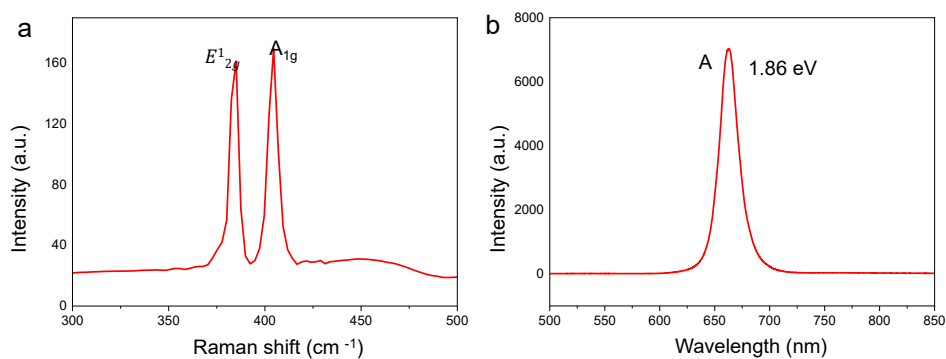


Figure 4. 36 (a) Raman and (b) PL of MoS₂ ML after stability testing.

4.2.8. Conclusion

In summary, the temperature dependence of the HER of an on-chip MoS₂ ML was investigated. The results show that an efficient electron transfer is triggered under higher temperature conditions, which leads to a significantly enhanced HER performance by activating the inert MoS₂ ML basal plane and generating efficient electron transfer at the interface between the electrolyte and catalyst. Lower HER overpotential (90 mV at a current density of 10 mA cm⁻²) is achieved at 60 °C. This work not only provides a strategy to enhance the HER catalytic properties of MoS₂ MLs but also lays the foundation for the future studies of the HER mechanism of 2D monolayers, providing the possibilities for designing the high-performance HER catalysts for energy conversion based on thermal effects.

5. Summary and outlook

This chapter includes the basic conclusions from previous chapters and the potential outlook of the research topic based on exfoliated 2D monolayers for the sustainable development of society, through energy conversion technologies via OER/HER.

5.1. Summary

This doctoral thesis is focused on the exfoliated 2D monolayers used for OER/HER with bottom-up and top-down methods, including NiFe-based monolayer and MoS₂ monolayer. The preparation (exfoliation) process of materials, materials structure and morphology, and electrochemical performance are presented. These studies include the following aspects.

Part 1 One-pot synthesis of LDHs monolayer

- (1) A one-pot strategy was reported to synthesize the NiFe-based LDHs monolayer.
- (2) The interlayer spacing of LDHs can be tunneled by varying the hydrolysis reagents.
- (3) The universality of this strategy ensures the extension of NiFe LDHs to NiFe-based multi-metal LDHs by doping or modification.
- (4) The NiFe LDHs monolayers show enhanced OER activity than that of the NiFe LDHs bulk counterpart.
- (5) The OER activity of LDHs monolayer can be further improved by metal doping or modification.
- (6) This facile strategy gives a good example of designing LDHs monolayer for highly active catalysts, and even for energy conversion and storage based on 2D superlattices LDHs-multifunctional materials.

Part 2 On-chip MoS₂ ML HER reactor

- (1) A MoS₂ ML with large size was obtained with a top-down method.
- (2) On-chip MoS₂ ML reactor was fabricated and the relationship between the HER performance and the thermal effect on MoS₂ ML was studied.

- (3) The thermal effect of MoS₂ ML was observed and confirmed by Raman and PL.
- (4) The thermal effects afford efficient electron transfer in the atomically MoS₂ ML and at the interface between the electrolyte and catalyst, leading to an enhanced HER performance.
- (5) The understanding of the thermal effect on HER catalysts offers a guideline for the development of the next generation catalyst technology towards hydrogen evolution or other efficient electrocatalysts based on the 2D monolayer.

5.2. Outlook

Though new designs were used to exfoliate the 2D monolayer materials with bottom-up and top-down methods, two kinds of 2D monolayer were obtained and its catalytic activity for the OER/HER was presented. Many aspects still need to be studied in detail to develop a highly efficient 2D monolayer electrocatalyst.

(1). For the LDHs, from the view of the synthetic chemistry, edge/vacancy abundant LDHs will provide better OER performance. Moreover, 2D LDHs monolayer is an ideal host for a single atom that LDHs/single-atom catalysts will become a hot spot in research and application. In short, cheap high-valence metals with special crystal planes, oxygen vacancy, and single-atom catalysts are potential OER catalysts for future applications.

(2). For on-chip MoS₂ ML, it is an ideal platform to monitor the reaction path or reaction mechanism by combining the in-situ equipment, including, Raman spectroscopy, X-ray absorption spectroscopy (XAS), XPS, Mössbauer spectroscopy, ultraviolet-visible spectroscopy, differential electrochemical mass spectrometry, surface interrogation scanning electrochemical microscopy, etc.

List of Figures and Tables

Figure 2. 1 Structure of 2D materials family: atomic structure of top and side view for different types. ^[29]	13
Figure 2. 2 Schematic illustrations of typical 2D monolayer synthesis methods. (a) Top-down strategies for the exfoliation of 2D bulk layered crystals through mechanical cleavage and ion-exchange exfoliation methods. (b) Bottom-up synthesis of 2D monolayers using liquid-phase growth or epitaxial growth methods.	14
Figure 2. 3 Sustainable energy future. Schematic of a sustainable energy landscape based on electrocatalysis. ^[3]	17
Figure 2. 4 Catalyst development strategies. Schematic of various catalyst development strategies, which aim to increase the number of active sites and/or increase the intrinsic activity of each active site. ^[3]	18
Figure 2. 5 Water splitting. (a) Schematic of water splitting. (b) The standard reaction of water splitting. ΔG represents activation energy, $n = 2$ for 2 electron transfer in the reaction and $F = 96485.3329 \text{ s} \cdot \text{A/mol}$ (Faraday constant). E° denotes the standard reversible electrode potential of water splitting. (c) Pourbaix diagram of water. (d) Representative polarization curves of OER, ORR, HOR, and HER. ^[109] (e) Generalized polarization curve for an electrochemical power conversion device with multiple sources of overpotential. ^[110]	20
Figure 2. 6. Schematic structural configurations of 2D LDHs and TMDs. (a) The idealized structure of carbonate-intercalated LDHs with different M^{2+}/M^{3+} molar ratios shows the metal hydroxide octahedrons stacked along the crystallographic c-axis, as well as water and anions present in the interlayer region. ^[135] (b) Structural polymorphs of bulk TMDs with 1T, 2H, and 3R phases structure. ^[136]	22
Figure 2. 7 (a) The OER mechanism for acid (blue line) and alkaline (red line) conditions. ^[2] The black line indicates that the oxygen evolution involves the formation of a peroxide ($\text{OOH}_{(\text{ad})}$) intermediate (black line) while another route for the direct reaction of two adjacent oxo ($\text{O}_{(\text{ad})}$) intermediates (light green line) to produce oxygen is possible as well. (b) Gibbs free energy of reactive species and intermediates (horizontal lines) of the OER versus the reaction coordinate at three different electrode potentials. ^[139] (c) The thermodynamic overpotential associated with elementary steps of the OER and the total energy of adsorption at the reversible electrode potential on a real and ideal catalyst surface. ΔG_i denotes the free reaction energy of the two elementary reactions steps and the order is $\Delta G_3 > \Delta G_1 = \Delta G_2 > \Delta G_4$. ^[139] (d) OER volcano plot for metal oxides. ^[3]	24
Figure 2. 8 Strategies to enhance the OER activity based on 2D NiFe LDHs by synthesizing controllable structures (hierarchical ^[155] or ultrafine ^[156] structure); synthesizing nanocarbon/LDHs (in-situ ^[152] or self-assembly ^[33] methods); synthesizing multi-metal LDHs (doping ^[160] and gold modification ^[159]) and exfoliation of LDHs (ion exchange ^[19] or etching-assisted ^[43] methods).....	27
Figure 2. 9. Mechanisms and activity trend of HER catalysis. (a) The mechanism of hydrogen evolution on the surface of an electrode in acidic solutions. ^[118] Standard free energy diagram for the (b) Volmer-Heyrovsky and (c) Volmer-Tafel route on Pt (111). ^[194] (d) Calculated free energy diagram for hydrogen evolution at a potential $U = 0$ relative to the standard hydrogen electrode at	

pH = 0.^[120] (e) Exchange current density versus MoS₂ edge length.^[119] (f) The Sabatier plot for HER catalysts shows the exchange current densities plotted against the free energy of hydrogen adsorption for metals and MoS₂.^[3]33

Figure 2. 10 On-chip MoS₂ HER reactors. Development history of on-chip electrocatalytic microdevices. Strained sulphur vacancies,^[198] and edge-exposed MoS₂^[20]; field-tuned MoS₂ nanosheets,^[213] field-tuned VSe₂ nanosheets,^[214] and edge and basal-plane sites^[215]; etched MoS₂ edge sites,^[216] edge/basal plane sites,^[21] electric field and photoelectrical effect,^[217] 1T-MoS₂^[22], self-gating,^[23] electrolyte gating,^[218] anisotropic properties,^[219] field-modulation,^[220] and single atomic vacancy catalysis^[204]; grain boundaries,^[221] magnetic enhancement,^[222] and in-site measurement.^[223]35

Figure 3. 1 Scheme of the experimental (a) oven and (b) hydrothermal reactor used for carrying out the NiFe LDHs. A hydrothermal reactor is mainly made up of two parts: an outer high-quality stainless-steel jacket and an inner Teflon chamber.39

Figure 3. 2 Schematic of technologies of photolithography.40

Figure 3. 3 Schematic of the electron beam evaporation system.....41

Figure 4. 1 (a) Schematic of the preparation process of NiFe LDHs bulk and monolayers. (b) XRD pattern of NiFe LDHs. The standard pattern of the pristine NiFe LDHs (JCPDS 40-0215). (c) The photographs of NiFe LDHs colloidal solution under laser irradiation.57

Figure 4. 2 SEM images of NiFe LDHs: (a) low magnification and (b) high magnification. (c) EDS pattern of NiFe LDHs over the full area. The inset in figure (c) shows one selected area of NiFe LDHs and atomic ratios of nickel (Ni), iron (Fe), and oxygen (O) in NiFe LDHs calculated from five different areas.....58

Figure 4. 3 TEM images of NiFe LDHs. (a) TEM image of NiFe LDHs bulk and corresponding SAED pattern (inset). (b) TEM image of exfoliated NiFe LDHs nanosheets and corresponding SAED pattern (inset). (c) HRTEM images of NiFe LDHs monolayers and the corresponding diffractogram pattern are marked in the red square area (inset). (d) HRTEM image of the cross-section of NiFe LDHs...59

Figure 4. 4 AFM images and the corresponding height profiles of the NiFe LDHs.61

Figure 4. 5 (a) XRD patterns of LDHs obtained at various hydrolysis reagent (the ratio of HMT to urea). (b) (003) and (006) peaks shift of XRD patterns of the obtained as-prepared LDH samples varying hydrolysis reagent between urea and HMT.....62

Figure 4. 6 Raman of LDHs obtained at various hydrolysis reagents (the ratio of HMT to urea)....63

Figure 4. 7 (a) FT-IR spectra of the LDHs. Prepared from pure HMT to pure urea. (b) Region characteristic for NO₃⁻ and CO₃²⁻ in the NiFe LDHs.....63

Figure 4. 8 Schematic diagram of NiFe LDHs samples: (a) NiFe LDHs₀ (NiFe LDHs_{CO₃²⁻}) prepared by using urea as hydrolysis reagent) and (b) NiFe LDHs (NiFe LDHs_{NO₃⁻} prepared by using HMT as hydrolysis reagent).64

Figure 4. 9 XPS spectra comparison of NiFe LDHs (NiFe LDHs_{NO₃⁻}) and NiFe LDHs₀ (NiFe LDHs_{CO₃²⁻}). (a) Survey, (b) Ni 2p, (c) Fe 3p, (d) O 1s, (e) C 1s and (f) N 1s. The KLL and LMM structure result from the excitation of Auger electron emission.....65

Figure 4. 10. (a) XRD patterns and (b) the zoom-in of the (003) and (006) peaks of NiFe-based multi-metal layered double hydroxides: NiFeCo, NiFeRu, NiFeCoRu, and NiFe/Au.....67

Figure 4. 11. Optical images of NiFe-based multi-metal LDHs nanosheets. Tyndall effect was visible

when irradiated with a laser beam.	67
Figure 4. 12 SEM and EDS patterns of NiFe-base LDHs: NiFeCo (a and b), NiFeRu (c and d), NiFeCoRu (e and f), and NiFe/Au (g and h). The inset in figures (b, d, f, and h) shows one selected area of NiFe-based LDHs (Scale bar 50 μm); atomic composition in each sample was calculated from five different areas.	68
Figure 4. 13 Tapping-mode AFM image and the corresponding height profiles of exfoliated monolayer NiFe-based multi-metal LDHs (a) NiFeCo, (b) NiFeRu, (c) NiFeCoRu and (d) NiFe/Au LDH nanosheets. It is marked with white line.	69
Figure 4. 14 Schematic illustrations of the fabrication process of work electrode based on lithography and e-beam deposition.	70
Figure 4. 15 OER performance. (a) Polarization curves of the NiFe LDHs monolayers, NiFe LDHs_0 powder, commercial RuO_2 , and gold electrode, sweep rate: 5 mV s^{-1} . (b) The corresponding Tafel slopes of the NiFe LDHs monolayers and NiFe LDHs_0 powders.	70
Figure 4. 16 Activity comparison of NiFe LDHs monolayer, NiFe LDHs_0 powder. The overpotential at current density of $j = 10 \text{ mA.cm}^{-2}$. The current was normalized to the areal activity at an overpotential of $\eta = 350 \text{ mV}$. Error bars represent the standard deviation of six measurements.	71
Figure 4. 17 Cyclic voltammetry (CV) curves of (a) NiFe LDHs monolayers and (b) NiFe LDHs_0 powder, scanned in the non-faradaic potential window at variable scan rates from 60 to 160 mV/s . The test potential range is 1.15-1.25 V vs RHE. The corresponding current density at 1.2 V vs RHE is used for calculating the C_{dl} value. (c) The calculated C_{dl} of NiFe LDHs monolayers and NiFe LDHs_0 powder catalysts. (d) Nyquist plots of NiFe LDHs monolayers and NiFe LDHs_0 powder at applied potentials 1.5V vs. RHE (overpotential at 270 mV).	72
Figure 4. 18 (a) Setup of a rotating disk electrode (RDE). (b) Polarization curves of the NiFe LDHs monolayers and commercial RuO_2 and glassy carbon disk electrode (GCE, 5 mm in diameter), sweep rate: 5 mV s^{-1} at the rotation rate of 1600 rpm. (c) The corresponding Tafel slopes of the NiFe LDHs monolayers on GCE.	73
Figure 4. 19 (a) Polarization curves and the corresponding Tafel slopes (inset) of the NiFeCo, NiFe Ru, NiFeCoRu, and NiFe/Au, sweep rate: 5 mV s^{-1} . (b) Activity comparison of NiFe LDHs and multi-metal NiFe-based LDHs monolayers. The current density normalized at $\eta = 300 \text{ mV}$	74
Figure 4. 20 (a) Nyquist plots of NiFe-base LDHs: NiFeCo, NiFeRu, NiFeCoRu, and NiFe/Au at applied potentials 1.5V vs. RHE (overpotential at 270 mV). (b) The calculated TOFs of NiFe LDHs monolayers, NiFeCo, NiFeRu, NiFeCoRu, and NiFe/Au at $\eta = 300 \text{ mV}$	75
Figure 4. 21 Schematics of the fabrication process and optical microscope images of the MoS_2 ML microelectrode array. (a) Schematic of the fabrication process for MoS_2 ML microelectrode array. Optical microscope image of the patterned (b) MoS_2 ML microelectrode, (c) MoS_2 ML/Cr/Au and (d) MoS_2 ML/Cr/Au/SU-8. AZ is the photoresist AZ5214e.	80
Figure 4. 22 (a) Side-section schematic of Cr/Pt (5 nm/50 nm) microelectrode. Optical microscope image of the patterned (b) Cr/Pt microelectrode, (c) microelectrode Cr/Pt with Cr/Au connection-electrode and (d) Cr/Pt with Cr/Au connection-electrode covered with SU-8 protection layer.	80
Figure 4. 23 Characterization of exfoliated MoS_2 ML. (A) Optic image of exfoliated MoS_2 ML on a silicon wafer (oxide layer 300nm). (B) Raman and (C) PL comparison of MoS_2 bulk and ML. XPS of MoS_2 ML: (D) Mo3d and (E) S2p. ML: monolayer.	81
Figure 4. 24 (a) Raman and (b) PL spectra of MoS_2 ML with increasing excitation laser power from 5.4 to 5400 $\text{W}\cdot\text{cm}^{-2}$ with a filter (from 0.1 to 100 %) at RT under ambient conditions. (c) Raman	

and (d) PL spectra of MoS ₂ bulk with increasing excitation laser power from 5.4 to 5400 kW·cm ⁻² with a filter (from 0.1 to 100 %) at RT under ambient conditions.	83
Figure 4. 25 Laser-induced thermal effects in MoS ₂ ML. Normalized (A) Raman and (B) PL spectra of MoS ₂ ML at increasing excitation laser power from 5.4 to 5400 kW·cm ⁻² with a filter (from 0.1 to 100 %) under ambient conditions. Zoomed-in details of B exciton in the MoS ₂ ML (insert of B, left) and schematic illustration of the band structure of MoS ₂ ML at the K points (insert of B, right). .	83
Figure 4. 26 The setup for evaluating the temperature-dependence of HER on an on-chip MoS ₂ ML. (a) IKA temperature heater and (b) on-chip MoS ₂ ML devices.	84
Figure 4. 27 Temperature-dependence of HER properties on MoS ₂ ML. (A) Schematic illustration and (B) Cross-section of the on-chip measurement setup. WE: working electrode, CE: counter electrode, and RE: reference electrode. (C) Polarization curves of MoS ₂ ML and corresponding (D) Tafel plots were obtained from the polarization curves over a temperature range from RT to 60 °C. (E) Tafel slope as a function of the temperature for lower temperature (Region I) and higher temperature (Region II). (F) TOF as a function of the overpotential. (G) Overpotential and TOF in lower temperature (Region I) and higher temperature (Region II) regions. Error bars represent standard deviations of four independent tests. (H) Nyquist plots for MoS ₂ ML at potentials -0.1 V vs. RHE (overpotential at 100 mV) from RT to 60 °C. (I) Overpotential (at 10 mA cm ⁻²) comparison with other reported on-chip MoS ₂ devices. a-g represent the on-chip MoS ₂ catalyst for SV-MoS ₂ ML, ^[198] MoS ₂ edges, ^[20] MoS ₂ nanosheets, ^[217] n-MoS ₂ , ^[23] MoS ₂ ML, ^[218] MoS ₂ ML, ^[276] and bowl-like MoS ₂ flake, ^[222] respectively.....	86
Figure 4. 28 LSV of Cr/Pt microelectrode over a temperature range from RT to 60 °C.	88
Figure 4. 29. Nyquist plots of MoS ₂ ML at applied potentials -100 mV vs. RHE under different temperatures from RT to 60 °C.	88
Figure 4. 30 Arrhenius plots of the exchange current densities on the MoS ₂ ML vs. temperature from RT (25) to 60 °C.....	89
Figure 4. 31 Characterization of exfoliated MoS ₂ ML on glass. (a) Raman and (b) PL spectra of the MoS ₂ ML on a glass substrate. (c) Polarization curves of the MoS ₂ ML on glass over a temperature range from RT to 60 °C.	90
Figure 4. 32 (a) Contact resistance of the MoS ₂ ML under different temperatures in H ₂ SO ₄ solution, which was obtained from EIS in Figure 4. 27H . (b) Polarization curves of the MoS ₂ ML under different temperatures with iR compensation. (c) Activity comparison of the MoS ₂ ML with/without iR compensation under different temperature. HER current density normalized to the areal activity, respectively, at the overpotential of 200 mV.	91
Figure 4. 33 Setup for evaluating the temperature-dependent HER of the MoS ₂ ML by using GC as a CE. (a) The temperature was controlled by IKA hot plates under the working electrode. (b) Optical image of the MoS ₂ ML microelectrode. Polarization curves of (c) the Pt film and (d) the MoS ₂ ML over a temperature range from RT to 60 °C by using glassy carbon (d= 3 mm) as a CE.	92
Figure 4. 34 HER Stability on MoS ₂ ML. Temperature-dependent current density curve for MoS ₂ ML catalyst at a constant overpotential of -200 mV versus RHE under different temperatures (orange curve). The schematic illustration of the set temperature with the IKA temperature controller (black line).	93
Figure 4. 35 HER Stability of the MoS ₂ ML. Temperature-dependent current density curve for the MoS ₂ ML catalyst at a constant overpotential of -200 mV versus RHE in an IKA constant temperature water bath at 25 °C and 30 °C.	94

Figure 4. 36 (a) Raman and (b) PL of MoS ₂ ML after stability testing.	95
---	----

Table 1 A summary of NiFe-based LDHs prepared through the hydrothermal method by using urea, HMT, and formamide as hydrolysis agents. M ₁ /M ₂ represents the ratio of divalent to trivalent metal ions. NH ₃ /M represents molar ratio of ammonium ion to metal ions.	29
---	----

Table 2 The recipe of NiFe-based LDHs.	56
--	----

Table 3. Comparison of this strategy as well as the reported LDHs exfoliated methods: exfoliated methods, equipment, time factors, and prices.	58
--	----

Table 4 Comparison of the on-chip HER performance of this report (at 60 °C) as well as other reported on-chip MoS ₂ results at RT: (overpotential (η) mV, at 10 mA cm ⁻²), Tafel slope (mV·dec ⁻¹)) and TOF (s ⁻¹).	88
---	----

List of Abbreviations

Abbreviations	Explanation
2D	Two-dimensional
AFM	Atomic force microscopy
CE	Counter electrode
CV	Cyclic voltammogram
C_{dl}	Electrochemical double layer capacitance
DI water	Distilled water
DMSO	Dimethyl sulfoxide
EDX	Energy-dispersive X-ray spectroscopy
FT-IR	Fourier transform infrared spectroscopy
HER/HOR	Hydrogen Evolution Reaction/Hydrogen oxidation reactions
HMT	Hexamethylenetetramine
LDH	Layered double hydroxides
LSV	Linear sweep voltammetry
MoS_2	Molybdenum disulfide
ML	Monolayer
OER/ORR	Oxygen evolution reaction/Oxygen reduction reactions

PL	Photoluminescence spectroscopy
RE	Reference electrode
RHE	Reversible hydrogen electrode
RT	Room temperature
RuO ₂	Ruthenium oxide
SAED	Selected area electron diffraction
SEM	Scanning electron microscopy
TEM	Transmission electron microscopy
TMDs	Transition metal dichalcogenides
TOF	turnover frequency
TRT	thermal release tape
WE	Working electrode
XRD	X-ray diffraction
XPS	X-ray photoelectron spectroscopy
η	Overpotential
ΔG	Activation energy

Bibliography

1. Zou, X. and Y. Zhang, *Noble metal-free hydrogen evolution catalysts for water splitting*. Chem. Soc. Rev., **2015**. 44(15), 5148-5180.
2. Suen, N.T., et al., *Electrocatalysis for the oxygen evolution reaction: recent development and future perspectives*. Chem. Soc. Rev., **2017**. 46(2), 337-365.
3. Seh, Z.W., et al., *Combining theory and experiment in electrocatalysis: Insights into materials design*. Science, **2017**. 355(6321), eaad4998.
4. Rossmeisl, J., et al., *Electrolysis of water on oxide surfaces*. J. Electroanal. Chem., **2007**. 607(1-2), 83-89.
5. Jiao, Y., et al., *Design of electrocatalysts for oxygen- and hydrogen-involving energy conversion reactions*. Chem. Soc. Rev., **2015**. 44(8), 2060-2086.
6. Nørskov, J.K., et al., *Trends in the exchange current for hydrogen evolution*. J. Electrochem. Soc., **2005**. 152(3), J23-J26.
7. Man, I.C., et al., *Universality in oxygen evolution electrocatalysis on oxide surfaces*. ChemCatChem, **2011**. 3(7), 1159-1165.
8. Roger, I., M.A. Shipman, and M.D. Symes, *Earth-abundant catalysts for electrochemical and photoelectrochemical water splitting*. Nat. Rev. Chem., **2017**. 1(1), 0003.
9. Novoselov, K.S., et al., *Electric field effect in atomically thin carbon films*. Science, **2004**. 306(5696), 666-669.
10. Fan, F.R., et al., *Emerging beyond-graphene elemental 2D materials for energy and catalysis applications*. Chem. Soc. Rev., **2021**. 50(19), 10983-11031.
11. Xiong, P., et al., *2D superlattices for efficient energy storage and conversion*. Adv. Mater., **2020**. 32(18), e1902654.
12. Jin, H., et al., *Emerging two-dimensional nanomaterials for electrocatalysis*. Chem. Rev., **2018**. 118(13), 6337-6408.
13. Chia, X.Y. and M. Pumera, *Characteristics and performance of two-dimensional materials for electrocatalysis*. Nat. Catal., **2018**. 1(12), 909-921.
14. Shifa, T.A., et al., *Heterostructures based on 2D materials: a versatile platform for efficient catalysis*. Adv. Mater., **2019**. 31(45), e1804828.
15. Deng, D.H., et al., *Catalysis with two-dimensional materials and their heterostructures*. Nat. Nanotechnol., **2016**. 11(3), 218-230.
16. Yang, S., et al., *Exfoliated graphitic carbon nitride nanosheets as efficient catalysts for hydrogen evolution under visible light*. Adv. Mater., **2013**. 25(17), 2452-2456.
17. Zhang, X., et al., *Solution-processed two-dimensional MoS₂ nanosheets: preparation, hybridization, and applications*. Angew. Chem. Int. Ed., **2016**. 55(31), 8816-8838.
18. Lukowski, M.A., et al., *Enhanced hydrogen evolution catalysis from chemically exfoliated metallic MoS₂ nanosheets*. J. Am. Chem. Soc., **2013**. 135(28), 10274-

- 10277.
19. Song, F. and X. Hu, *Exfoliation of layered double hydroxides for enhanced oxygen evolution catalysis*. Nat. Commun., **2014**. 5, 4477.
20. Voiry, D., et al., *The role of electronic coupling between substrate and 2D MoS₂ nanosheets in electrocatalytic production of hydrogen*. Nat. Mater., **2016**. 15(9), 1003-1009.
21. Zhou, Y., et al., *Revealing the contribution of individual factors to hydrogen evolution reaction catalytic activity*. Adv. Mater., **2018**. 30(18), e1706076.
22. Yu, Y., et al., *High phase-purity 1T'-MoS₂- and 1T'-MoSe₂-layered crystals*. Nat. Chem., **2018**. 10(6), 638-643.
23. He, Y., et al., *Self-gating in semiconductor electrocatalysis*. Nat. Mater., **2019**. 18(10), 1098-1104.
24. Zhang, J.Q., et al., *Single platinum atoms immobilized on an MXene as an efficient catalyst for the hydrogen evolution reaction*. Nat. Catal., **2018**. 1(12), 985-992.
25. Zhang, H., *Ultrathin two-dimensional nanomaterials*. ACS nano, **2015**. 9(10), 9451-9469.
26. Lin, Z., et al., *Solution-processable 2D semiconductors for high-performance large-area electronics*. Nature, **2018**. 562(7726), 254-258.
27. Kim, C., et al., *Performances of liquid - exfoliated transition metal dichalcogenides as hole injection layers in organic light - emitting diodes*. Adv. Funct. Mater., **2015**. 25(28), 4512-4519.
28. Li, H., et al., *Preparation and applications of mechanically exfoliated single-layer and multilayer MoS₂ and WSe₂ nanosheets*. Acc. Chem. Res., **2014**. 47(4), 1067-1075.
29. Nicolosi, V., et al., *Liquid exfoliation of layered materials*. Science, **2013**. 340(6139), 1226-1229.
30. Yin, S., et al., *A highly efficient oxygen evolution catalyst consisting of interconnected nickel-iron-layered double hydroxide and carbon nanodomains*. Adv. Mater., **2018**. 30(5), 1705106.
31. Chung, D.Y., et al., *Dynamic stability of active sites in hydr(oxy)oxides for the oxygen evolution reaction*. Nat. Energy, **2020**. 5(3), 222-230.
32. Friebe, D., et al., *Identification of highly active Fe sites in (Ni,Fe)OOH for electrocatalytic water splitting*. J. Am. Chem. Soc., **2015**. 137(3), 1305-1313.
33. Jia, Y., et al., *A heterostructure coupling of exfoliated Ni-Fe hydroxide nanosheet and defective graphene as a bifunctional electrocatalyst for overall water splitting*. Adv. Mater., **2017**. 29(17), 1700017.
34. Ping, J., et al., *Self-assembly of single-layer CoAl-layered double hydroxide nanosheets on 3D graphene network used as highly efficient electrocatalyst for oxygen evolution reaction*. Adv. Mater., **2016**. 28(35), 7640-7645.
35. Liu, Z., et al., *Synthesis, anion exchange, and delamination of Co-Al layered double hydroxide: assembly of the exfoliated nanosheet/polyanion composite films and magneto-optical studies*. J. Am. Chem. Soc., **2006**. 128(14), 4872-4880.

36. Ma, R.Z., et al., *Exfoliating layered double hydroxides in formamide: a method to obtain positively charged nanosheets*. J. Mater. Chem., **2006**. 16(39), 3809-3813.
37. Liang, H., et al., *Hydrothermal continuous flow synthesis and exfoliation of NiCo layered double hydroxide nanosheets for enhanced oxygen evolution catalysis*. Nano Lett., **2015**. 15(2), 1421-1427.
38. Long, X., et al., *A strongly coupled graphene and FeNi double hydroxide hybrid as an excellent electrocatalyst for the oxygen evolution reaction*. Angew. Chem. Int. Ed., **2014**. 53(29), 7584-7588.
39. Ma, W., et al., *A superlattice of alternately stacked Ni-Fe hydroxide nanosheets and graphene for efficient splitting of water*. ACS Nano, **2015**. 9(2), 1977-1984.
40. McAteer, D., et al., *Liquid exfoliated Co(OH)₂ nanosheets as low-cost, yet high-performance, catalysts for the oxygen evolution reaction*. Adv. Energy Mater., **2018**. 8(15), 1702965.
41. Zhou, P., et al., *Acid-etched layered double hydroxides with rich defects for enhancing the oxygen evolution reaction*. Chem. Commun., **2017**. 53(86), 11778-11781.
42. Wang, Y., et al., *Tuning surface electronic configuration of NiFe LDHs nanosheets by introducing cation vacancies (Fe or Ni) as highly efficient electrocatalysts for oxygen evolution reaction*. Small, **2018**. 14(17), e1800136.
43. Liu, R., et al., *Water-plasma-enabled exfoliation of ultrathin layered double hydroxide nanosheets with multivacancies for water oxidation*. Adv. Mater., **2017**. 29(30), 1701546.
44. Sun, H., et al., *Exfoliation of bimetallic (Ni, Co) carbonate hydroxide nanowires by Ar plasma for enhanced oxygen evolution*. Chem. Commun., **2020**. 56(6), 872-875.
45. Coleman, J.N., et al., *Two-dimensional nanosheets produced by liquid exfoliation of layered materials*. Science, **2011**. 331(6017), 568-571.
46. Jawaid, A., et al., *Mechanism for liquid phase exfoliation of MoS₂*. Chem. Mater., **2016**. 28(1), 337-348.
47. Li, Y., et al., *A general Lewis acidic etching route for preparing MXenes with enhanced electrochemical performance in non-aqueous electrolyte*. Nat. Mater., **2020**. 19(8), 894-899.
48. Miró, P., M. Audiffred, and T. Heine, *An atlas of two-dimensional materials*. Chem. Soc. Rev., **2014**. 43(18), 6537-6554.
49. Ben, J., et al., *2D III-nitride materials: properties, growth, and applications*. Adv. Mater., **2021**. 33(27), 2006761.
50. K. S. Novoselov, A.M., A. Carvalho, A. H. Castro Neto*, *2D materials and van der Waals heterostructures*. Science, **2016**. 353, 461.
51. Geim, A.K. and I.V. Grigorieva, *Van der Waals heterostructures*. Nature, **2013**. 499(7459), 419-425.
52. Zhou, J., et al., *A library of atomically thin metal chalcogenides*. Nature, **2018**. 556(7701), 355-359.
53. Pumera, M. and Z. Sofer, *2D monoelemental arsenene, antimonene, and*

- bismuthene: beyond black phosphorus*. Adv. Mater., **2017**. 29(21), 1605299.
54. Yankowitz, M., et al., *van der Waals heterostructures combining graphene and hexagonal boron nitride*. Nat. Rev. Phys., **2019**. 1(2), 112-125.
 55. Wang, Q.H., et al., *Electronics and optoelectronics of two-dimensional transition metal dichalcogenides*. Nat. Nanotechnol., **2012**. 7(11), 699-712.
 56. Rao, T., et al., *Phase transitions and water splitting applications of 2D transition metal dichalcogenides and metal phosphorous trichalcogenides*. Adv. Sci., **2021**. 8(10), 2002284.
 57. Klein, D.R., et al., *Probing magnetism in 2D van der Waals crystalline insulators via electron tunneling*. Science, **2018**. 360(6394), 1218-1222.
 58. Taboada-Gutiérrez, J., et al., *Broad spectral tuning of ultra-low-loss polaritons in a van der Waals crystal by intercalation*. Nat. Mater., **2020**.
 59. Abedini Dereshgi, S., et al., *Lithography-free IR polarization converters via orthogonal in-plane phonons in α -MoO₃ flakes*. Nat. Commun., **2020**. 11(1), 5771.
 60. Blancon, J.-C., et al., *Semiconductor physics of organic-inorganic 2D halide perovskites*. Nat. Nanotechnol., **2020**. 15(12), 969-985.
 61. Bergeron, H., D. Lebedev, and M.C. Hersam, *Polymorphism in post-dichalcogenide two-dimensional materials*. Chem. Rev., **2021**. 121(4), 2713-2775.
 62. Zou, Y.C., et al., *Ion exchange in atomically thin clays and micas*. Nat. Mater., **2021**. 20(12), 1677-1682.
 63. Long, X., et al., *Transition metal based layered double hydroxides tailored for energy conversion and storage*. Mater. Today, **2016**. 19(4), 213-226.
 64. VahidMohammadi, A., J. Rosen, and Y. Gogotsi, *The world of two-dimensional carbides and nitrides (MXenes)*. Science, **2021**. 372(6547), eabf1581.
 65. Anasori, B., M.R. Lukatskaya, and Y. Gogotsi, *2D metal carbides and nitrides (MXenes) for energy storage*. Nat. Rev. Mater., **2017**. 2(2), 16098.
 66. Zhang, X., et al., *Two-dimensional MoS₂-enabled flexible rectenna for Wi-Fi-band wireless energy harvesting*. Nature, **2019**. 566(7744), 368-372.
 67. Eda, G., G. Fanchini, and M. Chhowalla, *Large-area ultrathin films of reduced graphene oxide as a transparent and flexible electronic material*. Nat. Nanotechnol., **2008**. 3(5), 270-274.
 68. Acerce, M., D. Voiry, and M. Chhowalla, *Metallic 1T phase MoS₂ nanosheets as supercapacitor electrode materials*. Nat. Nanotechnol., **2015**. 10, 313.
 69. Kibsgaard, J., et al., *Engineering the surface structure of MoS₂ to preferentially expose active edge sites for electrocatalysis*. Nat. Mater., **2012**. 11(11), 963-969.
 70. Novoselov, K.S., et al., *Two-dimensional atomic crystals*. Proc. Natl. Acad. Sci. U.S.A., **2005**. 102(30), 10451-10453.
 71. Lee, C., et al., *Frictional characteristics of atomically thin sheets*. Science, **2010**. 328(5974), 76-80.
 72. Shim, J., et al., *Controlled crack propagation for atomic precision handling of wafer-scale two-dimensional materials*. Science, **2018**. 362(6415), 665-670.
 73. Liu, F., et al., *Disassembling 2D van der Waals crystals into macroscopic*

- monolayers and reassembling into artificial lattices*. Science, **2020**. 367(6480), 903-906.
74. Magda, G.Z., et al., *Exfoliation of large-area transition metal chalcogenide single layers*. Sci. Rep., **2015**. 5(1), 14714.
75. Wu, F., et al., *Formation of coherent 1H-1T heterostructures in single-layer MoS₂ on Au(111)*. ACS Nano, **2020**. 14(12), 16939-16950.
76. Desai, S.B., et al., *Gold-mediated exfoliation of ultralarge optoelectronically-perfect monolayers*. Adv. Mater., **2016**. 28(21), 4053-4058.
77. Velický, M., et al., *The intricate love affairs between MoS₂ and metallic substrates*. Adv. Mater. Interfaces, **2020**. 7(23), 2001324.
78. Velicky, M., et al., *Mechanism of gold-assisted exfoliation of centimeter-sized transition-metal dichalcogenide monolayers*. ACS Nano, **2018**. 12(10), 10463-10472.
79. Huang, Y., et al., *Universal mechanical exfoliation of large-area 2D crystals*. Nat. Commun., **2020**. 11(1), 2453.
80. Hai, X., et al., *Engineering the edges of MoS₂ (WS₂) crystals for direct exfoliation into monolayers in polar micromolecular solvents*. J. Am. Chem. Soc., **2016**. 138(45), 14962-14969.
81. Li, M.Y., et al., *Heterostructures based on two-dimensional layered materials and their potential applications*. Mater. Today, **2016**. 19(6), 322-335.
82. Kelly, A.G., et al., *All-printed thin-film transistors from networks of liquid-exfoliated nanosheets*. Science, **2017**. 356(6333), 69-73.
83. Fan, X., et al., *Controlled exfoliation of MoS₂ crystals into trilayer nanosheets*. J. Am. Chem. Soc., **2016**. 138(15), 5143-5149.
84. Shi, J., et al., *Controllable growth and transfer of monolayer MoS₂ on Au foils and its potential application in hydrogen evolution reaction*. ACS Nano, **2014**. 8(10), 10196-10204.
85. Liu, L., et al., *Phase-selective synthesis of 1T' MoS₂ monolayers and heterophase bilayers*. Nat. Mater., **2018**. 17(12), 1108-1114.
86. Amani, M., et al., *High luminescence efficiency in MoS₂ grown by chemical vapor deposition*. ACS Nano, **2016**. 10(7), 6535-6541.
87. Cheng, F., et al., *Interface engineering of Au(111) for the growth of 1T'-MoSe₂*. ACS Nano, **2019**. 13(2), 2316-2323.
88. Fu, D., et al., *Molecular beam epitaxy of highly crystalline monolayer molybdenum disulfide on hexagonal boron nitride*. J. Am. Chem. Soc., **2017**. 139(27), 9392-9400.
89. Yin, Y., et al., *Synergistic phase and disorder engineering in 1T-MoSe₂ nanosheets for enhanced hydrogen-evolution reaction*. Adv. Mater., **2017**. 29(28), 1700311.
90. Xie, J., et al., *Controllable disorder engineering in oxygen-incorporated MoS₂ ultrathin nanosheets for efficient hydrogen evolution*. J. Am. Chem. Soc., **2013**. 135(47), 17881-17888.
91. Xie, J., et al., *Defect-rich MoS₂ ultrathin nanosheets with additional active edge sites for enhanced electrocatalytic hydrogen evolution*. Adv. Mater., **2013**.

- 25(40), 5807-5813.
92. Tan, C., et al., *Recent advances in ultrathin two-dimensional nanomaterials*. Chem. Rev., **2017**. 117(9), 6225-6331.
 93. Liu, G., et al., *MoS₂ monolayer catalyst doped with isolated Co atoms for the hydrodeoxygenation reaction*. Nat. Chem., **2017**. 9(8), 810-816.
 94. Peto, J., et al., *Spontaneous doping of the basal plane of MoS₂ single layers through oxygen substitution under ambient conditions*. Nat. Chem., **2018**. 10(12), 1246-1251.
 95. Zhang, X., et al., *Phonon and Raman scattering of two-dimensional transition metal dichalcogenides from monolayer, multilayer to bulk material*. Chem. Soc. Rev., **2015**. 44(9), 2757-2785.
 96. Splendiani, A., et al., *Emerging photoluminescence in monolayer MoS₂*. Nano Lett., **2010**. 10(4), 1271-1275.
 97. Mak, K.F., et al., *Atomically thin MoS₂: a new direct-gap semiconductor*. Phys. Rev. Lett., **2010**. 105(13), 136805.
 98. Liu, Y., et al., *Promises and prospects of two-dimensional transistors*. Nature, **2021**. 591(7848), 43-53.
 99. Mak, K.F. and J. Shan, *Photonics and optoelectronics of 2D semiconductor transition metal dichalcogenides*. Nat. Photonics, **2016**. 10(4), 216-226.
 100. Cheng, R., et al., *Few-layer molybdenum disulfide transistors and circuits for high-speed flexible electronics*. Nat. Commun., **2014**. 5.
 101. Lopez-Sanchez, O., et al., *Ultrasensitive photodetectors based on monolayer MoS₂*. Nat. Nanotechnol., **2013**. 8(7), 497-501.
 102. Lembke, D., S. Bertolazzi, and A. Kis, *Single-layer MoS₂ electronics*. Acc. Chem. Res., **2015**. 48(1), 100-110.
 103. Tang, L., et al., *Confinement catalysis with 2D materials for energy conversion*. Adv. Mater., **2019**. 0(0), 1901996.
 104. Luan, C., et al., *Structure effects of 2D materials on alpha-nickel hydroxide for oxygen evolution reaction*. ACS Nano, **2018**. 12(4), 3875-3885.
 105. Chu, S. and A. Majumdar, *Opportunities and challenges for a sustainable energy future*. Nature, **2012**. 488(7411), 294-303.
 106. Benck, J.D., et al., *Catalyzing the hydrogen evolution reaction (HER) with molybdenum sulfide nanomaterials*. ACS Catal., **2014**. 4(11), 3957-3971.
 107. Browne, M.P., Z. Sofer, and M. Pumera, *Layered and two dimensional metal oxides for electrochemical energy conversion*. Energy Environ. Sci., **2019**. 12(1), 41-58.
 108. Wang, F., et al., *Recent advances in transition-metal dichalcogenide based nanomaterials for water splitting*. Nanoscale, **2015**. 7(47), 19764-19788.
 109. Liang, Y., et al., *Strongly coupled inorganic/nanocarbon hybrid materials for advanced electrocatalysis*. J. Am. Chem. Soc., **2013**. 135(6), 2013-2036.
 110. Liu, X.-W., W.-W. Li, and H.-Q. Yu, *Cathodic catalysts in bioelectrochemical systems for energy recovery from wastewater*. Chem. Soc. Rev., **2014**. 43(22), 7718-7745.
 111. Chao, T., et al., *Atomically dispersed pt on screw-like Pd/Au core-shell nanowires*

- for enhanced electrocatalysis*. Chem. Eur. J., **2020**. 26(18), 4019-4024.
112. Zhang, L., et al., *Atomic layer deposited Pt-Ru dual-metal dimers and identifying their active sites for hydrogen evolution reaction*. Nat. Commun., **2019**. 10(1), 4936.
113. Seitz, L.C., et al., *A highly active and stable IrO_x/SrIrO₃ catalyst for the oxygen evolution reaction*. Science, **2016**. 353(6303), 1011-1014.
114. Dotan, H., et al., *Decoupled hydrogen and oxygen evolution by a two-step electrochemical–chemical cycle for efficient overall water splitting*. Nat. Energy, **2019**. 4(9), 786-795.
115. Hunter, B.M., H.B. Gray, and A.M. Muller, *Earth-abundant heterogeneous water oxidation catalysts*. Chem. Rev., **2016**. 116(22), 14120-14136.
116. Fang, M., et al., *Hierarchical nanostructures: design for sustainable water splitting*. Adv. Energy Mater., **2017**. 7(23), 1700559.
117. Staszak-Jirkovský, J., et al., *Design of active and stable Co-Mo-S_x chalcogels as pH-universal catalysts for the hydrogen evolution reaction*. Nat. Mater., **2015**. 15, 197.
118. Ding, Q., et al., *Efficient electrocatalytic and photoelectrochemical hydrogen generation using MoS₂ and related compounds*. Chem, **2016**. 1(5), 699-726.
119. Jaramillo, T.F., et al., *Identification of active edge sites for electrochemical H₂ evolution from MoS₂ nanocatalysts*. Science, **2007**. 317(5834), 100-102.
120. Hinnemann, B., et al., *Biomimetic hydrogen evolution: MoS₂ nanoparticles as catalyst for hydrogen evolution*. J. Am. Chem. Soc., **2005**. 127(15), 5308-5309.
121. Hu, K., et al., *Catalytic activity of graphene-covered non-noble metals governed by proton penetration in electrochemical hydrogen evolution reaction*. Nat. Commun., **2021**. 12(1), 203.
122. Zhao, D.M., et al., *Boron-doped nitrogen-deficient carbon nitride-based Z-scheme heterostructures for photocatalytic overall water splitting*. Nat. Energy, **2021**. 6(4), 388-397.
123. Ong, W.J., et al., *Graphitic carbon nitride (g-C₃N₄)-based photocatalysts for artificial photosynthesis and environmental remediation: Are we a step closer to achieving sustainability?* Chem. Rev., **2016**. 116(12), 7159-7329.
124. Liu, J., et al., *Metal-free efficient photocatalyst for stable visible water splitting via a two-electron pathway*. Science, **2015**. 347(6225), 970-974.
125. Liu, H., et al., *Conductive boron nitride as promising catalyst support for the oxygen evolution reaction*. Adv. Energy Mater., **2020**. 10(25), 1902521.
126. Wang, X., et al., *Rapid activation of platinum with black phosphorus for efficient hydrogen evolution*. Angew. Chem. Int. Ed., **2019**. 58(52), 19060-19066.
127. Li, X., et al., *Adaptive bifunctional electrocatalyst of amorphous CoFe oxide @ 2D black phosphorus for overall water splitting*. Angew. Chem. Int. Ed., **2020**. 59(47), 21106-21113.
128. Di, J., et al., *Ultrathin two-dimensional materials for photo- and electrocatalytic hydrogen evolution*. Mater. Today, **2018**. 21(7), 749-770.
129. Zhang, B., et al., *Homogeneously dispersed multimetal oxygen-evolving catalysts*. Science, **2016**. 352(6283), 333-337.

130. Lim, K.R.G., et al., *Rational design of two-dimensional transition metal carbide/nitride (MXene) hybrids and nanocomposites for catalytic energy storage and conversion*. ACS Nano, **2020**. 14(9), 10834-10864.
131. Cui, C., et al., *Ultrastable MXene@Pt/SWCNTs' nanocatalysts for hydrogen evolution reaction*. Adv. Funct. Mater., **2020**. 30(47), 2000693.
132. Wan, Y., et al., *A simple molecular design strategy for two-dimensional covalent organic framework capable of visible-light-driven water splitting*. J. Am. Chem. Soc., **2020**. 142(9), 4508-4516.
133. Li, Y., et al., *New synthetic strategies toward covalent organic frameworks*. Chem. Soc. Rev., **2020**. 49(10), 2852-2868.
134. Dhakshinamoorthy, A., A.M. Asiri, and H. Garcia, *2D metal-organic frameworks as multifunctional materials in heterogeneous catalysis and electro/photocatalysis*. Adv. Mater., **2019**. 31(41), e1900617.
135. Fan, G., et al., *Catalytic applications of layered double hydroxides: recent advances and perspectives*. Chem. Soc. Rev., **2014**. 43(20), 7040-7066.
136. Wang, R., et al., *Defect engineering in metastable phases of transition-metal dichalcogenides for electrochemical applications*. Chem Asian J, **2020**. 15(23), 3961-3972.
137. Song, J., et al., *A review on fundamentals for designing oxygen evolution electrocatalysts*. Chem. Soc. Rev., **2020**. 49(7), 2196-2214.
138. McCrory, C.C., et al., *Benchmarking heterogeneous electrocatalysts for the oxygen evolution reaction*. J. Am. Chem. Soc., **2013**. 135(45), 16977-16987.
139. Dau, H., et al., *The mechanism of water oxidation: from electrolysis via homogeneous to biological catalysis*. ChemCatchem, **2010**. 2(7), 724-761.
140. Medford, A.J., et al., *From the Sabatier principle to a predictive theory of transition-metal heterogeneous catalysis*. J. Catal., **2015**. 328, 36-42.
141. Zhang, B., et al., *High-valence metals improve oxygen evolution reaction performance by modulating 3d metal oxidation cycle energetics*. Nat. Catal., **2020**. 3(12), 985-992.
142. Reier, T., et al., *Electrocatalytic oxygen evolution reaction in acidic environments - reaction mechanisms and catalysts*. Adv. Energy Mater., **2017**. 7(1), 1601275.
143. Zhu, K., X. Zhu, and W. Yang, *Application of in situ techniques for the characterization of NiFe-based oxygen evolution reaction (OER) electrocatalysts*. Angew. Chem. Int. Ed., **2019**. 58(5), 1252-1265.
144. Mesa, C.A., et al., *Multihole water oxidation catalysis on haematite photoanodes revealed by operando spectroelectrochemistry and DFT*. Nat. Chem., **2020**. 12(1), 82-89.
145. Zhao, M.Q., et al., *Hierarchical nanocomposites derived from nanocarbons and layered double hydroxides - properties, synthesis, and applications*. Adv. Funct. Mater., **2012**. 22(4), 675-694.
146. Zhao, Y.F., et al., *Layered double hydroxide nanostructured photocatalysts for renewable energy production*. Adv. Energy Mater., **2016**. 6(6), 1501974.
147. Xu, M. and M. Wei, *Layered double hydroxide-based catalysts: recent advances*

- in preparation, structure, and applications*. Adv. Funct. Mater., **2018**. 28(47), 1802943.
148. Dionigi, F. and P. Strasser, *NiFe-based (oxy)hydroxide catalysts for oxygen evolution reaction in non-acidic electrolytes*. Adv. Energy Mater., **2016**. 6(23), 1600621.
149. Han, L., S. Dong, and E. Wang, *Transition-metal (Co, Ni, and Fe)-based electrocatalysts for the water oxidation reaction*. Adv. Mater., **2016**. 28(42), 9266-9291.
150. Lu, X., et al., *2D layered double hydroxide nanosheets and their derivatives toward efficient oxygen evolution reaction*. Nanomicro Lett., **2020**. 12(1), 86.
151. Lv, L., et al., *2D layered double hydroxides for oxygen evolution reaction: from fundamental design to application*. Adv. Energy Mater., **2019**. 9(17), 1803358.
152. Gong, M., et al., *An advanced Ni-Fe layered double hydroxide electrocatalyst for water oxidation*. J. Am. Chem. Soc., **2013**. 135(23), 8452-8455.
153. Bajdich, M., et al., *Theoretical investigation of the activity of cobalt oxides for the electrochemical oxidation of water*. J. Am. Chem. Soc., **2013**. 135(36), 13521-13530.
154. Dou, Y.H., et al., *How cobalt and iron doping determine the oxygen evolution electrocatalytic activity of NiOOH*. Cell Reports Physical Science, **2020**. 1(6), 100077.
155. Yu, L., et al., *Hierarchical hollow nanoprisms based on ultrathin Ni-Fe layered double hydroxide nanosheets with enhanced electrocatalytic activity towards oxygen evolution*. Angew. Chem. Int. Ed., **2018**. 57(1), 172-176.
156. Zhao, Y.F., et al., *Sub-3 nm ultrafine monolayer layered double hydroxide nanosheets for electrochemical water oxidation*. Adv. Energy Mater., **2018**. 8(18), 1703585.
157. Huang, Z.-F., et al., *Chemical and structural origin of lattice oxygen oxidation in Co-Zn oxyhydroxide oxygen evolution electrocatalysts*. Nat. Energy, **2019**. 4(4), 329-338.
158. Yao, Y.C., et al., *Engineering the electronic structure of single atom Ru sites via compressive strain boosts acidic water oxidation electrocatalysis*. Nat. Catal., **2019**. 2(4), 304-313.
159. Zhang, J., et al., *Single-atom Au/NiFe layered double hydroxide electrocatalyst: probing the origin of activity for oxygen evolution reaction*. J. Am. Chem. Soc., **2018**. 140(11), 3876-3879.
160. Chen, G., et al., *Accelerated hydrogen evolution kinetics on NiFe-layered double hydroxide electrocatalysts by tailoring water dissociation active sites*. Adv. Mater., **2018**. 30(10), 1706279.
161. Ng, J.W.D., et al., *Gold-supported cerium-doped NiO_x catalysts for water oxidation*. Nat. Energy, **2016**. 1(5), 16053.
162. Cao, L., et al., *Dynamic oxygen adsorption on single-atomic Ruthenium catalyst with high performance for acidic oxygen evolution reaction*. Nat. Commun., **2019**. 10(1), 4849.
163. Lu, X. and C. Zhao, *Electrodeposition of hierarchically structured three-*

- dimensional nickel-iron electrodes for efficient oxygen evolution at high current densities.* Nat. Commun., **2015**. 6, 6616.
164. Li, Y.B. and C. Zhao, *Enhancing water oxidation catalysis on a synergistic phosphorylated NiFe hydroxide by adjusting catalyst wettability.* ACS Catal., **2017**. 7(4), 2535-2541.
 165. Oliver-Tolentino, M.A., et al., *An approach to understanding the electrocatalytic activity enhancement by superexchange interaction toward OER in alkaline media of Ni-Fe LDH.* J. Phys. Chem. C, **2014**. 118(39), 22432-22438.
 166. Zhou, Y., et al., *Exceptional performance of hierarchical Ni-Fe (hydr)oxide@NiCu electrocatalysts for water splitting.* Adv. Mater., **2019**. 31(8), e1806769.
 167. Zhang, H.J., et al., *Bifunctional heterostructure assembly of NiFe LDH nanosheets on NiCoP nanowires for highly efficient and stable overall water splitting.* Adv. Funct. Mater., **2018**. 28(14), 1706847.
 168. Qiu, Z., et al., *Direct observation of active catalyst surface phases and the effect of dynamic self-optimization in NiFe-layered double hydroxides for alkaline water splitting.* Energy Environ. Sci., **2019**. 12(2), 572-581.
 169. Luo, J., et al., *Water photolysis at 12.3% efficiency via perovskite photovoltaics and Earth-abundant catalysts.* Science, **2014**. 345(6204), 1593-1596.
 170. Dresp, S., et al., *Direct electrolytic splitting of seawater: activity, selectivity, degradation, and recovery studied from the molecular catalyst structure to the electrolyzer cell level.* Adv. Energy Mater., **2018**. 8(22), 1800338.
 171. Dresp, S., et al., *An efficient bifunctional two-component catalyst for oxygen reduction and oxygen evolution in reversible fuel cells, electrolyzers and rechargeable air electrodes.* Energy Environ. Sci., **2016**. 9(6), 2020-2024.
 172. Li, P.S., et al., *Tuning electronic structure of NiFe layered double hydroxides with vanadium doping toward high efficient electrocatalytic water oxidation.* Adv. Energy Mater., **2018**. 8(15), 1703341.
 173. Zhang, X., et al., *A simple synthetic strategy toward defect - rich porous monolayer NiFe - layered double hydroxide nanosheets for efficient electrocatalytic water oxidation.* Adv. Energy Mater., **2019**. 9(24), 1900881.
 174. Hunter, B.M., et al., *Effect of interlayer anions on [NiFe]-LDH nanosheet water oxidation activity.* Energy Environ. Sci., **2016**. 9(5), 1734-1743.
 175. Zhou, D., et al., *Activating basal plane in NiFe layered double hydroxide by Mn²⁺ doping for efficient and durable oxygen evolution reaction.* Nanoscale Horiz., **2018**. 3(5), 532-537.
 176. Jiang, J., et al., *Atomic-level insight into super-efficient electrocatalytic oxygen evolution on iron and vanadium co-doped nickel (oxy)hydroxide.* Nat. Commun., **2018**. 9(1), 2885.
 177. Zhu, W., et al., *Au promoted nickel-iron layered double hydroxide nanoarrays: a modular catalyst enabling high-performance oxygen evolution.* ACS Appl. Mater. Interfaces, **2017**. 9(23), 19807-19814.
 178. Wang, X., et al., *CeO_x-decorated NiFe-layered double hydroxide for efficient alkaline hydrogen evolution by oxygen vacancy engineering.* ACS Appl. Mater.

- Interfaces, **2018**. 10(41), 35145-35153.
179. Zhou, Q., et al., *Active-site-enriched iron-doped nickel/cobalt hydroxide nanosheets for enhanced oxygen evolution reaction*. ACS Catal., **2018**. 8(6), 5382–5390.
180. Zhu, X., et al., *Dual-sized NiFe layered double hydroxides in situ grown on oxygen-decorated self-dispersal nanocarbon as enhanced water oxidation catalysts*. J. Mater. Chem. A, **2015**. 3(48), 24540-24546.
181. Liu, W.-J., et al., *Electrochemical oxidation of 5-hydroxymethylfurfural with NiFe layered double hydroxide (LDH) nanosheet catalysts*. ACS Catal., **2018**. 8(6), 5533-5541.
182. Zhang, F.-S., et al., *Extraction of nickel from NiFe-LDH into Ni₂P@NiFe hydroxide as a bifunctional electrocatalyst for efficient overall water splitting*. Chem. Sci., **2018**. 9(5), 1375-1384.
183. Yang, Y., et al., *Highly active trimetallic NiFeCr layered double hydroxide electrocatalysts for oxygen evolution reaction*. Adv. Energy Mater., **2018**. 8(15), 1703189.
184. Xie, J., et al., *Intralayered ostwald ripening to ultrathin nanomesh catalyst with robust oxygen-evolving performance*. Adv. Mater., **2017**. 29(10), 1604765.
185. Xie, J., et al., *Sub-3 nm pores in two-dimensional nanomesh promoting the generation of electroactive phase for robust water oxidation*. Nano Energy, **2018**. 53, 74-82.
186. Liu, T., et al., *Interfacial electron transfer of Ni₂P-NiP₂ polymorphs inducing enhanced electrochemical properties*. Adv. Mater., **2018**. 30(46), e1803590.
187. Ma, W., et al., *Development of efficient electrocatalysts via molecular hybridization of NiMn layered double hydroxide nanosheets and graphene*. Nanoscale, **2016**. 8(19), 10425-10432.
188. Lee, S., L. Bai, and X. Hu, *Deciphering iron-dependent activity in oxygen evolution catalyzed by nickel-iron layered double hydroxide*. Angew. Chem. Int. Ed., **2020**. 59(21), 8072-8077.
189. Giovannetti, G., et al., *Doping graphene with metal contacts*. Phys. Rev. Lett., **2008**. 101(2), 026803.
190. Liu, H., Y. Liu, and D. Zhu, *Chemical doping of graphene*. J. Mater. Chem., **2011**. 21(10), 3335-3345.
191. Wehling, T.O., et al., *Molecular doping of graphene*. Nano Lett., **2008**. 8(1), 173-177.
192. Sakintuna, B., F. Lamari-Darkrim, and M. Hirscher, *Metal hydride materials for solid hydrogen storage: a review*. Int. J. Hydrogen Energy, **2007**. 32(9), 1121-1140.
193. Shinagawa, T., A.T. Garcia-Esparza, and K. Takanabe, *Insight on Tafel slopes from a microkinetic analysis of aqueous electrocatalysis for energy conversion*. Sci Rep, **2015**. 5, 13801.
194. Skúlason, E., et al., *Modeling the electrochemical hydrogen oxidation and evolution reactions on the basis of density functional theory calculations*. J. Phys. Chem. C, **2010**. 114(42), 18182-18197.

195. Laursen, A.B., et al., *Electrochemical hydrogen evolution: Sabatier's principle and the volcano plot*. J. Chem. Educ., **2012**. 89(12), 1595-1599.
196. Kibler, L.A., *Hydrogen electrocatalysis*. ChemPhysChem, **2006**. 7(5), 985-991.
197. Yang, J., et al., *Ultrahigh-current-density niobium disulfide catalysts for hydrogen evolution*. Nat. Mater., **2019**. 18(12), 1309-1314.
198. Li, H., et al., *Activating and optimizing MoS₂ basal planes for hydrogen evolution through the formation of strained sulphur vacancies*. Nat. Mater., **2016**. 15(1), 48-53.
199. Li, Y., et al., *MoS₂ nanoparticles grown on graphene: an advanced catalyst for the hydrogen evolution reaction*. J. Am. Chem. Soc., **2011**. 133(19), 7296-7299.
200. Tsai, C., F. Abild-Pedersen, and J.K. Nørskov, *Tuning the MoS₂ edge-site activity for hydrogen evolution via support interactions*. Nano Lett., **2014**. 14(3), 1381-1387.
201. Tsai, C., et al., *Theoretical insights into the hydrogen evolution activity of layered transition metal dichalcogenides*. Surf. Sci., **2015**. 640, 133-140.
202. Voiry, D., et al., *Conducting MoS₂ nanosheets as catalysts for hydrogen evolution reaction*. Nano Lett., **2013**. 13(12), 6222-6227.
203. Wang, H., et al., *Electrochemical tuning of vertically aligned MoS₂ nanofilms and its application in improving hydrogen evolution reaction*. Proc. Natl. Acad. Sci. U.S.A., **2013**. 110(49), 19701-19706.
204. Yang, J., et al., *Single atomic vacancy catalysis*. ACS Nano, **2019**. 13(9), 9958-9964.
205. Gupta, U. and C.N.R. Rao, *Hydrogen generation by water splitting using MoS₂ and other transition metal dichalcogenides*. Nano Energy, **2017**. 41, 49-65.
206. He, Z.L. and W.X. Que, *Molybdenum disulfide nanomaterials: structures, properties, synthesis and recent progress on hydrogen evolution reaction*. Appl. Mater. Today, **2016**. 3, 23-56.
207. Yan, Y., et al., *Recent development of molybdenum sulfides as advanced electrocatalysts for hydrogen evolution reaction*. ACS Catal., **2014**. 4(6), 1693-1705.
208. Lu, Q., et al., *2D transition-metal-dichalcogenide-nanosheet-based composites for photocatalytic and electrocatalytic hydrogen evolution reactions*. Adv. Mater., **2016**. 28(10), 1917-1933.
209. Zhao, G.Q., et al., *Heterostructures for electrochemical hydrogen evolution reaction: a review*. Adv. Funct. Mater., **2018**. 28(43), 1803291.
210. Chen, Y.X., et al., *Emerging two-dimensional nanomaterials for electrochemical hydrogen evolution*. J. Mater. Chem. A, **2017**. 5(18), 8187-8208.
211. Zhu, C.R., et al., *TMD-based highly efficient electrocatalysts developed by combined computational and experimental approaches*. Chem. Soc. Rev., **2018**. 47(12), 4332-4356.
212. Yang, L., et al., *Sustainable fuel production from ambient moisture via ferroelectrically driven MoS₂ nanosheets*. Adv. Mater., **2020**. 32(25), 2000971.
213. Wang, J., et al., *Field effect enhanced hydrogen evolution reaction of MoS₂ nanosheets*. Adv. Mater., **2017**. 29(7), 1604464.

214. Yan, M., et al., *Field-effect tuned adsorption dynamics of VSe₂ nanosheets for enhanced hydrogen evolution reaction*. Nano Lett., **2017**. 17(7), 4109-4115.
215. Zhang, J., et al., *Unveiling active sites for the hydrogen evolution reaction on monolayer MoS₂*. Adv. Mater., **2017**. 29(42), 1701955.
216. Wang, Z.G., et al., *Controllable etching of MoS₂ basal planes for enhanced hydrogen evolution through the formation of active edge sites*. Nano Energy, **2018**. 49, 634-643.
217. Yan, M.Y., et al., *Electric field and photoelectrical effect bi-enhanced hydrogen evolution reaction*. Nano Res., **2018**. 11(6), 3205-3212.
218. Liu, X., et al., *The critical role of electrolyte gating on the hydrogen evolution performance of monolayer MoS₂*. Nano Lett., **2019**. 19(11), 8118-8124.
219. Nam, G.H., et al., *In-plane anisotropic properties of 1T'-MoS₂ layers*. Adv. Mater., **2019**. 31(21), e1807764.
220. Wang, Y., et al., *Field effect modulation of electrocatalytic hydrogen evolution at back-gated two-dimensional MoS₂ electrodes*. Nano Lett., **2019**. 19(9), 6118-6123.
221. He, Y., et al., *Engineering grain boundaries at the 2D limit for the hydrogen evolution reaction*. Nat. Commun., **2020**. 11(1), 57.
222. Zhou, W., et al., *Magnetic enhancement for hydrogen evolution reaction on ferromagnetic MoS₂ catalyst*. Nano Lett., **2020**. 20(4), 2923-2930.
223. Takahashi, Y., et al., *High-resolution electrochemical mapping of the hydrogen evolution reaction on transition-metal dichalcogenide nanosheets*. Angew. Chem. Int. Ed., **2020**. 59(9), 3601-3608.
224. Yang, H., et al., *On-chip electrocatalytic microdevice: an emerging platform for expanding the insight into electrochemical processes*. Chem. Soc. Rev., **2020**. 49(10), 2916-2936.
225. Borukhin, S. and B. Pokroy, *Formation and elimination of surface nanodefects on ultraflat metal surfaces produced by template stripping*. Langmuir, **2011**. 27(22), 13415-13419.
226. Yang, R., et al., *Synergistic coupling of CoFe-LDH arrays with NiFe-LDH nanosheet for highly efficient overall water splitting in alkaline media*. Appl. Catal. B, **2019**. 253, 131-139.
227. Xu, X., et al., *High-efficiency CO₂ separation using hybrid LDH-polymer membranes*. Nat. Commun., **2021**. 12(1), 3069.
228. Zhang, C.X., et al., *Rh₂S₃/N-doped carbon hybrids as pH-universal bifunctional electrocatalysts for energy-saving hydrogen evolution*. Small Methods, **2020**. 4(9), 2000208.
229. Niu, S.Q., et al., *How to reliably report the overpotential of an electrocatalyst*. ACS Energy Lett., **2020**. 5(4), 1083-1087.
230. Stevens, M.B., et al., *Measurement techniques for the study of thin film heterogeneous water oxidation electrocatalysts*. Chem. Mater., **2016**. 29(1), 120-140.
231. Zhou, D., et al., *Layered double hydroxide-based electrocatalysts for the oxygen evolution reaction: identification and tailoring of active sites, and*

- superaerophobic nanoarray electrode assembly*. Chem. Soc. Rev., **2021**. 50(15), 8790-8817.
232. Yu, J., et al., *Preparation of two dimensional layered double hydroxide nanosheets and their applications*. Chem. Soc. Rev., **2017**. 46(19), 5950-5974.
 233. Xiao, H., H. Shin, and W.A. Goddard III, *Synergy between Fe and Ni in the optimal performance of (Ni,Fe)OOH catalysts for the oxygen evolution reaction*. Proc. Natl. Acad. Sci. U.S.A., **2018**. 115(23), 5872-5877.
 234. Louie, M.W. and A.T. Bell, *An investigation of thin-film Ni-Fe oxide catalysts for the electrochemical evolution of oxygen*. J. Am. Chem. Soc., **2013**. 135(33), 12329-12337.
 235. Ma, R. and T. Sasaki, *Nanosheets of oxides and hydroxides: ultimate 2D charge-bearing functional crystallites*. Adv. Mater., **2010**. 22(45), 5082-5104.
 236. Wang, Y., et al., *Layered double hydroxide nanosheets with multiple vacancies obtained by dry exfoliation as highly efficient oxygen evolution electrocatalysts*. Angew. Chem. Int. Ed., **2017**. 56(21), 5867-5871.
 237. Ma, R., et al., *Synthesis and exfoliation of Co²⁺-Fe³⁺ layered double hydroxides: an innovative topochemical approach*. J. Am. Chem. Soc., **2007**. 129(16), 5257-5263.
 238. Zheng, F., et al., *Sub - 2 nm ultrathin and robust 2D FeNi layered double hydroxide nanosheets packed with 1D FeNi - MOFs for enhanced oxygen evolution electrocatalysis*. Adv. Funct. Mater., **2021**. 31(43), 2103318.
 239. Diaz-Morales, O., D. Ferrus-Suspedra, and M.T.M. Koper, *The importance of nickel oxyhydroxide deprotonation on its activity towards electrochemical water oxidation*. Chem. Sci., **2016**. 7(4), 2639-2645.
 240. Zhao, G., et al., *Reduced graphene oxide modified NiFe-calcinated layered double hydroxides for enhanced photocatalytic removal of methylene blue*. Appl. Surf. Sci., **2018**. 434, 251-259.
 241. Ratcliff, E.L., et al., *Evidence for near-surface NiOOH species in solution-processed NiOx selective interlayer materials: Impact on energetics and the performance of polymer bulk heterojunction photovoltaics*. Chem. Mater., **2011**. 23(22), 4988-5000.
 242. Ali-Löytty, H., et al., *Ambient-Pressure XPS Study of a Ni-Fe Electrocatalyst for the Oxygen Evolution Reaction*. J. Phys. Chem. C, **2016**. 120(4), 2247-2253.
 243. Biesinger, M.C., et al., *Resolving surface chemical states in XPS analysis of first row transition metals, oxides and hydroxides: Cr, Mn, Fe, Co and Ni*. Appl. Surf. Sci., **2011**. 257(7), 2717-2730.
 244. Roy, C., et al., *Impact of nanoparticle size and lattice oxygen on water oxidation on NiFeO_xH_y*. Nat. Catal., **2018**. 1(11), 820-829.
 245. Yamashita, T. and P. Hayes, *Analysis of XPS spectra of Fe²⁺ and Fe³⁺ ions in oxide materials*. Appl. Surf. Sci., **2008**. 254(8), 2441-2449.
 246. Khani, H., et al., *Graphitic-shell encapsulation of metal electrocatalysts for oxygen evolution, oxygen reduction, and hydrogen evolution in alkaline solution*. Adv. Energy Mater., **2020**. 10(1), 1903215.
 247. Dong, C.Q., et al., *Eutectic-derived mesoporous Ni-Fe-O nanowire network*

- catalyzing oxygen evolution and overall water splitting. Adv. Energy Mater.*, **2018**. 8(5), 1701347.
248. Wang, H.Y., et al., *Ni³⁺-induced formation of active NiOOH on the spinel Ni-Co oxide surface for efficient oxygen evolution reaction. Adv. Energy Mater.*, **2015**. 5(10), 1500091.
249. Zhou, D., et al., *NiFe hydroxide lattice tensile strain: enhancement of adsorption of oxygenated intermediates for efficient water oxidation catalysis. Angew. Chem. Int. Ed.*, **2019**. 58(3), 736-740.
250. Heine, C., et al., *Recycling of CO₂: probing the chemical state of the Ni(111) surface during the methanation reaction with ambient-pressure X-ray photoelectron spectroscopy. J. Am. Chem. Soc.*, **2016**. 138(40), 13246-13252.
251. Okpalugo, T.I.T., et al., *High resolution XPS characterization of chemical functionalised MWCNTs and SWCNTs. Carbon*, **2005**. 43(1), 153-161.
252. Lv, H., H. Zhang, and G. Ji, *Development of novel graphene/g-C₃N₄ composite with broad-frequency and light-weight features. Part. Part. Syst. Charact.*, **2016**. 33(9), 656-663.
253. Kasten, L.S., et al., *An XPS study of cerium dopants in sol-gel coatings for aluminum 2024-T3. Surf. Coat. Technol.*, **2001**. 140(1), 11-15.
254. Trzesniewski, B.J., et al., *In situ observation of active oxygen species in Fe-containing Ni-based oxygen evolution catalysts: the effect of pH on electrochemical activity. J. Am. Chem. Soc.*, **2015**. 137(48), 15112-15121.
255. McCrory, C.C., et al., *Benchmarking hydrogen evolving reaction and oxygen evolving reaction electrocatalysts for solar water splitting devices. J. Am. Chem. Soc.*, **2015**. 137(13), 4347-4357.
256. Chakthranont, P., et al., *Effects of gold substrates on the intrinsic and extrinsic activity of high-loading nickel-based oxyhydroxide oxygen evolution catalysts. ACS Catal.*, **2017**. 7(8), 5399-5409.
257. Morales-Guio, C.G., L.A. Stern, and X. Hu, *Nanostructured hydrotreating catalysts for electrochemical hydrogen evolution. Chem. Soc. Rev.*, **2014**. 43(18), 6555-6569.
258. Voiry, D., et al., *Enhanced catalytic activity in strained chemically exfoliated WS₂ nanosheets for hydrogen evolution. Nat. Mater.*, **2013**. 12(9), 850-855.
259. Ouyang, Y.X., et al., *Activating inert basal planes of MoS₂ for hydrogen evolution reaction through the formation of different intrinsic defects. Chem. Mater.*, **2016**. 28(12), 4390-4396.
260. Cheng, C.C., et al., *Activating basal-plane catalytic activity of two-dimensional MoS₂ monolayer with remote hydrogen plasma. Nano Energy*, **2016**. 30, 846-852.
261. Ye, G., et al., *Defects engineered monolayer MoS₂ for improved hydrogen evolution reaction. Nano Lett.*, **2016**. 16(2), 1097-1103.
262. Shi, Y., et al., *Energy level engineering of MoS₂ by transition-metal doping for accelerating hydrogen evolution reaction. J. Am. Chem. Soc.*, **2017**. 139(43), 15479-15485.
263. Deng, Y.L., et al., *Operando Raman spectroscopy of amorphous molybdenum*

- sulfide (MoS_x) during the electrochemical hydrogen evolution reaction: identification of sulfur atoms as catalytically active sites for H⁺ reduction.* ACS Catal., **2016**. 6(11), 7790-7798.
264. Tran, P.D., et al., *Coordination polymer structure and revisited hydrogen evolution catalytic mechanism for amorphous molybdenum sulfide.* Nat. Mater., **2016**. 15(6), 640-646.
265. Wang, Y., et al., *Field effect modulation of heterogeneous charge transfer kinetics at back-gated two-dimensional MoS₂ electrodes.* Nano Lett., **2017**. 17(12), 7586-7592.
266. Markovic, N.M., B.N. Grgur, and P.N. Ross, *Temperature-dependent hydrogen electrochemistry on platinum low-index single-crystal surfaces in acid solutions.* J. Phys. Chem. B, **1997**. 101(27), 5405-5413.
267. Song, L., et al., *Temperature-dependent kinetics and reaction mechanism of ammonia oxidation on Pt, Ir, and PtIr alloy catalysts.* J. Electrochem. Soc., **2018**. 165(15), J3095-J3100.
268. Li, H., et al., *From bulk to monolayer MoS₂: evolution of Raman scattering.* Adv. Funct. Mater., **2012**. 22(7), 1385-1390.
269. Li, G., et al., *Activating MoS₂ for pH-universal hydrogen evolution catalysis.* J. Am. Chem. Soc., **2017**. 139(45), 16194-16200.
270. Yan, R., et al., *Thermal conductivity of monolayer molybdenum disulfide obtained from temperature-dependent Raman spectroscopy.* ACS Nano, **2014**. 8(1), 986-993.
271. Rigosi, A.F., et al., *Probing interlayer interactions in transition metal dichalcogenide heterostructures by optical spectroscopy: MoS₂/WS₂ and MoSe₂/WSe₂.* Nano Lett., **2015**. 15(8), 5033-5038.
272. Smejkal, V., et al., *Time-dependent screening explains the ultrafast excitonic signal rise in 2D semiconductors.* ACS Nano, **2021**. 15(1), 1179-1185.
273. Buscema, M., et al., *The effect of the substrate on the Raman and photoluminescence emission of single-layer MoS₂.* Nano Res., **2014**. 7(4), 561-571.
274. Ross, J.S., et al., *Electrical control of neutral and charged excitons in a monolayer semiconductor.* Nat. Commun., **2013**. 4, 1474.
275. Shi, Y., et al., *Hot electron of Au nanorods activates the electrocatalysis of hydrogen evolution on MoS₂ nanosheets.* J. Am. Chem. Soc., **2015**. 137(23), 7365-7370.
276. Zhu, J., et al., *Boundary activated hydrogen evolution reaction on monolayer MoS₂.* Nat. Commun., **2019**. 10(1), 1348.
277. He, Z.D., et al., *The pre-exponential factor in electrochemistry.* Angew. Chem. Int. Ed., **2018**. 57(27), 7948-7956.
278. Dong, G., et al., *Insight into the electrochemical activation of carbon-based cathodes for hydrogen evolution reaction.* J. Mater. Chem. A, **2015**. 3(24), 13080-13086.

Acknowledgments

I would like to thank all the people who made this dissertation possible and an unforgettable experience for me. First, I would like to extend **my sincere gratitude to Prof. Dr. Bernd Büchner for giving me an opportunity to submit and pursue my doctoral degree at TU Dresden and to Prof. Dr. Rudolf Schäfer for his support, and for their help and suggestions about my study.** In addition, I am grateful to Prof. Dr. Oliver G. Schmidt and Prof. Dr. Feng Zhu for introducing me to this institute (IFW Dresden) to carry out my Ph.D. research. I would like to further acknowledge the financial support of the China Scholarship Council (CSC) for making me live comfortably in Germany.

Special thanks to Prof. Dr. Karin Leistner in TU Chemnitz and Dr. Axel Lubk in IFW Dresden for their time in reading this dissertation draft, and for their great feedback, suggestions, and comments, which make this dissertation better.

Many thanks to Subakti Subakti, Dr. Daniel Wolf, and Dr. Axel Lub in IFW Dresden for TEM measurements. Many thanks to Marielle Deconinck and Prof. Dr. Yana Vaynzof in TU Dresden and to Dr. Steffen Oswald and Dr. Martin Hantusch in IFW Dresden for XPS measurements. Many thanks to Mrs Birgit Opitz, Dr. Ivan Kaban, and Dr. Ruben Hühne in IFW Dresden for their help of XRD measurements. Many thanks to Dr. Libo Ma and Dr. Yin Yin in IFW Dresden for their help with Raman and PL measurements. Many thanks to Dr. Stefan Baunack in IFW Dresden for his help with SEM measurements. Many thanks to Dr. Volker Neu in IFW Dresden for his help with AFM measurements. Many thanks to Dr. Mingchao Wang, Dr. Guangbo Chen, Dr. Xia Wang, and Dr. Minghao Yu in TU Dresden for the electrochemical test and FI-IR measurements. Many thanks go to Ronny Engelhard, Sandra Nestler, Jenny Herrlich, Carol Schmidt, and all the IFW cleanroom team for their technical support on photolithography, deposition techniques and invaluable tips. Great thanks to Kristina Krummer-Meier, Rita Taubert, Steffi Gerber, Julia Abram, Ines Firlle, Aline Leue, and Katrin Münster for helping with the administrative issues. Many thanks to my office

member Dr. Weijie Nie, Dr. Nand Lal Sharma, Sabour Un Sharma, and Ghata Bhayani. I also thank the colleagues in the IIN group for their kind help and fruitful discussions: Dr. Libo Ma, Dr. Yin Yin, Dr. Lixiang Liu, Tianming Li, Dr. Jin Ge, Dr. Jinhui Wang, Dr. Minshen Zhu, Hongmei Tang, Dr. Hua Zhang, Yaping Yan, Wenlan Zhang, Rachappa Ravishankar, Dr. Vineeth Kumar Bandari, Zhe Qu, Shaista Andleeb, Long Qian Xu, Subao Shi, and Yang Nan. I would like to also thank the many other members, who are always willing to provide advice on various aspects of my research.

Special thanks to my English teacher Grandpa David in Atlanta and special thanks go to Fei Li, Yi Liu, and Yang Li for their encouragement and companionship in learning, living and spiritual during these years. Special thanks to Han Liu, Marcus, Hongxiang Zhou, Dr. Xuerun Li, Shen Xing, Dr. Yaxin Zhang, Justice, Yuwen, Yaohong, Yuexi, Jou-I, I-Shan, Zhongwei, Yihan, Jinghan, etc.

Lastly, I would like to acknowledge the contribution of my parents and my older sister for their love and supports and my dearest wife, Yuru, for her love, companion, understanding, and listening over the years.

July, 2022, IFW Dresden

Jiang

Publications

- [1] **J. Qu***, F. Li, M. Wang, S. Subakti, M. Deconinck, G. Chen, Y. Li, L. Liu, X. Wang, M. Yu, D. Wolf, A. Lubk, B. Büchner, Y. Vaynzof, O. G. Schmidt, and F. Zhu, One-Pot Synthesis of Nitrate-Intercalated NiFe Layered Double Hydroxides with an 8.2 Å Interlayer Spacing, *Adv. Mater. Interfaces*, **2022**, 9, 2200973, DOI: 10.1002/admi.202200973.
- [2] **J. Qu***, Y. Li, Fei Li, T. Li, X. Wang, Y. Yin, L. Ma, O. G. Schmidt, and F. Zhu, Direct Thermal Enhancement of Hydrogen Evolution Reaction of On-Chip Monolayer MoS₂, *ACS Nano* **2022**, 16, 2, 2921-2927, DOI: 10.1021/acsnano.1c10030.
- [3] T. Li, M. Hantusch, **J. Qu**, V. K. Bandari, M. Knupfer, F. Zhu, O. G. Schmidt, *Nat. Commun.* **2022**, 13, 2875, DOI: 10.1038/s41467-022-30498-y.
- [4] F. Li, **J. Qu**, Y. Li, J. Wang, M. Zhu, L. Liu, J. Ge, S. Duan, T. Li, V. K. Bandari, M. Huang, F. Zhu, O. G. Schmidt, *Adv. Sci.* **2020**, 7, 2001561 (*Equal contribution*).
- [5] Y. Li, **J. Qu**, F. Li, Z. Qu, H. Tang, L. Liu, M. Zhu, O. G. Schmidt, *Nano Mater. Sci.* **2021**, 3, 140 (*Equal contribution*).
- [6] F. Li, Y. Li, **J. Qu**, J. Wang, V. K. Bandari, F. Zhu, O. G. Schmidt, *Nano Mater. Sci.* **2021**, 3, 154.
- [7] F. Li, J. Wang, L. Liu, **J. Qu**, Y. Li, V. K. Bandari, D. Karnaushenko, C. Becker, M. Faghih, T. Kang, S. Baunack, M. Zhu, F. Zhu, O. G. Schmidt, *Adv. Sci.* **2019**, 6, 1901051.
- [8] F. Li, M. Huang, J. H. Wang, **J. Qu**, Y. Li, L. X. Liu, V. K. Bandari, Y. Hong, B. K. Sun, M. S. Zhu, F. Zhu, Y. X. Zhang, O. G. Schmidt, *Energy Stor. Mater.* **2020**, 27, 17.
- [9] Y. R. Ge, Z. Wei, Y. S. Li, **J. Qu**, B. Y. Zu, X. C. Dou, *Sens. Actuators B Chem.* **2017**, 244, 983.
- [10] **J. Qu**, Y. Ge, B. Zu, Y. Li, X. Dou, *Small* **2016**, 12, 1369.

Curriculum Vitae

Qu, Jiang

Leibniz IFW Dresden, 01069 Dresden
j.qu@ifw-dresden.de

EDUCATION

Ph.D. in Physics 10.2019 - 01.2023 IFW Dresden	Dissertation title: Two-dimensional (2D) monolayer materials: exfoliation, characterization, and application (TU Dresden) Supervisor: Prof. Bernd Büchner
10.2016 - 09.2019	Research assistant (TU Chemnitz)
09.2013 - 06.2016	M.S. in Physics and chemistry of materials, University of the Chinese Academy of Sciences (UCAS), China.
09.2009 - 06.2013	B.S. in Inorganic non-metallic materials technology, Nanjing Tech University, China.

RESEARCH

My research interests focus on the exfoliation of 2D monolayers, including bottom-up synthesis and top-down exfoliation methods.

Currently, the 2D monolayers can be obtained effectively, such as layered double hydroxides, graphene, and transition metal dichalcogenides (TMDs, e.g. MoS_2 , WS_2 , WSe_2 , TaS_2 , etc.). The optics, spectra, and electrochemistry properties of the 2D monolayers are recorded.

Further, I am going to explore and investigate the excitons and quantum transport measurements in 2D monolayers, including, the substrate effect, heterostructure, and twisted bilayer.

SKILLS

2D monolayer device fabrication

Clean room experiences

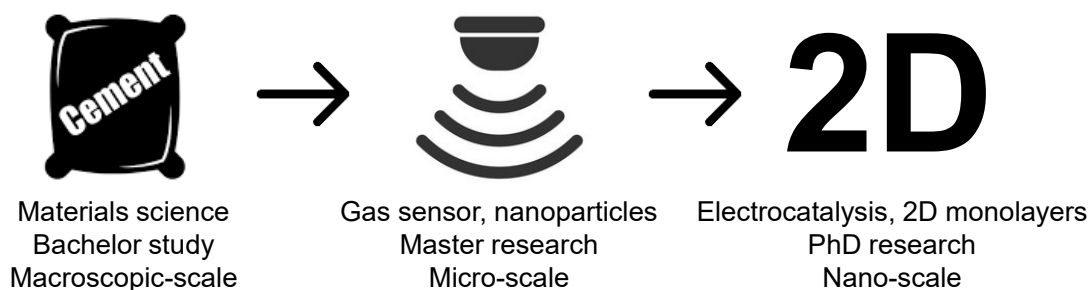
- Photolithography
- Electron beam evaporation (e-beam)
- Chemical vapor deposition (CVD)
- Atomic layer deposition (ALD)
- Reactive-ion etching (RIE)
- etc.

Characterization methods

- Atomic force microscopy (AFM)
- Raman and photoluminescence (PL)
- Scanning electron microscopy (SEM)
- X-ray diffraction (XRD)
- X-ray photoelectron spectroscopy (XPS)
- Transmission electron microscopy (TEM)
- Fourier transform infrared spectroscopy (FT-IR) ...

● Familiar with exfoliation of 2D monolayer, transfer of 2D monolayer, and device fabrication of microdevices; Measurements and analysis of 2D monolayers, such as, AFM, PL, and Raman; Application: electrochemical catalytic performance of water splitting, including, oxygen evolution reaction (OER), hydrogen evolution reaction (HER), especially, on-chip 2D monolayer devices.

RESEARCH ROUTE



PERSONAL STATEMENT

I have a good background in materials science with strong motivation to find out the novel phenomenon of 2D monolayers, including graphene, and TMDs (MoS_2 , WS_2 , MoSe_2 , WSe_2 , MoTe_2 , WTe_2 , TaS_2 , etc.).

I am focusing on the 2D monolayers, including, exfoliation of 2D monolayers, device fabrication, performance measurements, data collection, and analysis.

I have experience in preparing, submitting, revising, publishing, and reviewing manuscripts, independently.

PUBLICATIONS

- [1] J. Qu*, Y. Li, Fei Li, T. Li, X. Wang, Y. Yin, L. Ma, O. G. Schmidt, and F. Zhu, *ACS Nano* **2022**, 16, 2, 2921-2927, doi: 10.1021/acsnano.1c10030.
- [2] J. Qu*, F. Li, M. Wang, S. Subakti, M. Deconinck, G. Chen, Y. Li, L. Liu, X. Wang, M. Yu, D. Wolf, A. Lubk, B. Büchner, Y. Vaynzof, O. G. Schmidt, and F. Zhu, *Adv. Mater. Interfaces*, **2022**, doi: 10.1002/admi.202200973.
- [3] T. Li, M. Hantusch, J. Qu, V. K. Bandari, M. Knupfer, F. Zhu, O. G. Schmidt, *Nat. Commun.* **2022**, 13, 2875, doi: 10.1038/s41467-022-30498-y.
- [4] F. Li, J. Qu, Y. Li, J. Wang, M. Zhu, L. Liu, J. Ge, S. Duan, T. Li, V. K. Bandari, M. Huang, F. Zhu, O. G. Schmidt, *Adv. Sci.* **2020**, 7, 2001561 (*Equal contribution*).
- [5] Y. Li, M. Zhu, D. Karnaushenko, F. Li, J. Qu, J. Wang, P. Zhang, L. Liu, R. Ravishankar, V. Bandari, H. Tang, Z. Qu, F. Zhu, Q. Wenig, and O. Schmidt, *Nanoscale Horiz.*, **2022**, DOI: 10.1039/d2nh00472k.
- [6] Y. Li, J. Qu, F. Li, Z. Qu, H. Tang, L. Liu, M. Zhu, O. G. Schmidt, *Nano Mater. Sci.* **2021**, 3, 140 (*Equal contribution*).
- [7] F. Li, Y. Li, J. Qu, J. Wang, V. K. Bandari, F. Zhu, O. G. Schmidt, *Nano Mater. Sci.* **2021**, 3, 154.
- [8] F. Li, J. Wang, L. Liu, J. Qu, Y. Li, V. K. Bandari, D. Karnaushenko, C. Becker, M. Faghih, T. Kang, S. Baunack, M. Zhu, F. Zhu, O. G. Schmidt, *Adv. Sci.* **2019**, 6, 1901051.
- [9] F. Li, M. Huang, J. H. Wang, J. Qu, Y. Li, L. X. Liu, V. K. Bandari, Y. Hong, B. K. Sun, M. S. Zhu, F. Zhu, Y. X. Zhang, O. G. Schmidt, *Energy Stor. Mater.* **2020**, 27, 17.
- [10] J. Qu, Y. Ge, B. Zu, Y. Li, X. Dou, *Small* **2016**, 12, 1369. (Gas sensor)

Qu, Jiang (屈江) - Google Scholar

Selbständigkeitserklärung

Hiermit versichere ich, dass ich die vorliegende Arbeit ohne unzulässige Hilfe Dritter und ohne Benutzung anderer als der angegebenen Hilfsmittel angefertigt habe; die aus fremden Quellen direkt oder indirekt übernommenen Gedanken sind als solche kenntlich gemacht.

Weitere Personen waren an der Abfassung der vorliegenden Arbeit nicht beteiligt. Die Hilfe eines Promotionsberaters habe ich nicht in Anspruch genommen. Weitere Personen haben von mir keine geldwerten Leistungen für Arbeiten erhalten, die im Zusammenhang mit dem Inhalt der vorgelegten Dissertation stehen. Diese Dissertation wurde durchgeführt am Leibniz-Institut für Festkörper- und Werkstoffforschung Dresden (IFW Dresden).

Die Arbeit wurde bisher weder im Inland noch im Ausland in gleicher oder ähnlicher Form einer anderen Prüfungsbehörde vorgelegt.

.....

Ort, Datum

.....

Unterschrift
